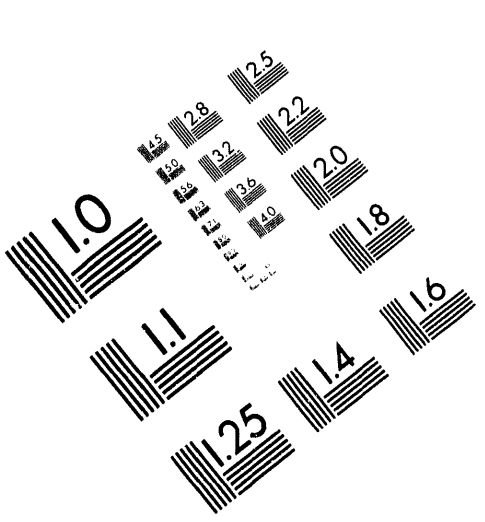

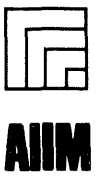

Association for Information and Image Management
1100 Wayne Avenue, Suite 1100
Silver Spring, Maryland 20910
301/587-8202

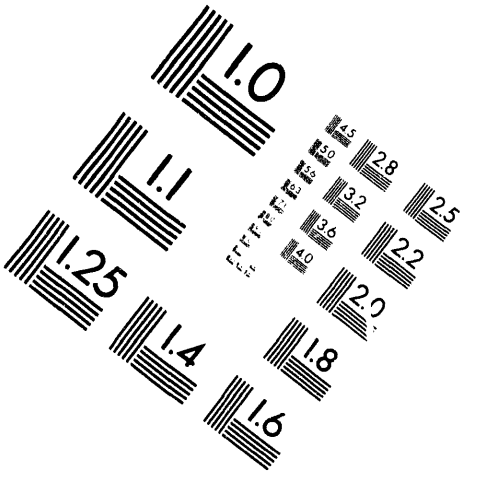

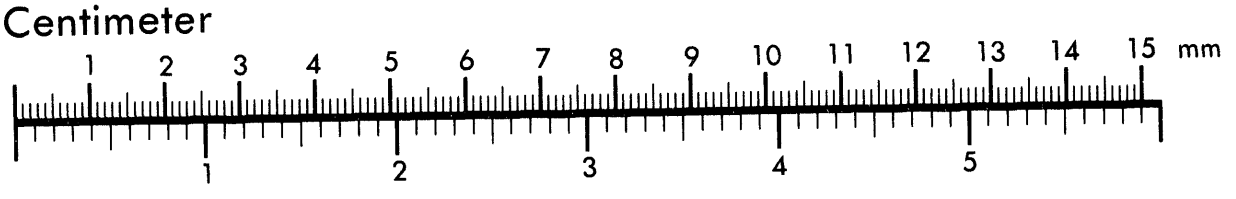

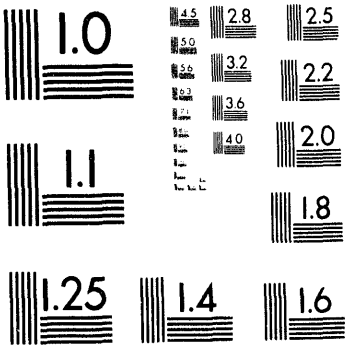

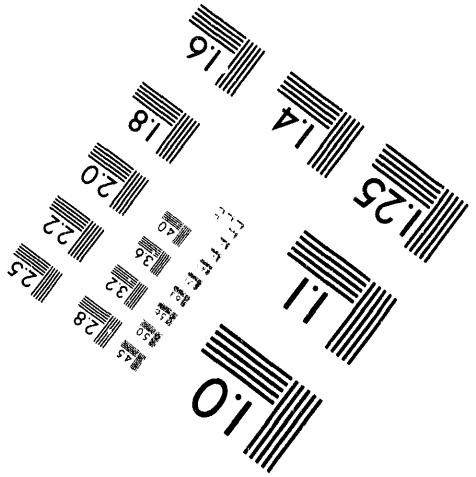

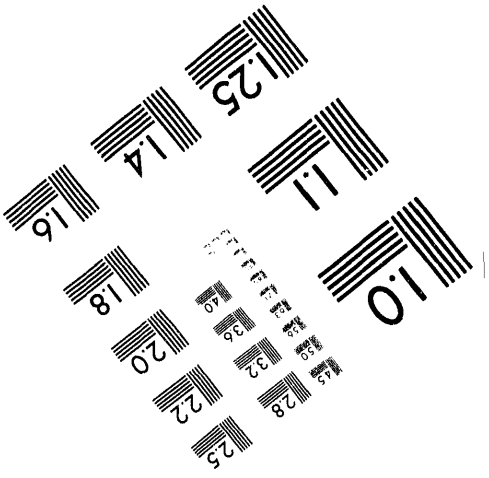

1 of 2

LBL-34376
UC-000

Linear Adaptive Noise-reduction Filters for Tomographic Imaging: Optimizing for Minimum Mean Square Error

Winston Y. Sun
Ph.D. Thesis

Department of Electrical Engineering and Computer Sciences
University of California

and

Life Sciences Division
Lawrence Berkeley Laboratory
University of California
Berkeley, California 94720

April 1993

This work was supported by the National Institutes of Health under Grant HL 07367, through the U.S. Department of Energy under Contract No. DE-AC03-76SF00098.

Abstract

Linear Adaptive Noise-reduction Filters for Tomographic Image Reconstruction:
Optimizing for Minimum Mean-square Error

by

Winston Y. Sun

Doctor of Philosophy

University of California at Berkeley

Professor Thomas F. Budinger, Chair

This thesis solves the problem of finding the optimal linear noise-reduction filter for linear tomographic image reconstruction. The optimization is data dependent and results in minimizing the mean-square error of the reconstructed image. The error is defined as the difference between the result and the best possible reconstruction. Applications for the optimal filter include reconstructions of positron emission tomographic (PET), X-ray computed tomographic, single-photon emission tomographic, and nuclear magnetic resonance imaging. Using high resolution PET as an example, the optimal filter is derived and presented for the convolution backprojection, Moore-Penrose pseudoinverse, and the natural-pixel basis set reconstruction methods. Simulations and experimental results are presented for the convolution backprojection method.

Linear filters which optimize for minimum mean-square error (mmse) are called Wiener filters; such filters require the knowledge of the signal and noise statistics. Unfortunately, the noise and signal statistics are unknown other than the well-accepted model that the PET-detected events follow Poisson statistics. This work investigates a novel technique of spectral estimation using the concept of reprojection (measuring the projections of a reconstructed image). The technique is adaptive wherein the filter shape changes to accommodate for the number of detected events and the shape projection of the object. Simulations show that the technique results in good agreement between the theoretical values and the experimental results.

The characteristic noise power of a reconstructed image for a particular tomograph geometry is found by averaging the power spectral density (PSD) of 500 white-noise reprojections. White-noise reprojections are obtained by projecting reconstructions (using only a ramp filter) of white-noise projections. Estimating the noise power in a particular projection of a specific data set is accomplished by normalizing the noise PSD characterization to the total power of the reprojected data set in the high-frequency band where noise dominates over the signal. Normalization is done by a single parameter scale factor to achieve a least-squares fit over the upper m frequency indices. The PSD of the signal is therefore the remainder after subtracting the normalized noise power from the total PSD. Robustness of the estimation technique was measured in terms of sensitivity to the number (m) of frequency indices used to normalize the noise power characteristics. Simulations using a complex-brain phantom show that varying m over the highest 25% of the frequency band results in less than 0.1% change (relative to the local mean) in the standard deviations of selected uniform regions.

A set of simulations comparing the results of the conventional Butterworth (BW) noise-reduction filter and the Wiener filter are presented. The standard deviations for selected regions of uniform activity were measured for simple geometric phantoms (uniform disk, uniform rectangle and ring with two rectangles) for varying number of detected events. Both the BW-filtered and the Wiener-filtered results show that a ten-fold increase in the number of counts from 2×10^5 to 2×10^6 reduces the standard deviation by a factor of 2.50 or more. The simulations show that the adaptive Wiener filter outperforms the BW filter for non-isotropic phantoms where the spectral content of the phantom varies from angle to angle.

A new approach to measure reconstructed-image quality was derived to compare the Wiener filter method to other algorithms. Despite the fact that the standard deviations for the Wiener-filtered reconstructions are generally smaller than BW-filtered counterpart, the improvement is only minor. However, the visual quality of the Wiener-filtered images have distinct characteristics and markedly different appearances compared to the BW-filtered results — the BW-filtered images are characterized by coarse 2-D textural noise whereas the Wiener-filtered images are characterized

by a much finer textural noise. Since the rms error is not the optimal metric to measure image quality, a new method of quantifying image quality was developed in this thesis. By segmenting the pixels in a region of known uniform activity into 5 gray-scale levels representing the degree of fluctuations of each pixel from the region mean, a spatial distribution of the variation from the local mean can be represented. The 5 levels of binning were categorized by pixel values that are within ± 12.5% of the local mean, pixel values that are between ± 12.5% and ± 25%, between ± 25% and ± 50%, between ± 50% and ± 75%, and values that exceed ±75% of the local mean. Image quality can be quantified by measuring the number of pixels that fall within a threshold window. Simulations show that the Wiener-filtered reconstructions contain more than twice as many pixels within the ±50% threshold window than the BW-filtered reconstructions.

The results of the Wiener-filtered reconstruction of an experimental data set collected from the Donner 600-crystal high-resolution tomograph are compared to the BW-filtered reconstructions. As in the simulations, the visual appearance of the noise in the BW-filtered images is characterized by coarse textures with oscillating gray-scale values whereas the Wiener-filtered images have much a finer texture with a more uniform gray-scale-valued background.

Reconstruction results for a complex-brain phantom are compared for the BW-filtered, Wiener-filtered reconstructions and for the reconstructions using the maximum likelihood estimation (MLE) method. Comparisons of the ROI statistics show that the Wiener-filtered image have lower standard deviations in a uniform region as compared to both the BW-filtered and the MLE reconstructions.

Prof. T. F. Budinger, Chair

Acknowledgments

My sincerest thanks and gratitude goes to Professor Thomas Budinger and to Professor Stephen Derenzo for their guidance and advice, and for giving me the opportunity to work at the Center for Functional Imaging. I wish to also thank Dr. Ron Huesman and Dr. S.T.S. Wong for many helpful discussions and tutorials during my stay at the Functional Imaging lab. I wish to thank Dr. Jorge Llacer who contributed greatly to my knowledge of non-linear reconstruction methods and for allowing me to use some of his software to compare results of the MLE methods to that of the work presented in this thesis. I am indebted to all the fellow graduate students whom I've worked with during my stay at Berkeley in particular my officemates Blaise Frederick, Josh Lack, Paul Hughett, and especially Dr. John Keltner for his support both in and out of the research environment.

As I reflect on my student life, I have to offer my gratitude to my friends who *all* contributed in helping me finally reach my goal. Life just wouldn't have been the same without 'em. A special thanks goes to Dr. Gino Addiego for all the madness that kept me sane; Kelvin Okimoto and Frank Viana for the "surfari's"; Anantha Chandrakasan for all those "ten's"; Frank Dunlap, Steve Hrinya, and Bill McFarland for the Thursday nite BBQ's, "skate @ 8's", etc...; 'Three Molakas' for the gyros, "cling peaches" and the "bullets"; Glenn Tso for helping me "dodge all the bullets"; Mark Loewenstein for the Saturday lunches; and to all my other pals whom I haven't mentioned for their friendship.

I am also indebted to my family who gave me support and encouragement. To my siblings Vivienne, Barbara, Mamie, Wesley, and Diana for their endless support, I offer you all my warmest thanks. To the late Eloise Sterling Hirt who gave me inspiration and strength, I reserve a place in my heart for you. Finally, I offer my deepest thanks to my parents Stanley and Grace Sun for all their love, patience and encouragement.

This work was supported by the U.S. Department of Energy under Contract No. DE-AC03-76SF00098 and by the National Institute of Health under Grant HL-07367.

Contents

GLOSSARY

1-D one dimensional

2-D two dimensional

BW Butterworth

CBP Convolution Backprojection (aka filtered backprojection)

LLSE Linear Least-Square Estimate

LSI Linear Shift Invariant

MLE Maximum Likelihood Estimation

mmse minimum mean-square error

mse mean-square error

M-P Moore-Penrose (pseudoinverse)

MTF Modulation Transfer Function (point spread function)

NR Noise Reduction

PET Positron Emission Tomography

PSD Power Spectral Density

ROI Region of Interest

RSR Ring Surrounding (2) Rectangles (phantom)

SNR Signal to Noise Ratio

SVD Singular Value Decomposition

UCD Uniform Circular Disk (phantom)

URP Uniform Rectangular Phantom

Chapter 1

Introduction

1.1 Statement of thesis

This thesis investigates the techniques of solving for optimal linear filters which results in the minimum mean-square error (mmse). As will be shown, a prerequisite for the solution to these optimal filters is some *a priori* knowledge of the signal and noise characteristics. One of the main difficulties is to obtain estimates for these unknown parameters. The main focus of this work is to develop a new technique to estimate the noise and signal statistics given only one low-count measurement.

The problem of linear tomographic reconstruction has been investigated by many authors. Baker [1], Ramachandra [2], Marr [3], Buonocore [4], etc... have all solved the inverse problem. The problem remains that for high resolution positron emission tomograph (PET) data, the signal-to-noise ratio (SNR) is limited and a noise-reduction filter is necessary to reconstruct images of "good" quality. The "goodness" of an image can be defined many ways. For instance, one of the benefits of filtering out the noise is that the SNR will be improved and hence the visual fidelity of the reconstructed image enhanced. However, the visual fidelity criterion is not a well defined mathematical cost function and for quantitative studies an objective metric is necessary. Thus, the mean-square error will be considered as a metric to measure the "goodness" of an image.

Incorporating known priors such as the modulation transfer function (MTF) of the tomograph, reconstruction method, and statistical behavior of the noise this work develops a method of estimating the noise and signal power spectra to be used in Wiener filters which can then be used to achieve mmse estimate of the original object. Finally, as a practical clinical tool the implementation of the algorithm must be made such that fast reconstruction times are possible. Applications of the optimal filtering can then be used in other medical imaging modalities such as fast X-ray computed tomography (X-ray CT) and single photon emission computed tomography (SPECT) as well as PET.

1.2 Motivation and background

The goal of this work is to reconstruct images without time-consuming iterations for the data acquired by the Donner 600-crystal high-resolution tomograph. Currently, the standard method of image reconstruction involves manually iterating and selecting the cut-off frequency and filter order of the Butterworth (BW) low-pass filter as depicted in figure 1.1. Several reconstructions using different BW filters are done and the "best" image is selected for clinical use. One clinical application for the

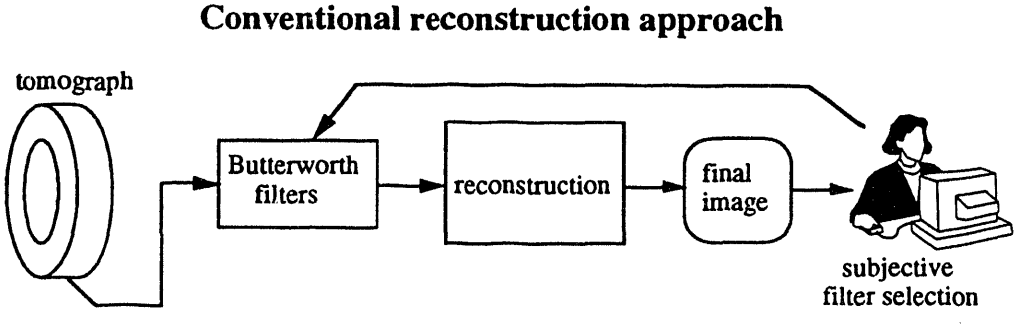

Figure 1.1: Block diagram illustrating the conventional reconstruction using the Butterworth filter requiring manual iteration and subjective filter selection.

tomographic reconstruction tools is for use with fast X-ray CT's. Traumatic head

injuries must be quickly diagnosed using the X-ray CT scanners and reconstruction times in ten seconds per slice is necessary. With current computing technologies the only method of reconstruction capable of attaining these speeds is with the convolution backprojection (CBP) method (also referred to as filtered backprojection). By developing an algorithm that automatically generates the ideal noise-reduction filter based on the data collected, the manual iteration and selection process can be eliminated and an optimized reconstruction can be achieved as a pictured in figure 1.2.

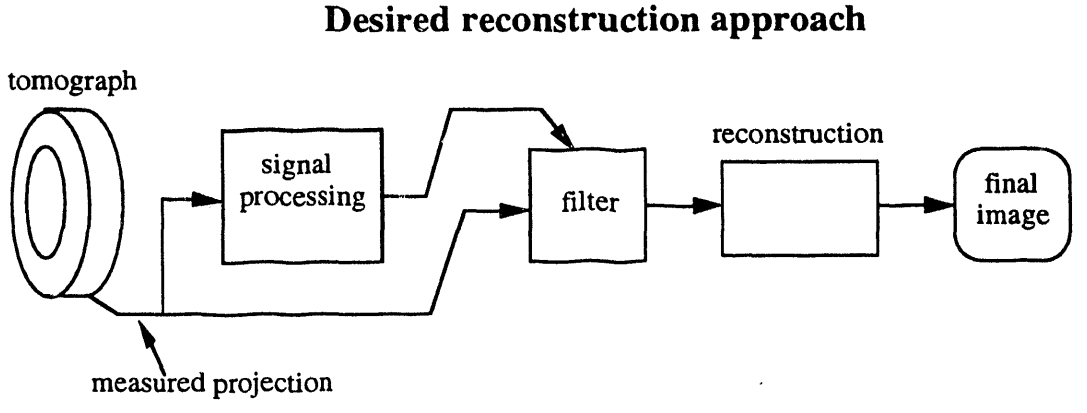

Figure 1.2: Block diagram illustrating the desired approach of reconstruction where the data is processed and analyzed to determine automatically the optimal noise reduction filter.

Parallel projections form what are known as the Radon transform [5] of an image. A perfect reconstruction of the original image is possible by inverting this operation using the inverse Radon transform (for a square integralable $b(x,y)$). However, a true Radon transform requires measurements in infinitesimal increments in both angle and projection bins as indicated by integrals in the Radon and its inverse transform equations 1.1 and 1.2 below: ($\mathcal{P}$ denotes the projection or the Radon transform, $\mathcal{B}$ denotes the backprojection operation, and $\mathcal{R}$ denotes the linear shift-invariant ramp filtering operation where the ramp filter in the frequency domain is merely: $R(f) = |f|$ for $f : -\infty < f < \infty$).

$$p(s,\theta) \equiv \mathcal{P}b = \int_{-\infty}^{\infty}\int_{-\infty}^{\infty} b(x,y)\delta(x\cos\theta + y\sin\theta - s)dxdy, \qquad (1.1)$$

$$\text{with } -\infty < s < \infty;\ 0 \leq \theta < \pi$$

and for the inverse,

$$b(x,y) \equiv \mathcal{BR}p = \int_0^{\pi} \int_{-\infty}^{\infty} |\xi| P(\zeta,\theta) \exp[j2\pi\xi(x\cos\theta + y\sin\theta)] d\xi d\theta \tag{1.2}$$

where $P(\xi,\theta)$ is the 1-D Fourier transform of $p(s,\theta)$ in the s (the radial coordinate) direction and ξ is the Fourier component of s. Note that the inner integral in the inverse Radon transform is merely the 1-D inverse Fourier transform of $|\xi|P(\xi,\theta)$ which is just $p(s,\theta)\otimes$ (ramp-filter kernel), where $\otimes$ denotes the convolution operator. In practical PET, parallel projection measurements can only be made in finite number of angles and bins. Hence, the common method of reconstructing PET images uses the approximation to the inverse Radon transform [2] [6] [7] [8] [9] which can be written in an equation as follows:

$$b(x,y) \approx \Delta \sum_{n=0}^{\Theta-1} \sum_{k=0}^{K-1} p(k,\hat{\theta}) r(\hat{s}-k) \tag{1.3}$$

where

$$\hat{s} = x\cos(n\Delta) + y\sin(n\Delta) \tag{1.4}$$

and

$$\hat{\theta} = n\Delta. \tag{1.5}$$

Again, the second summation is a discrete circular convolution and $r(s)$ is the 1-D inverse discrete Fourier transform of a truncated ramp function, i.e.

$$R(f) = \mathcal{F}_{2f_o}\{r(s)\} = |f| \tag{1.6}$$

$$\text{for } f\text{: - } f_o < f \leq f_o$$

where f_o is the Nyquist rate, $\mathcal{F}_{2f_o}$ is the discrete $2f_o$-point 1-D Fourier transform operator and f is the frequency index. Another alternative to $R(f)$, when using the discrete approximation to the inverse Radon transform, is:

$$R(f) = \mathcal{F}_{2f_o}\{\mathcal{F}_{4f_o}^{-1}\{|f|\}\} \tag{1.7}$$

$$\text{for } f : -2f_o < f \leq 2f_o$$

where the $\mathcal{F}_{4f_o}$ indicates a discrete $4f_o$-point Fourier transform. The discrete Fourier transforms are implemented using the fast Fourier transform (FFT) algorithm. The above $R(f)$ aliases less in the spatial domain than the first approximation to the ramp filter as more frequency indices are used to approximate the ramp kernel.

This method of reconstruction does an outstanding job of reconstructing the original image in the absence of noise as the original uniform circular disk versus reconstructed image is shown below in figures 1.3 and 1.4. However, practical tomo-

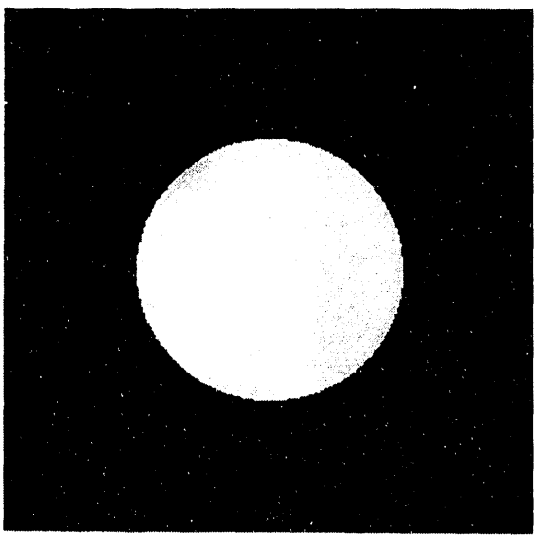

Figure 1.3: The original uniform circular disk phantom

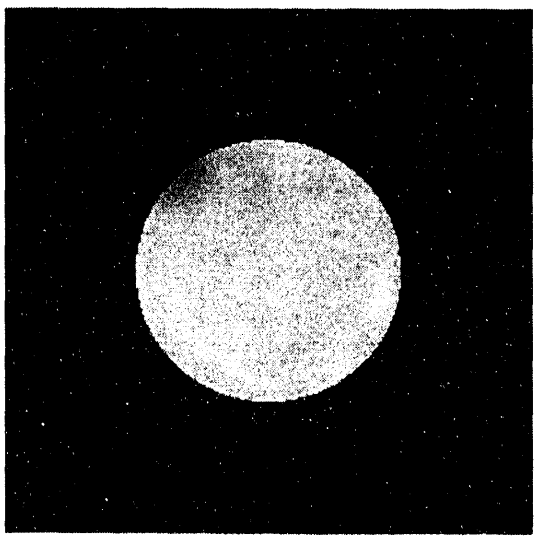

Figure 1.4: The reconstructed image in absence of noise

graph measurements include noise as well as the true signal (the projections). Figure 1.5 shows what the same reconstruction looks like when simulated noise is added to the projection data before reconstruction. The simulated noisy projection data is a realization of a Poisson process such that the noisy projection, $p'(s,\theta)$, is generated by the following:

$$p'(s,\theta) = Poisson(\lambda = p(s,\theta)) \tag{1.8}$$

where $p(s,\theta)$ is the ideal analytic projection.

Previous attempts at noise-reduction filtering techniques have been based primarily on heuristics including non-adaptive filters such as the Hanning, Hamming, Shep-Logan low-pass filters [7] [2] [10]. Adaptive filters based on heuristics include

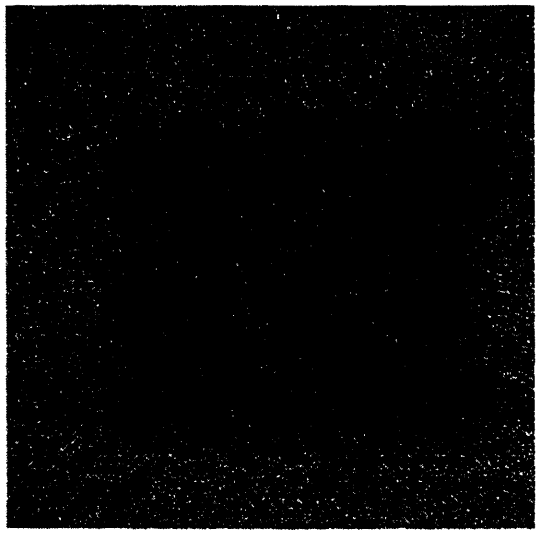

Figure 1.5: Reconstruction for a 500,000 event simulation without using any NR filters.

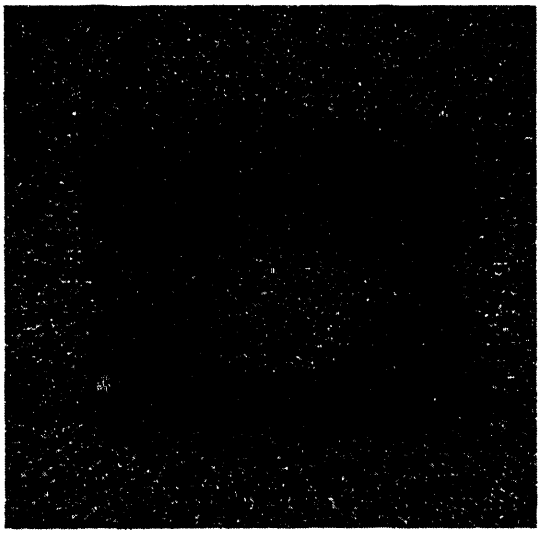

Figure 1.6: Reconstruction of the same data set using a Butterworth NR filter.

the Butterworth [11] [10] and Metz filters [12]. The Butterworth (BW) filters are perhaps the most universally used noise-reduction filters because of their flexibility. By manually iterating the parameters of cut-off frequency and filter order, a clinician is able to attain a reconstructed image with good visual fidelity or appearance. Figure 1.6 illustrates one possible BW-filtered reconstruction of the same uniform circular disk phantom. The drawback to this technique is that bias is introduced by each clinician or viewer who picks his/her own BW parameters. Thus, a goal of this work is to develop a method to filter the projections in an objective way.

Adaptive Wiener filters which minimize mean-square error have been suggested in various forms by Tsui [13] and Shim - Cho [14]. Tsui's filter is to be used in conjunction with the conventional CBP reconstruction whereas Shim-Cho's filter is based on the pseudoinverse (of the projection formation matrix) reconstruction. In either case, prior knowledge of the noise and signal statistics (power spectra, auto-correlation matrix) is required. This thesis further develops the concepts of Wiener filtering developed by Tsui and improves upon the method of estimating the noise and the signal power for measurements with poor SNR's.

Other reconstruction methods for PET have been developed in recent years which are based on Bayesian methods (MAP) [7] [15] [16] and the maximum likeli-

hood estimation (MLE) method [17] [18] [19] [20]. The MAP method results in the identical solution as that of the mmse filtering method for noise which have zero mean [7]. Again, as in the case of the mmse solution, prior knowledge of the noise and signal statistics is necessary to use the MAP approach. The MLE uses the expectation-maximization (EM) algorithm which is an iterative approach to solve a log-likelihood equation for a Poisson process for which there is no closed-form solution [21]. This method makes efficient use of the data as it utilizes the Poisson statistics without having to model it as an additive Gaussian. There are, however, some drawbacks to the MLE method. Computationally, the iterative EM algorithm takes an order of magnitude (or more) more time to reach to a convergent solution. Furthermore, the solution that the MLE method converges to is typically characterized by large oscillations in the pixel values within a region of constant value. In order to correct for these large oscillations various "stopping" rules and heuristic low-pass filtering is applied to achieve smoother and visually appealing images [20] [22] [23]. However, these "stopping" rules and heuristic low-pass filters add bias to the solution.

A more complete summary of tomographic reconstruction algorithms are given by Rangayyan [24].

Chapter 2

Theoretical Considerations

Mathematical model of the data acquisition as well as the data itself is the topic of discussion in the first section of this chapter. Methods of reconstruction as well as the reconstruction optimization are considered. Using an additive independent noise model for the measured data, three methods of image reconstruction are presented as well as the optimizing reconstruction filter to be used with each method.

2.1 Data Acquisition

The ideal data acquisition process can be mathematically modeled by the vector-matrix equation 2.1 below

$$\underline{p} = \mathbf{F}\underline{b}. \tag{2.1}$$

In this equation, $\underline{p}$ is the measured projection vector, $\underline{b}$ is the vectorized object, and $\mathbf{F}$ is the measurement matrix (or the projection formation matrix). For the case of an ideal Radon transform, the vectors would be infinite dimensional and $\mathbf{F}$ would be the continuous space projection formation operator. However, in order to simplify calculations, the object b is modeled as a gridded or pixelized 2-dimensional object with uniform density in each pixel [25] [26] [27]. This pixelization is illustrated in figure 2.1 below.

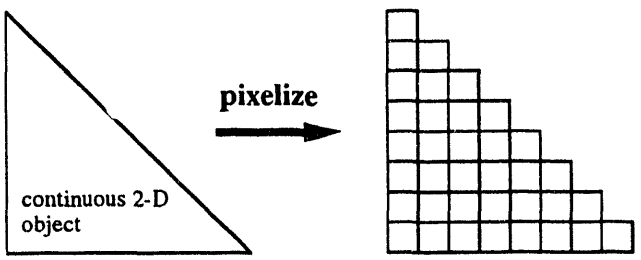

Figure 2.1: Example of how a continuous 2-D object is modeled as a collection of uniform pixels.

A simple example of a 4×4 pixelized object below (figure 2.2) illustrates the physical interpretation of equation 2.1. In this example, two projection angles orthogonal

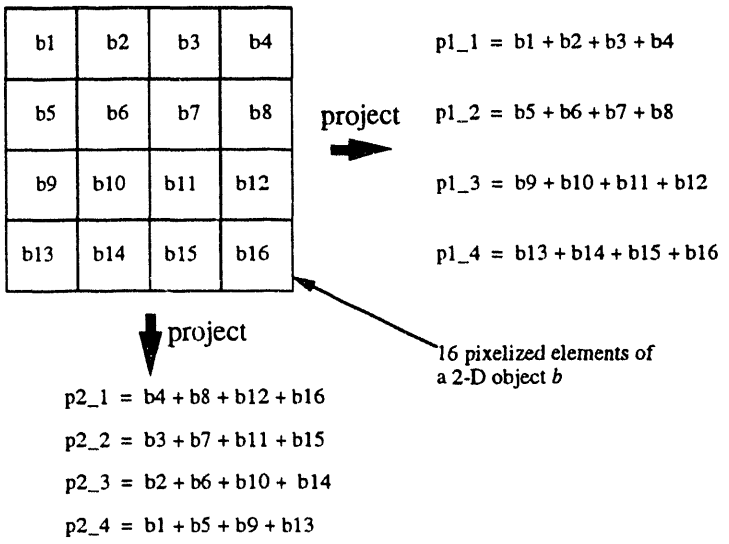

Figure 2.2: Example of a square object gridded into 16 uniform pixels and its projections in two angles. Pn-m is the m-th projection bin in the n-th projection angle.

to one another measures four bins in each angle. The 2-D object, b is vectorized as a column-ordered vector as shown below:

$$\underline{b} = [\ b_1\ b_2\ b_3\ b_4\ b_5\ b_6\ b_7\ b_8\ b_9\ b_{10}\ b_{11}\ b_{12}\ b_{13}\ b_{14}\ b_{15}\ b_{16}\ ]^T$$

The $\mathbf{F}$ matrix is the measurement matrix that transforms the object vector $\underline{b}$ and the results in the projection vector $\underline{p}$. The $\mathbf{F}$ matrix is determined by the geometry

of the tomograph and how measurements are physically made. Horizontal projection through the upper fourth of $\underline{b}$ in the above image results in a projection p_{1-1} (1st projection angle - 1st bin) = $b_1 + b_2 + b_3 + b_4$; Thus, the first row of $\mathbf{F}$ is [1 1 1 1 0 0 0 0 0 0 0 0 0 0 0 0]. The other 7 row entries can be similarly determined by inspection of the equation below.

$$\underline{p} = \begin{bmatrix} \underline{p}_1^T & \underline{p}_2^T \end{bmatrix}^T$$

$$= \begin{bmatrix} p_{1-1} & p_{1-2} & p_{1-3} & p_{1-4} & p_{2-1} & p_{2-2} & p_{2-3} & p_{2-4} \end{bmatrix}^T$$

$$= \begin{bmatrix} b_1 + b_2 + b_3 + b_4 \\ b_5 + b_6 + b_7 + b_8 \\ b_9 + b_{10} + b_{11} + b_{12} \\ b_{13} + b_{14} + b_{15} + b_{16} \\ b_4 + b_8 + b_{12} + b_{16} \\ b_3 + b_7 + b_{11} + b_{15} \\ b_2 + b_6 + b_{10} + b_{14} \\ b_1 + b_5 + b_9 + b_{13} \end{bmatrix}$$

$$\underline{p} = \mathbf{F} \begin{bmatrix} b_1 & b_2 & b_3 & b_4 & b_5 & b_6 & b_7 & b_8 & b_9 & b_{10} & b_{11} & b_{12} & b_{13} & b_{14} & b_{15} & b_{16} \end{bmatrix}^T$$

In PET, the ideal projection formation equation must be interpreted in a statistical manner because the physics of the measurement process do not correspond to analytical projection measurements. The measurement process for PET proceeds as follows. A metabolically active tracer labeled with a positron-emitting radionuclide is injected into a patient where after a short time, accumulation (of the radionuclide) in that part of the anatomy for which the tracer molecule has an affinity occurs. When the radioactive nuclei decay they emit positrons which immediately annihilate with nearby electrons to produce a pair of 511-keV photons traveling in opposite directions. When the photon pairs are detected simultaneously, an annihilation event somewhere along the line connecting the two detectors is assumed to have occurred. After detecting 500,000+ events (for the Donner 600-crystal tomograph measuring a

brain) a reconstruction can be made. Each labeled tracer molecule is a positron emitter which undergoes a radioactive decay and like all other radioactive decay processes it is modeled as a Poisson process. Since each tracer molecule decays independently from others, emissions can be modeled as independent Poisson processes. The tomograph measurement is simply the collective sum of all detected emissions so that each projection bin can be modeled as the superposition of independent Poissons. The statistical interpretation of the measurements becomes

$$E\underline{p} = \mathbf{F}\underline{b} \tag{2.2}$$

where the E is the expectation operator. Or, the expected value of the measurements is equal to the value of the analytic projections. Since the data is Poisson, the variance of the data is equal to the expected value.

For a random variable, x, having Poisson statistics a Gaussian substitute described by equations 2.3 and 2.4 [28] [29]:

$$x \sim Poisson(\lambda = Ex) \tag{2.3}$$

$$x' = x'' + N(\mu = 0, \sigma = \sqrt{Ex}) \tag{2.4}$$

where $x'' = Ex$ and $N(\mu, \sigma)$ is a Gaussian with mean $= \mu$ and standard deviation $= \sigma$ models the first and second order statistics of a Poisson process. As can be seen from equation 2.4, the new random variable x' has the same expected value and variance as x. If a measured signal has stationary Poisson statistics, there are advantages of modeling that signal using the Gaussian model where the signal component can be thought of as Ex and the noise being $N(0, \sqrt{Ex})$. Modeling the projections as Poisson, the noise is no longer purely additive [30] and linear methods of solving for a mmse-producing filters are not possible.

2.2 Linear Reconstruction

The reconstruction of tomographic images is that of an inverse problem. That is, all linear methods are based on inverting the data acquisition process. Whether it involves finding the exact inverse, approximating the inverse or finding the Moore-Penrose pseudoinverse the basis of reconstruction is solving for $\underline{b}$ in the equation

$$\underline{p} = \mathbf{F}\underline{b}.$$

In the case of PET, the $\mathbf{F}$ matrix is the projection formation operator as described in an earlier example shown in figure 2.2. The $\mathbf{F}$ matrix is a function of the tomograph geometry including the number of sampling angles and number the detectors (or bins). The 8×16 $\mathbf{F}$ matrix below, corresponding to the projection formation matrix for the sampling geometry shown in figure 2.2

$$\mathbf{F} = \begin{bmatrix} 1 & 1 & 1 & 1 & 0 & 0 & 0 & 0 & 0 & 0 & 0 & 0 & 0 & 0 & 0 & 0 \\ 0 & 0 & 0 & 0 & 1 & 1 & 1 & 1 & 0 & 0 & 0 & 0 & 0 & 0 & 0 & 0 \\ 0 & 0 & 0 & 0 & 0 & 0 & 0 & 0 & 1 & 1 & 1 & 1 & 0 & 0 & 0 & 0 \\ 0 & 0 & 0 & 0 & 0 & 0 & 0 & 0 & 0 & 0 & 0 & 0 & 1 & 1 & 1 & 1 \\ 0 & 0 & 0 & 1 & 0 & 0 & 0 & 1 & 0 & 0 & 0 & 1 & 0 & 0 & 0 & 1 \\ 0 & 0 & 1 & 0 & 0 & 0 & 1 & 0 & 0 & 0 & 1 & 0 & 0 & 0 & 1 & 0 \\ 0 & 1 & 0 & 0 & 0 & 1 & 0 & 0 & 0 & 1 & 0 & 0 & 0 & 1 & 0 & 0 \\ 1 & 0 & 0 & 0 & 1 & 0 & 0 & 0 & 1 & 0 & 0 & 0 & 1 & 0 & 0 & 0 \end{bmatrix}$$

is not full rank as you can add the first four rows and subtract the fifth, sixth, and seventh row to yield the eighth row. In general the size of the $\mathbf{F}$ matrix is ΘK x dim($\underline{b}$), where Θ is the number of projection angles, K is the number of bins in each angle, and dim(·) is the dimension of the argument. Another example shown below in figure 2.3 uses geometries more convenient for typical tomographs. Here, the tomograph samples at four evenly space angles with two projection bins in each angle. For this case, $\mathbf{F}$ is described by a 8×8 matrix as shown below. The object $\underline{b}$ is dissected into eight equal parts and the first projection bin in the first angle, $p1_1$,

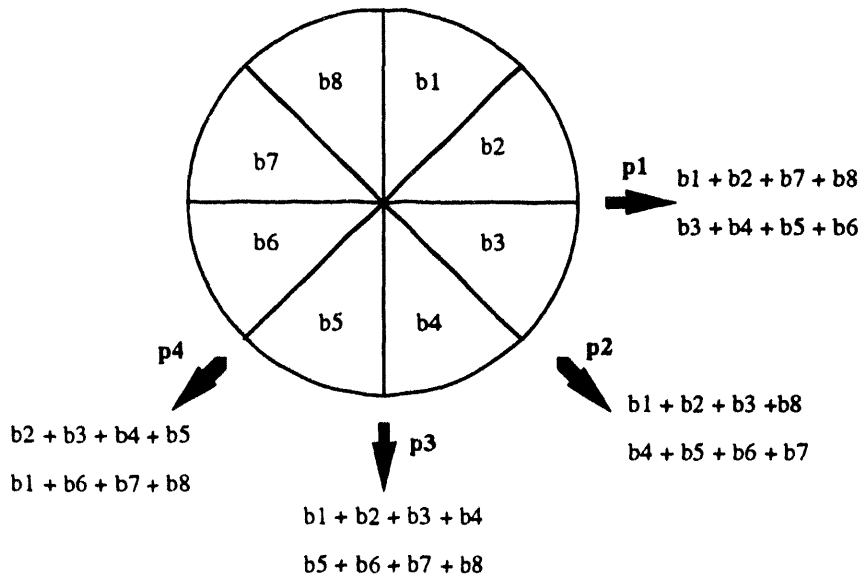

Figure 2.3: Example of a circular object gridded into 8 pixels and its projections at 4 equally spaced angles.

is simply the sum of the upper 4 pie pieces which is just $b_1 + b_2 + b_7 + b_8$. Thus, the first row of $\mathbf{F}$ is

$$\mathbf{F}_{1,n} = [1\ 1\ 0\ 0\ 0\ 0\ 1\ 1].$$

The rest of the F matrix can be filled in by looking at the projection bin values and determining the correct linear combinations of b_i's. The resulting $\mathbf{F}$ matrix is as follows:

$$\mathbf{F} = \begin{bmatrix} 1 & 1 & 0 & 0 & 0 & 0 & 1 & 1 \\ 0 & 0 & 1 & 1 & 1 & 1 & 0 & 0 \\ 1 & 1 & 1 & 0 & 0 & 0 & 0 & 1 \\ 0 & 0 & 0 & 1 & 1 & 1 & 1 & 0 \\ 1 & 1 & 1 & 1 & 0 & 0 & 0 & 0 \\ 0 & 0 & 0 & 0 & 1 & 1 & 1 & 1 \\ 0 & 1 & 1 & 1 & 1 & 0 & 0 & 0 \\ 1 & 0 & 0 & 0 & 0 & 1 & 1 & 1 \end{bmatrix}.$$

Again, this 8×8 matrix is not full rank as the linear combination of the first 7 rows yield the eighth. For any projection formation matrix, $\mathbf{F}$, the rank of $\mathbf{F}$ can be shown

to be Θ (K - 1) + 1 [1] [31] and thus always singular. This means that the equation is ill-posed and there is no unique solution when solving for $\underline{b}$.

There are, however, ways to over come the singularity problem. The conventional filtered backprojection is based on the approximation to the Radon/inverse Radon transforms. As stated in the previous chapter, for the case where projections measurements are made in infinitesimal increments both in angle and bin width perfect inversion/reconstruction (for a projection of the original square integralable function, $b(x,y)$) is possible as shown below:

$$b(x,y) = \int_0^{\pi} \int_{-\infty}^{\infty} |\xi| P(\xi,\theta) \exp[j2\pi\xi(x\cos\theta + y\sin\theta)] d\xi d\theta$$

By replacing the integral sign with a summation sign on the inverse Radon equation and replacing the ramp filter with a truncated ramp filter an approximation of inverse radon transform is made and is the basis for the conventional filtered backprojection reconstruction.

$$\underline{b} = \sum_{\theta=0}^{\Theta-1} \sum_{k=0}^{K-1} p(k,\theta) r(n-k)$$

It is noteworthy to investigate the relationship between the projection operation and the backprojection operation. Let u and v be real Hilbert spaces where u is the range space and v is the domain space of the Radon transform, $\mathcal{R}$. Namely,

$$b(x,y) \in v \text{ and } p(s,\theta) \in u.$$

Starting from the projection equation (Radon transform) below,

$$p(s,\theta) \equiv \mathcal{R}b = \int_{-\infty}^{\infty} \int_{-\infty}^{\infty} b(x,y)\delta(x\cos\theta + y\sin\theta - s) dx dy,$$

then with $\langle \cdot, \cdot \rangle$ denoting the inner product,

$$\langle \mathcal{P}b, p \rangle_v = \int_{-\infty}^{\infty} ds \int_0^{\pi} d\theta [\int_{-\infty}^{\infty} \int_{-\infty}^{\infty} b(x,y)\delta(x\cos\theta + y\sin\theta - s) dx dy] \qquad (2.5)$$

$$= \int_0^{\pi} d\theta \int_{-\infty}^{\infty} dx \int_{-\infty}^{\infty} dy [\int_{-\infty}^{\infty} ds b(x,y)\delta(x\cos\theta + y\sin\theta - s)p(s,\theta)]$$

$$= \int_0^{\pi} d\theta \int_{-\infty}^{\infty} dx \int_{-\infty}^{\infty} dy b(x,y)p(x\cos\theta + y\sin\theta, \theta)$$

$$= \int_{-\infty}^{\infty} dx \int_{-\infty}^{\infty} dy b(x,y) \int_0^{\pi} d\theta p(x\cos\theta + y\sin\theta, \theta)$$

$$\equiv \langle b, \mathcal{B}p \rangle_u \tag{2.6}$$

Thus the backprojection operation is the adjoint of the projection operation. Which means

$$\langle \mathcal{P}b, p \rangle_u = \langle b, \mathcal{B}p \rangle_v \tag{2.7}$$

This relationship will hold for the discrete space case so that the backprojection transformation in a real finite-dimensional Hilbert space is simply $\mathbf{F^T}$. Thus, the conventional convolution (or filtered) backprojection reconstruction can be denoted by the following vector-matrix equation:

$$\underline{\tilde{b}}_1 = \mathbf{F^T R} \underline{p} \tag{2.8}$$

where $\mathbf{R}$ is the truncated-ramp filtering operation in matrix form. The physical interpretation of the above equation is as follows: filter the projections with kernel R and then backproject using the backprojection operator $\mathbf{F^T}$.

Another alternative solution or estimation for $\underline{b}$ is to use the Moore-Penrose (M-P) pseudoinverse denoted by the superscript(+). Using the M-P inverse,

$$\underline{\tilde{b}}_2 = \mathbf{F^+} \underline{p}. \tag{2.9}$$

The M-P inverse yields the minimum L_2 norm solution with the least-square error where the error=$\underline{e}$ is defined as:

$$\underline{e} = \underline{b} - \underline{\tilde{b}}_2. \tag{2.10}$$

The M-P inverse of a matrix $\mathbf{A}$ have the following relationships [32] [33] [34]:

$$\begin{aligned} 1)\quad \mathbf{A}\mathbf{A}^{+}\mathbf{A} &= \mathbf{A} \\ 2)\quad \mathbf{A}^{+}\mathbf{A}\mathbf{A}^{+} &= \mathbf{A}^{+} \\ 3)\quad \mathbf{A}\mathbf{A}^{+} &= [\mathbf{A}\mathbf{A}^{+}]^{\mathbf{T}} \\ 4)\quad \mathbf{A}^{+}\mathbf{A} &= [\mathbf{A}^{+}\mathbf{A}]^{\mathbf{T}} \end{aligned}$$

The M-P inverse can be found by using the singular value decomposition (SVD) of a matrix $\mathbf{F}$. Any matrix $\mathbf{F}$ can be decomposed as follows [35] [34]

$$\mathbf{F} = \mathbf{U}\mathbf{\Lambda}\mathbf{V}^{\mathbf{T}} \tag{2.11}$$

where $\mathbf{U}$ and $\mathbf{V}$ are unitary matrices with orthonormal columns $\underline{u}_j$ and $\underline{v}_j$ respectively and $\mathbf{\Lambda}$ is a diagonal matrix not necessarily square. The M-P inverse of $\mathbf{F}$ is simply

$$\mathbf{F}^{+} = \mathbf{V}\mathbf{\Lambda}^{+}\mathbf{U}^{\mathbf{T}}. \tag{2.12}$$

By using the definition of the M-P inverse and equation 2.12 the reconstruction equation can be made to look very similar to that of the conventional convolution backprojection.

$$\begin{aligned} \tilde{\underline{b}}_2 &= \mathbf{F}^{+}\underline{p} && (2.13) \\ &= \mathbf{F}^{+}\mathbf{F}\mathbf{F}^{+}\underline{p} \\ &= [\mathbf{F}^{+}\mathbf{F}]^{\mathbf{T}}\mathbf{F}^{+}\underline{p} \\ &= \mathbf{F}^{\mathbf{T}}[\mathbf{F}^{+^{\mathbf{T}}}\mathbf{F}^{+}]\underline{p} \\ &= \mathbf{F}^{\mathbf{T}}[\mathbf{U}\mathbf{\Lambda}^{+^{\mathbf{T}}}\mathbf{V}^{\mathbf{T}}\mathbf{V}\mathbf{\Lambda}^{+}\mathbf{U}^{\mathbf{T}}]\underline{p} \\ &= \mathbf{F}^{\mathbf{T}}[\mathbf{U}\mathbf{\Lambda}^{+^{\mathbf{T}}}\mathbf{\Lambda}^{+}\mathbf{U}^{\mathbf{T}}]\underline{p} \\ &= \mathbf{F}^{\mathbf{T}}\tilde{\mathbf{R}}\underline{p} && (2.14) \end{aligned}$$

where $\tilde{\mathbf{R}} = [\mathbf{U}\mathbf{\Lambda}^{+^{\mathbf{T}}}\mathbf{\Lambda}^{+}\mathbf{U}^{\mathbf{T}}]$. The above equation is identical to that of the conventional convolution backprojection reconstruction with the exception to the filtering

kernel $\tilde{\mathbf{R}}$.

The reconstruction approach taken by Baker [1] is given as follows: the pixelized reconstructed image is an approximation to the continuous space domain object described by the following equation:

$$b(x,y) \approx \sum_{mn} {B^T}_{mn}(x,y)c_{mn} \tag{2.15}$$

where ${B^T}_{mn}(x,y)$ defines the generalized pixels, and c_{mn}'s are the linear scaling or weighting factors for each pixel. The above equation can be expressed as

$$b \approx B^T \underline{c}. \tag{2.16}$$

The weighting factor c_{mn}'s is solved, in vector form, using the least-squares criterion given below:

$$\hat{\underline{c}} = \arg\min_{\underline{c}} \{||\underline{p} - FB^T\underline{c}||_2^2\} \tag{2.17}$$

where F was a projection formation operator that maps from a continuous space domain to a discretized projection space whose SVD is given as follows:

$$F = \mathbf{U}S \cdot V^T \tag{2.18}$$

where V^T is an unitary operator that simply rotates it's operand in the continuous space domain, S selects components from the operand in the continuous space and maps them to a discrete vector space, $\mathbf{U}$ is a finite dimensional unitary matrix. Baker chose a pixelization operator, B^T, such that the its basis set was orthonormal and governed by F. Baker's B is given as follows:

$$B = [(S \cdot S)^+]^{\frac{1}{2}} S \cdot V^T. \tag{2.19}$$

Solving the equation 2.17 for $\underline{c}$ yields

$$\hat{\underline{c}} = [(S \cdot S)^+]^{\frac{1}{2}} \mathbf{U^T} \underline{p}. \tag{2.20}$$

Substituting, the reconstructed image $\hat{\underline{b}}$

$$\hat{b} = V \cdot S^T (S \cdot S)^+ \mathbf{U^T} \underline{p}. \tag{2.21}$$

2.3 Optimization

Before delving into the specific case of PET image reconstruction a very important result will be presented here for the linear least-squares solution for a system with additive random noise vector to a stochastic signal vector shown in figure 2.4 below. The linear least-squares estimate (LLSE), $\hat{\underline{x}}$ (labeled in figure 2.4 as $\underline{y}$) is also the mmse estimate of $\underline{x}$ [36]. The LLSE of $\underline{x}$ is arrived at by applying a linear

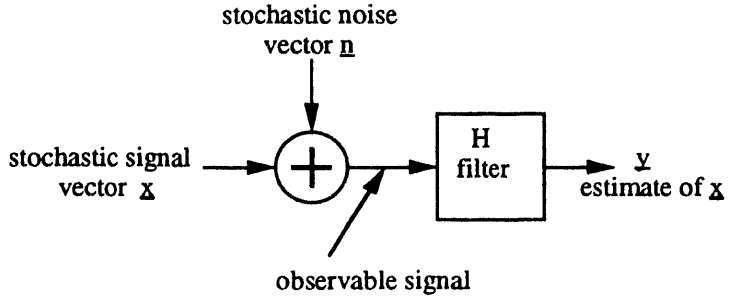

Figure 2.4: Generalized block diagram of filtering to produce mmse

transformation to the noisy vector $[\underline{x} + \underline{n}]$ such that

$$\underline{y} = \mathbf{H}(\underline{x} + \underline{n}). \tag{2.22}$$

The linear transform $\mathbf{H}$ expressed below in equation 2.33 is the generalized Wiener filter for all linear systems with additive noise. The result can then be applied to the problem of PET image reconstruction from noisy projection data set. $\mathbf{H}$ is solved using calculus of variations on $\mathbf{H}$. That is, let $\Delta\mathbf{H}$ be a perturbation to $\mathbf{H}$. Conditions on $\Delta\mathbf{H}$ is placed to insure that the cost function, mse,

$$\texttt{mse} = E||\underline{x} - \hat{\underline{x}}||_2^2 \tag{2.23}$$

is minimized to solve for $\mathbf{H}$ [37]. The solution proceeds as follows:

$$\mathbf{H} = \arg\min_{H}\{E||\underline{x} - \underline{y}||_2^2\} \tag{2.24}$$

where $\underline{y} = \mathbf{H}(\underline{x} + \underline{n})$. Consider $\mathbf{H} + \Delta\mathbf{H}$ and let $\underline{y} = (\mathbf{H} + \Delta\mathbf{H})(\underline{x} + \underline{n})$.

$$E||\underline{x} - \underline{y}||_2^2 = E[\underline{x} - (\mathbf{H} + \Delta\mathbf{H})(\underline{x} + \underline{n})]^T[\underline{x} - (\mathbf{H} + \Delta\mathbf{H})(\underline{x} + \underline{n})] \tag{2.25}$$

$$= E\{(\underline{x}^T(\mathbf{I}-\mathbf{H}^\mathbf{T}-\Delta\mathbf{H}^\mathbf{T})-\underline{n}^T\mathbf{H}^\mathbf{T}-\underline{n}^T\Delta\mathbf{H}^\mathbf{T})((\mathbf{I}-\mathbf{H}-\Delta\mathbf{H})\underline{x}-\mathbf{H}\underline{n}\Delta\mathbf{H}\underline{n})\} \quad (2.26)$$

$$\begin{aligned} &= E||(\mathbf{I}-\mathbf{H})\underline{x}-\mathbf{H}\underline{n}||_2^2 + E||\Delta\mathbf{H}(\underline{x}+\underline{n}||_2^2 \\ &-2E\{[\underline{x}^T(\mathbf{I}-\mathbf{H}^\mathbf{T})-\underline{n}^T\mathbf{H}^\mathbf{T}]\mathbf{H}^\mathbf{T}(\underline{x}+\underline{n})\} \end{aligned} \quad (2.27)$$

The first term in the above equation is a constant with respect to $\Delta\mathbf{H}$. The second term is a quadratic in $\Delta\mathbf{H}$ and the third term is linear in $\Delta\mathbf{H}$. The entire quadratic equation achieves a minimum when the linear term reaches zero [38] [39].

$$\Rightarrow E\{[\underline{x}^T(\mathbf{I}-\mathbf{H}^\mathbf{T})-\underline{n}^T\mathbf{H}^\mathbf{T}]\Delta\mathbf{H}^\mathbf{T}(\underline{x}+\underline{n})\}=0 \quad (2.28)$$

Now, let $\underline{z}_1^T = \underline{x}^T(\mathbf{I}-\mathbf{H}^\mathbf{T})-\underline{n}^T\mathbf{H}^\mathbf{T}$, $\underline{z}_2 = (\underline{x}+\underline{n})$ and $\mathbf{A}=\Delta\mathbf{H}$. Then, the above equation can be expressed as

$$E\underline{z}_1^T\mathbf{A}\underline{z}_2 = 0 \quad (2.29)$$

$$E\underline{z}_1^T\mathbf{A}\underline{z}_2 = E\sum_i^j z_{1i}A_{ij}z_{2j} = 0$$

Now, a relationship between $\underline{z}_1$ and $\underline{z}_2$ in equation 2.29 can be derived for for any $\mathbf{A}$. Consider

$$\mathbf{A}: A_{ij} = \begin{cases} 1 & i=m,n \\ 0 & otherwise \end{cases}$$

$$\Rightarrow E\underline{z}_{1m}\underline{z}_{2n} = 0 \quad (2.30)$$

$$\Rightarrow E\underline{z}_1\underline{z}_2^T = 0 \quad (2.31)$$

$$E\{[(\mathbf{I}-\mathbf{H}^\mathbf{T})\underline{x}-\mathbf{H}\underline{n}](\underline{x}^T+\underline{n}^T)\}=0 \quad (2.32)$$

$$E\{\underline{x}\underline{x}^T-\mathbf{H}\underline{x}\underline{x}^T+\underline{x}\underline{n}^T-\mathbf{H}\underline{x}\underline{n}^T-\mathbf{H}\underline{n}\underline{x}^T-\mathbf{H}\underline{n}\underline{n}^T\}=0$$

For the additive Gaussian model of equation 2.4 $E\underline{n}=0$ and $\underline{x}$ is independent from $\underline{n}$. So,

$$\Rightarrow \mathbf{H} = \mathbf{R}_{xx}[\mathbf{R}_{xx}+\mathbf{R}_{nn}]^{-1} \quad (2.33)$$

Section 2.2 discussed possible methods to estimate $\underline{b}$ from the equation

$$\underline{p} = \mathbf{F}\underline{b}.$$

However, in practical PET data there is measurement noise. Thus, instead of solving the above equation a more realistic equation to use is the following:

$$\underline{p}' = \mathbf{F}\underline{b} + \underline{n}. \tag{2.34}$$

where $\underline{n}$ is the additive noise in vector form.

The main source of the measurement noise is due to the Poisson nature of the radioactive tracer decay. Obviously, the dosage of the tracer a patient receives must be made low and the amount of time a patient can remain still while being scanned both contribute to the limited amount of radionuclide decay that can be measured. Other sources of noise include Compton scattering of photons within a patient and also scattering of photons in a detector crystal causing a neighboring crystal to scintillate and falsely detecting a photon. Another source of noise comes from crystal penetration where a high energy photon penetrates through a crystal without causing a scintillation to occur but the secondary crystal scintillates thus falsely determining that the photon had hit the secondary crystal first. The correction of this noise source was investigated by Huesman, et al [40]. Blurring due to the positron range was investigated and corrected by Haber [41]. Other sources which contribute to low SNR are things like crystal deadtime where typically several hundred milliseconds must pass before a detector crystal can scintillate again and when neighboring crystals simultaneously detect a photon. Due to the limitation in the electronics a coincidence window of ten nanoseconds is used to determine whether a photon pair was emitted from a single source. If, however, two neighboring crystals simultaneously receive photons the electronics cannot determine which photon pairs struck which pair of detectors. Thus, all such coincident photons are thrown out. All of the above contribute to limited statistics of a particular PET data set and hence cause the SNR to degrade.

Since measurements contain noise and the $\mathbf{F}$ matrix is singular, the equation $\underline{p}' = \mathbf{F}\underline{b} + \underline{\mathrm{n}}$ is not deterministic nor is there a unique $\underline{b}$ which satisfy the equation. Thus, only an estimate of the unknown, $\underline{b}$, can be made. As stated in the first chapter, a mathematically tractable cost function of the mean-square error (mse) will be minimized in $\hat{\underline{b}}$, the estimate of the original object $\underline{b}$.

2.3.1 Filter for CBP reconstruction

One approach to minimizing the mse is to solve for a filter or operator, $\mathbf{H_1}$, in the system depicted by the block diagram below where the reconstruction block is the CBP operator denoted by $\mathbf{G}$, i.e. $\mathbf{G} = \mathbf{F^T R}$. In the block diagram, the

Block diagram of data acquistion, filtering and reconstruction

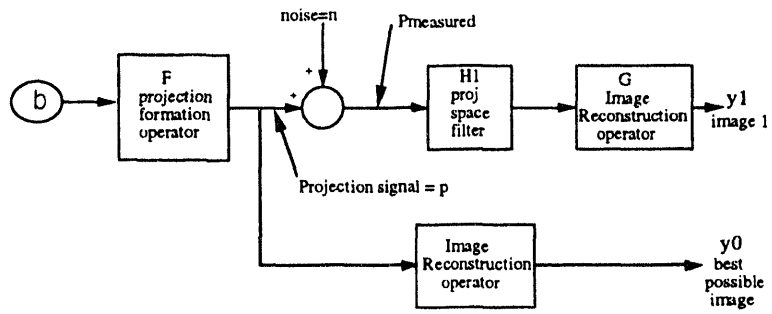

Figure 2.5: Block diagram of the data acquisition, pre-filtering the projections and reconstruction.

ideal reconstruction, or the best possible reconstruction is indicated by y_0 where reconstruction was done using noiseless projection data $\underline{p}$. The measured data, however, is filtered with $\mathbf{H_1}$ and then reconstructed. Thus, the LLSE of the best possible reconstruction is

$$\underline{y}_1 = \mathbf{G}\mathbf{H}_1\underline{p}' \tag{2.35}$$

where $\underline{p}'$ is the measured projection, $(\underline{p} + \underline{n})$. The mse cost function is the difference between the ideal reconstruction, $\underline{y}_0$, and $\underline{y}_1$. The same method of solving for $\mathbf{H}$ in the previous section of considering $\mathbf{H} + \triangle\mathbf{H}$ can be utilized again to solve the following:

$$\mathbf{H}_1 = \arg\min_{H_1}\{E||\underline{y}_0 - \underline{y}_1||_2^2\}. \tag{2.36}$$

Again, consider $\mathbf{H_1} + \triangle\mathbf{H}$ and let $\underline{y_1} = \mathbf{G}(\mathbf{H_1} + \triangle\mathbf{H})(\underline{p} + \underline{n})$.

$$E||\underline{y_0} - \underline{y_1}||_2^2 = E[\underline{y_0} - \mathbf{G}(\mathbf{H_1} + \triangle\mathbf{H})(\underline{p} + \underline{n})]^T[\underline{y_0} - \mathbf{G}(\mathbf{H_1} + \triangle\mathbf{H})(\underline{p} + \underline{n})] \tag{2.37}$$

$$= E||\mathbf{G}(\mathbf{I}-\mathbf{H_1})\underline{p}-\mathbf{G}\mathbf{H_1}\underline{n}||_2^2 + E||\mathbf{G}\,\Delta\,\mathbf{H}(\underline{p}+\underline{n}||_2^2$$
$$-2E\{[\underline{p}^T(\mathbf{I}-\mathbf{H_1^T})-\underline{n}^T\mathbf{H_1^T}]\mathbf{G^T}\mathbf{G}\,\Delta\,\mathbf{H}(\underline{p}+\underline{n})\} \tag{2.38}$$

As before, setting the linear term in $\Delta\mathbf{H}$ to zero,

$$E\{[\underline{p}^T(\mathbf{I}-\mathbf{H_1^T})-\underline{n}^T\mathbf{H_1^T}]\mathbf{G^T}\mathbf{G}\,\Delta\,\mathbf{H^T}(\underline{p}+\underline{n})\}=0 \tag{2.39}$$

Now, let $\underline{z}_1^T = \underline{x}^T(\mathbf{I}-\mathbf{H_1^T})-\underline{n}^T\mathbf{H_1^T}\mathbf{G^T}\mathbf{G}$, $\underline{z}_2=(\underline{p}+\underline{n})$ and $\mathbf{A}=\Delta\mathbf{H}$. Which leads to $E\underline{z}_1\underline{z}_2^T=0$ and

$$E\{\mathbf{G}\mathbf{G^T}[(\mathbf{I}-\mathbf{H_1})\underline{p}-\mathbf{H_1}\underline{n}][\underline{p}+\underline{n}]^T\}=0 \tag{2.40}$$

With the same assumption as before ($\underline{p}$ independent of $\underline{n}$) we arrive at

$$\mathbf{H_1}=\mathbf{R}_{pp}[\mathbf{R}_{pp}+\mathbf{R}_{nn}]^{-1} \tag{2.41}$$

Which is identical to the generalized Wiener filter. It should be noted that even though $\mathbf{G}=\mathbf{F^T}\mathbf{R}$ for this above derivation, the filter $\mathbf{H_1}$ is not a function of $\mathbf{G}$ so for any linear reconstructor $\mathbf{G}$, the above $\mathbf{H_1}$ will satisfy the optimization requirement in equation 2.36.

An alternative approach for solving this problem is depicted in the block diagram below. The only difference between this second approach and the first is the placement

Block diagram of data acquistion, reconstruction and filtering

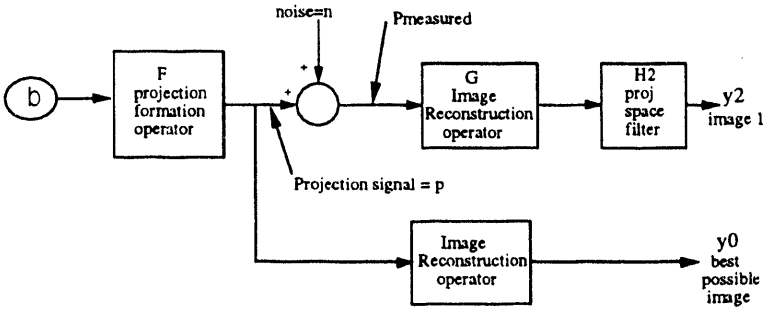

Figure 2.6: Block diagram of post filtering the reconstructed image.

of the Wiener filter block. As can be seen, the second approach filters reconstructed

image rather than filtering the projections before reconstruction. The LLSE of the best possible reconstruction now becomes

$$\underline{y_2} = \mathbf{H_2 G} \underline{p'} \tag{2.42}$$

where $\underline{p'}$ is the measured noisy projection. Using the same method as the two previous cases, $\mathbf{H_2}$ can be solved.

$$\mathbf{H_2} = \arg\min_{H_2} \{E||\underline{y_0} - \underline{y_2}||_2^2\} \tag{2.43}$$

where $\underline{y_2} = \mathbf{H_2 G}(\underline{p} + \underline{n})$. Consider $\mathbf{H_1} + \Delta\mathbf{H}$ and let $\underline{y_2} = (\mathbf{H_2} + \Delta\mathbf{H})\mathbf{G}(\underline{p} + \underline{n})$.

$$E||\underline{y_0} - \underline{y_2}||_2^2 = E[\underline{y_0} - (\mathbf{H} + \Delta\mathbf{H})\mathbf{G}(\underline{p} + \underline{n})]^T[\underline{y_0} - (\mathbf{H} + \Delta\mathbf{H})\mathbf{G}(\underline{p} + \underline{n})] \tag{2.44}$$

$$\begin{aligned} &= E||(\mathbf{I} - \mathbf{H_2})\mathbf{G}\underline{p} - \mathbf{H_2 G}\underline{n}||_2^2 + E||\Delta\mathbf{H_2 G}(\underline{p} + \underline{n})||_2^2 \\ &\quad -2E\{[\underline{p}^T\mathbf{G}(\mathbf{I} - \mathbf{H_2^T}) - \underline{n}^T\mathbf{G^T H_2^T}]\Delta\mathbf{H}\mathbf{G}(\underline{p} + \underline{n})\} \end{aligned} \tag{2.45}$$

Setting the linear term in $\Delta\mathbf{H}$ to zero,

$$E\{[\underline{p}^T\mathbf{G}(\mathbf{I} - \mathbf{H_2^T}) - \underline{n}^T\mathbf{G^T H_2^T}]\Delta\mathbf{H}\mathbf{G}(\underline{p} + \underline{n})\} = 0. \tag{2.46}$$

Let $\underline{z_1}^T = [\underline{p}^T\mathbf{G}(\mathbf{I} - \mathbf{H_2^T}) - \underline{n}^T\mathbf{G^T H_2^T}]$, $\underline{z_2} = (\underline{p} + \underline{n})$ and $\mathbf{A} = \Delta\mathbf{H}\mathbf{G}$.

$$\Rightarrow E\{[(\mathbf{I} - \mathbf{H_2})\mathbf{G}\underline{p} - \mathbf{H_2 G}\underline{n}][\underline{p}^T + \underline{n}^T]\} = 0 \tag{2.47}$$

For $\underline{p}$ independent of $\underline{n}$,

$$\Rightarrow (\mathbf{I} - \mathbf{H_2})\mathbf{G}\mathbf{R}_{pp} - \mathbf{H_2 G}\mathbf{R}_{nn} = 0 \tag{2.48}$$

$$\Rightarrow \mathbf{H_2 G} = \mathbf{G}\mathbf{R}_{pp}[\mathbf{R}_{pp} + \mathbf{R}_{nn}]^{-1} \tag{2.49}$$

In general, $\mathbf{G}$ is singular and only a LLSE estimate of $\mathbf{H_2}$ is possible which is

$$\mathbf{H_2'} = \mathbf{G}\mathbf{R}_{pp}[\mathbf{R}_{pp} + \mathbf{R}_{nn}]^{-1}\mathbf{G}^+ \tag{2.50}$$

It is trivial to show that $\underline{y_1}$ and $\underline{y_2}$ (the reconstructions using $\mathbf{H_1}$ and $\mathbf{H_2}$, respectively) are equivalent if the reconstruction operator, $\mathbf{G}$, is invertible. However,

the linear reconstruction operators are not invertible because $\mathbf{F^T}$, the backprojection transformation, is singular which follows because $\mathbf{F}$ is singular. Thus, the two results shown above are not necessarily equivalent.

$\mathbf{H_2'}$ is only the least-squares approximation to the filter that achieves the mmse. Whereas the result of the first method achieves the mmse. Meaning that achieving mmse in the projection space results in the mmse in the final image. The resulting error pre-filtering, using $\mathbf{H_1}$, is always less than or equal the error which results from post-filtering with $\mathbf{H_2}$. The reason filtering in the image space does not necessarily produce the "best" result is that the dimension of the domain space of the linear reconstruction transform $\mathbf{G}$ is larger than the dimension of its range space. Another words, there is a loss of information when a signal undergoes the $\mathbf{G}$ transformation as the singular values of $\mathbf{G}$ that are zero cause the null space of $\mathbf{G}$ to be mapped to zero. The vectors that lie in the null space may contain information which can reduce the error. For example, if there are correlations between the vectors in the null space and the vectors not in the null space they will appear in terms of $\mathbf{R}_{pp}$ which in turn can reduce the error.

2.3.2 Filter for M-P Inverse

For the case of the reconstruction based on the M-P inverse and the SVD of $\mathbf{F}$, one can take advantage of the SVD structure to derive an elegant representation of the Wiener filter which boils down to the calculating weighting factors for the singular values of $\mathbf{F}$. The smaller the singular values (λ's), the more the corresponding noise can be amplified in the reconstruction. Thus, the weighting factors are used to control the amplification of the noise. This idea was first suggested by Shim and Cho [14] and later applied to magneto encephalography by Hughett [39]. Consider the block diagram pictured in figure 2.5. Instead of the reconstruction operator $\mathbf{G}$ being $\mathbf{F^T R}$,

let $\mathbf{G} = \mathbf{F}^+$. Now, the LLSE of the best possible reconstruction becomes

$$\underline{y}_1 = \mathbf{F}^+\mathbf{H}_1\underline{p}' \tag{2.51}$$

where $\underline{p}'$ is the measured noisy projection. Since $\mathbf{F}$'s domain space is spanned by $\mathbf{V}$, $\underline{b}$ can be decomposed in terms of $\underline{v}_k$'s, the right singular vectors of $\mathbf{F}$. Thus,

$$\underline{b} = \sum_{k=0}^{K-1} \beta_k \underline{v}_k = \mathbf{V}\underline{\beta} \tag{2.52}$$

Similarly, $\underline{n}$ can be decomposed in terms of $\underline{u}_j$'s, the left singular vectors of $\mathbf{F}$. Thus,

$$\underline{n} = \sum_{j=0}^{J-1} \eta_j \underline{u}_j = \mathbf{U}\underline{\eta} \tag{2.53}$$

Thus,

$$\underline{p}' = \underline{p} + \underline{n} = \mathbf{U}\mathbf{\Lambda}\mathbf{V}^{\mathbf{T}}\mathbf{V}\underline{\beta} + \mathbf{U}\underline{\eta} \tag{2.54}$$

$$\Rightarrow \underline{p}' = \mathbf{U}(\mathbf{\Lambda}\underline{\beta} + \underline{\eta}) \tag{2.55}$$

So,

$$\underline{y}_0 = \mathbf{F}^+\underline{p} \tag{2.56}$$

$$\underline{y}_0 = \mathbf{V}\mathbf{\Lambda}^+\mathbf{U}^{\mathbf{T}}\mathbf{U}\mathbf{\Lambda}\mathbf{V}^{\mathbf{T}}\mathbf{V}\underline{\beta} = \mathbf{V}\mathbf{I}_t\underline{\beta} \tag{2.57}$$

where $\mathbf{I}_t$ is a truncated identity matrix formed by $\mathbf{\Lambda}^+\mathbf{\Lambda}$.

$$\underline{y}_1 = \mathbf{F}^+\mathbf{H}_1\mathbf{U}(\mathbf{\Lambda}\underline{\beta} + \underline{\eta}) \tag{2.58}$$

From equations 2.33 and 2.36, $\mathbf{H}_1 = \mathbf{R}_{pp}[\mathbf{R}_{pp} + \mathbf{R}_{nn}]^{-1}$. Written in terms of $\mathbf{U}$ and $\mathbf{V}$,

$$\mathbf{H}_1 = \mathbf{U}\mathbf{\Lambda}\mathbf{R}_{\beta\beta}\mathbf{\Lambda}\mathbf{\Lambda}^+[\mathbf{R}_{\beta\beta} + \mathbf{R}_{\eta\eta}]^{-1}\mathbf{\Lambda}^+\mathbf{U}^{\mathbf{T}} \tag{2.59}$$

which can be expressed as

$$\mathbf{H}_1 = \mathbf{U}\mathbf{D}\mathbf{U}^{\mathbf{T}} \tag{2.60}$$

$$\Rightarrow \underline{y}_1 = \mathbf{V}\mathbf{\Lambda}^+\mathbf{D}(\mathbf{\Lambda}\underline{\beta} + \underline{\eta}) \tag{2.61}$$

where $\mathbf{D}$ is a diagonal matrix if β_j's and η_k's are independent. As stated in section 2.1, PET data is a collection statistically independent Poisson processes thus, it is

reasonable to assume η_k's and β_j's are independent as stated in section 2.1. Thus, $\mathbf{D}$ will be assumed diagonal with d_i as the diagonal elements. Now, $\mathbf{H_1}$ can solved by simply minimizing the mse, with the error being $\underline{e} = \underline{y_0} - \underline{y_1}$.

$$\Rightarrow \underline{e} = \sum_{k=0}^{K-1} \underline{v_k}[\beta_k - d_k(\beta_k + \frac{1}{\lambda_k}\eta_k)] \tag{2.62}$$

where K is the rank of $\mathbf{F}$. Thus,

$$E||\underline{e}||_2^2 = \sum_{k=0}^{K-1}\sum_{j=0}^{K-1}\{\underline{v_k}[\beta_k - d_k(\beta_k + \frac{1}{\lambda_k}\eta_k]^T\}\{\underline{v_j}[\beta_j - d_j(\beta_j + \frac{1}{\lambda_j}\eta_j]\} \tag{2.63}$$

But note that $\underline{v_k}$'s are orthogonal, thus

$$\underline{v_k}^T \cdot \underline{v_j} = \begin{cases} 1 & k = j \\ 0 & otherwise \end{cases}$$

Which leads to

$$E||\underline{e}||_2^2 = E\beta_k^2(1-d_k)^2 + E\frac{d_k}{\lambda_k}(1-d_k)\beta_k\eta_k + 2E\frac{d_k^2}{\lambda_k^2}\beta_k^2 \tag{2.64}$$

Now, solving for d_k's proceeds as

$$\frac{\partial E||\underline{e}||_2^2}{\partial d_k} = 0. \tag{2.65}$$

Which leads to

$$d_k = \frac{\lambda_k^2 E\beta_k^2}{\lambda_k^2 E\beta_k^2 + E\eta_k^2}. \tag{2.66}$$

Thus, the Wiener filter, $\mathbf{H_1}$ for the M-P inverse reconstruction is $\mathbf{UDU^T}$ with the diagonal elements of $\mathbf{D}$ being the d_k's above.

2.3.3 Filter for Natural Pixel Reconstruction

Using the orthonormal-natural pixels [1] for reconstruction, a similar filtering scheme is appropriate where a diagonal matrix, $\mathbf{D}$, acts to weigh the singular values

to achieve a mmse estimate. Thus, the filtered weighting factors for the natural pixels become

$$\hat{\underline{c}} = \mathbf{D}[(S \cdot S^T)]^{\frac{1}{2}}\mathbf{U^T}\underline{p}' \tag{2.67}$$

and the filtered reconstruction is

$$\hat{b} = V \cdot S^T\mathbf{D}(S \cdot S^T)^{+}\mathbf{U^T}\underline{p}' \tag{2.68}$$

where $\underline{p}' = \underline{p} + \underline{n}$, the measured projection.

As with the SVD reconstruction using square pixels in the previous discussion, $\underline{p}'$ can be written in terms of the left singular vectors of $\mathbf{F}$, $\mathbf{U}$.

$$b = V \cdot \beta. \tag{2.69}$$

So,

$$\underline{p}' = \mathbf{U}S \cdot V^T \cdot V \cdot \beta + \mathbf{U}\underline{\eta}) \tag{2.70}$$

Now, since $\mathbf{D}$ and $[(S \cdot S^T)]^{\frac{1}{2}}$ are both diagonal, they commute. So, the above equations can be written as

$$\hat{\underline{c}} = [(S \cdot S^T)]^{\frac{1}{2}}\mathbf{D}\mathbf{U^T}\mathbf{U}(S \cdot \beta + \underline{\eta}) \tag{2.71}$$

which leads to

$$\hat{\underline{c}} = [(S \cdot S^T)]^{\frac{1}{2}}\mathbf{D}(S \cdot \beta + \underline{\eta}) \tag{2.72}$$

and

$$\hat{b} = V \cdot S^T(S \cdot S^T)^{+}\mathbf{D}(S \cdot \beta + \underline{\eta}). \tag{2.73}$$

The above equation can be written as

$$\hat{b} = V \cdot S^T\mathbf{\Lambda'}\mathbf{D}(S \cdot \beta + \underline{\eta}) \tag{2.74}$$

where $\mathbf{\Lambda'} = (S \cdot S^T)^{+}$. This can be expressed as

$$\hat{b} = \sum_k v_k d_k(\beta_k + \frac{1}{\lambda_k}\eta_k) \tag{2.75}$$

where $\frac{1}{\lambda_k}$ is the diagonal element of $\mathbf{\Lambda'}$ and $\beta_k = (\beta_k : b = \sum_k v_k\beta_k)$. The above equation leads to the identical error equation ($e = b_o - \hat{b}$) as in equation 2.62 except

that v_k is now a function and not a vector. As in the previous case, $\mathbf{D}$ can be solved by minimizing $E||e||_2^2$, by differentiating $E||e||_2^2$ with respect to d_i, the diagonal elements of $\mathbf{D}$. Using the same assumption that the noise and signal are independent, the diagonal elements are

$$D_{ii} \equiv d_i = \frac{\lambda_i^2 E\beta_i^2}{\lambda_i^2 E\beta_i^2 + E\eta_i^2} \tag{2.76}$$

which is identical to the previous result. As stated in section 2.3.1, the Wiener filter is independent of reconstruction method as long as it is linear. Furthermore, error resulting from pre-filtering the projections is always less than or equal to post-filtering the reconstructed image.

2.4 Frequency Space Filtering

Spatial frequency filtering of 2-D signals such as a tomographic image is easily accomplished by applying the projection-slice theorem. The projection slice theorem states that the Fourier transform of the projection of the 2-D signal at angle θ is equal to the slice of the 2-D Fourier transform of the original image at angle θ [7] [42] [43]. An equivalent form of 2-D filtering is to apply the appropriate 1-D filters to the projections of the 2-D object followed by inverse Radon transforming the filtered projections. PET data lends itself to spatial-frequency filtering as the collected data are modeled to be projection measurements of the original object. Thus, applying 1-D noise-reduction filters to the PET projection data accomplishes spatial-frequency filtering of the reconstructed image.

In terms of the reconstruction equation,

$$\hat{\underline{b}} = \mathbf{F}^{\mathbf{T}}\mathbf{R}\underline{p} \tag{2.77}$$

the $\mathbf{R}$ is a linear shift-invariant (LSI) transform. LSI transforms have a special form when written in matrix form. Since LSI operation is equivalent to a convolution with

a filter kernel as expressed below

$$y(n) = \sum_i x(i)h(n-i), \tag{2.78}$$

it can easily be shown that a circulant matrix $\mathbf{H}$ operating on a vector $\underline{x}$ ($\underline{y} = \mathbf{H}\underline{x}$) is equivalent to the convolution operation described in equation 2.78. As can be seen from above, the structure of LSI operators are written as circulant matrices. Furthermore, because the signals being filtered are very sensitive to phase information (images signals are phase sensitive [44] [45]), the LSI filters must be zero phase operators. This means that the filter kernels are symmetric and real resulting their Fourier transforms being symmetric and real. This requirement makes the LSI operators to be not only circulant but also symmetric. A symmetric matrix, $\mathbf{A}$, has SVD which is in the form:

$$\mathbf{A} = \mathbf{U}\mathbf{\Lambda}\mathbf{U}^{\mathbf{T}}. \tag{2.79}$$

That is, the left and right singular vectors are equivalent as $\mathbf{A}^{\mathbf{T}}\mathbf{A} = \mathbf{A}\mathbf{A}^{\mathbf{T}}$ for $\mathbf{A} = \mathbf{A}^{\mathbf{T}}$. For LSI operators, the singular vectors $\underline{u_j}$ are simply sinusoids as $e^{(j\omega t)}$ are eigenfunctions for continuous LSI time-domain systems. As evidenced by the SVD of LSI operators the property of commutability exits amongst LSI transforms. Two LSI transforms $\mathbf{A_1}$ and $\mathbf{A_2}$ have SVD's shown below:

$$\mathbf{A_1} = \mathbf{U}\mathbf{\Lambda_1}\mathbf{U}^{\mathbf{T}} \tag{2.80}$$

$$\mathbf{A_2} = \mathbf{U}\mathbf{\Lambda_2}\mathbf{U}^{\mathbf{T}}. \tag{2.81}$$

$$\begin{aligned}\mathbf{A_1}\mathbf{A_2} &= \mathbf{U}\mathbf{\Lambda_1}\mathbf{U}^{\mathbf{T}}\mathbf{U}\mathbf{\Lambda_2}\mathbf{U}^{\mathbf{T}} \\ &= \mathbf{U}\mathbf{\Lambda_1}\mathbf{I}\mathbf{\Lambda_2}\mathbf{U}^{\mathbf{T}} \\ &= \mathbf{U}\mathbf{\Lambda_2}\mathbf{\Lambda_1}\mathbf{U}^{\mathbf{T}} \\ &= \mathbf{U}\mathbf{\Lambda_2}\mathbf{I}\mathbf{\Lambda_1}\mathbf{U}^{\mathbf{T}} \\ &= \mathbf{U}\mathbf{\Lambda_2}\mathbf{U}^{\mathbf{T}}\mathbf{U}\mathbf{\Lambda_1}\mathbf{U}^{\mathbf{T}}\end{aligned} \tag{2.82}$$

$$= \mathbf{A_2 A_1} \tag{2.83}$$

Applying the spatial-frequency noise-reduction filter to the projection can now be expressed as the following:

$$\hat{\underline{b}} = \mathbf{F^T R H} \underline{p}' \tag{2.84}$$

$$= \mathbf{F^T H R} \underline{p}' \tag{2.85}$$

where $\mathbf{H}$ is the spatial-frequency noise-reduction filter. The linear transform operator which results in the mmse estimate still applies to the above equation but $\mathbf{H}$ in the above equation must be LSI. This can only happen if $\mathbf{H} = \mathbf{R}_{xx}[\mathbf{R}_{xx} + 2\mathbf{R}_{xn} + \mathbf{R}_{nn}]^{-1}$ is circulant and symmetric. The above is true if each correlation term ($\mathbf{R}$'s) is circulant and symmetric. This places statistical constraints that the correlation of the signal and the noise amongst each other and between the two are functions of only the distance between the signal in question. In other words, the signal and the noise must be wide-sense stationary (WSS). The WSS requirement for the signal and noise was the original constraint used by Wiener [46] for his mmse producing filter.

Using the Gaussian model of equation 2.1 where the total signal is represented by x':

$$x' = x'' + N(0, \sqrt{Ex}) \tag{2.86}$$

with x being a WSS stochastic process a WSS model with additive independent noise can be used for the LSI Wiener filter. With the above model, the noise is independent from the signal and thus uncorrelated. It follows that the filter in Fourier spatial-frequency domain can be found by simply taking the 1-D Fourier transform of the first row of the $\mathbf{H}$ matrix. Since the kernel is

$$h(n) = r_{xx}(n)/[r_{xx}(n) + r_{nn}(n)] \tag{2.87}$$

where $r_{xx}(n)$ and $r_{nn}(n)$ are autocorrelation functions of the signal and noise, respectively. The Fourier transform of $h(n)$ results in the following:

$$H(\omega) = \frac{P_{xx}(\omega)}{[P_{xx}(\omega) + P_{nn}(\omega)]} \tag{2.88}$$

where $P_{xx}(\omega)$ and $P_{nn}(\omega)$ are the power spectral densities of the signal and noise, respectively.

Though the WSS constraint may be valid for short-time samples of voice signals, it is usually not a good assumption for projection measurements. This is made clear by considering the projection of a uniform circular disk which is just an elongated half circle. The mean value (in the projection space) of a uniform circular disk phantom with Poisson emission process would be exactly this elongated half circle and it is clear that this violates the WSS condition that the mean be constant and the correlation value be only a function of distance and not position. However, all conventional CBP reconstruction with noise-reduction filtering uses a LSI transform as it is the fastest method of reconstruction.

Chapter 3

Wiener filter implementation

The previous chapter outlined the derivation for the Wiener filter for three types of reconstructions. However, in each formulation the filter is a function of signal and noise statistics. This chapter discusses the method of estimating the power spectra of the noise and signal used for Wiener filter in the CBP reconstruction algorithm. The outline of the Wiener filter implementation is presented and the robustness of the estimation technique is discussed.

3.1 Power Spectral Density Estimation

The preceding chapter outlined the methods for mmse filtering but key ingredients in each of the three filters are still missing. All three versions of the Wiener filters are functions of the noise and signal statistics, namely the autocorrelation matrix (and the cross correlation matrix if the signal and noise are correlated). The two reconstructions based on SVD have Wiener filter representation which depend on autocorrelation of the both the signal and noise parameters. As for the convolution backprojection reconstruction, the filtering is done in the Fourier or frequency domain and the filter is a function of the power spectra of the noise and signal, which is merely

the Fourier transform of a row of the auto-correlation matrix. Up to this point, only the equations have been derived for these optimizing filters without considering how the noise and signal characteristics can be estimated.

The ironic problem with Wiener filtering is that one needs to know the signal and noise statistics in order for the filter output to be the mmse estimate of the signal. One ends up estimating the signal so that filter can be found to be used in making the LLSE of that same signal.

Since the CBP method is the most computationally practical reconstruction algorithm and also the most common algorithm, this chapter investigates how the power spectral densities (PSD's) of the noise and signal may be estimated. Tsui [13] applied the Wiener filter to X-ray CT data where the SNR is generally an order of magnitude better than that of PET. Using a simplistic approach to the estimation problem, Tsui followed the model of the projection as being similar to the model given in equation 2.4. That is, the projections were modeled as being signal plus an additive white noise which is independent from the signal. Furthermore, ergodicity of the mean and variance was assumed in the measured projections. Thus, all that was needed was to calculate the mean and the variance of each projection angle and the noise PSD was simply a white spectrum with the projection variance as its magnitude. Based on the additive independent Gaussian model, this method makes an unbiased estimate the noise power [47]. However, for PET data with a much poorer SNR this method can lead to the signal power estimates with a large variance. The variance of the noise estimate is distributed as χ^2_{4K+2} [48]. But for those frequencies where the signal power is small relative to the noise power, the error in the signal power estimates can become excessively large. As Penney, et al [49] has shown the performance of the Wiener filter is a strong function of how well the signal PSD can be estimated.

3.1.1 PSD Estimation Using Reprojections

The raw collected data, as described in section 2.1, is described with Poisson statistics. Equation 2.4, rewritten below models the first and second order statistics of a Poisson stochastic process.

$$p \sim Poisson(\lambda = Ep)$$

$$p' = p'' + N(\mu = 0, \sigma = \sqrt{Ep})$$

where $p'' = Ep$ and $N(\mu, \sigma)$ is a Gaussian with mean = μ and standard deviation = μ. That is, if p" is considered to be the signal and $N(0, \sqrt{Ep})$ is considered to be the noise, then the signal power to the noise power ratio is p" itself. Using this additive noise model is useful in heuristically describing the noise-reduction that occurs when an image is reconstructed with noisy projections.

Example: Point source

Consider this example: a point source positron emitter is placed at the center of the tomograph as shown in the figure 3.1.

The projection at angle θ, as shown in the figure will be

$$p'_\theta = p_o + n_\theta \tag{3.1}$$

for the center bin for all projection angles where n_θ is the noise component at angle θ. For a tomograph which samples projections at Θ angles, the reconstruction of this point source would be the following:

$$\hat{b} \approx \frac{1}{\Theta} \sum_\theta p'_\theta$$

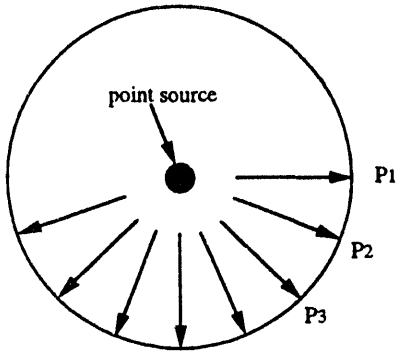

Figure 3.1: Example of a point source placed in the center of a tomograph and the projection measurements taken by the tomograph ring.

$$\hat{b} \approx p_o + \frac{1}{\Theta}\sum_{\theta} n_\theta. \tag{3.2}$$

The result of the reconstruction is an averaging effect of the Θ observations and hence the SNR is improved. The SNR in the image has improved by a factor of Θ as compared to the SNR in the raw projection space by simply reconstructing the image without applying any NR filters.

3.1.2 Noise in the Projections vs Image vs Reprojections

Based on the additive noise model, a rigorous calculation of the transformation of the noise between the raw measured projection space to the reconstructed image space without NR filtering is presented below. Again, consider the block diagram of the data acquisition process and a generic reconstruction process (designated by **G**) in figure 2.5.

The observable projection measurement is $\underline{p}' = \mathbf{F}\underline{b} + \underline{n}$, where $\underline{n}$ is the noise component. The covariance of the projection vector is simply the covariance of $\underline{n}$, based on the additive noise model where $\underline{b}$ is deterministic. The reconstructed image, therefore, is represented in vector form as $\mathbf{GF}\underline{b} + \mathbf{G}\underline{n}$. The covariance of the

reconstructed image is therefore

$$\mathbf{\Sigma_y} = cov(\underline{y}) = E[\underline{y} - E\underline{y}][\underline{y} - E\underline{y}]^T \tag{3.3}$$

$$\mathbf{\Sigma_y} = \mathbf{G}\mathbf{\Sigma_n}\mathbf{G^T} \tag{3.4}$$

where Σ_n is the covariance of $\underline{n}$. For a special case where the noise is zero-mean and independent, $\mathbf{\Sigma_n}$ is diagonal. Furthermore, if the noise is also identically distributed, $\mathbf{\Sigma_n} = \sigma^2\mathbf{I}$. That is, the covariance of the noise is a constant scalar equal to its variance multiplied by the identity matrix. Under the independent, identically distributed (IID) conditions, $\mathbf{\Sigma_y} = \sigma^2\mathbf{G}\mathbf{G^T}$. Thus, if the induced L_2 norm of $\mathbf{G}\mathbf{G^T}$ (or the largest singular value of $\mathbf{G}\mathbf{G^T}$ is less than unity, the induced L_2 norm of the covariance in the image space is less than the induced L_2 norm of the covariance in the projection space. Meaning, the noise is reduced in the image space.

Similar analysis can be carried out in the continuous domain for a LSI reconstruction operator with impulse response $G(f)$. However, instead of looking at the covariance matrices as in the discrete case above the PSD of the image can be written as a function the PSD of the projections. For a LSI operator having impulse-response function $H_{LSI}(f)$ and a WSS stochastic process input, the WSS output process' PSD is described as follows:

$$\Phi_{output}(f) = |H_{LSI}(f)|^2\Phi_{input}(f) \tag{3.5}$$

where $\Phi(f)$ denotes the PSD of a WSS process. It follows that

$$\Phi_y(f) = |G(f)|^2\Phi_p(f). \tag{3.6}$$

Now only the noise component in the projections so that the PSD in the projection is due to noise alone, i.e.

$$\Phi_p(f) = \Phi_n(f). \tag{3.7}$$

Hanson [50] has shown that the $|H_{LSI}(f)|^2$ for a CBP reconstruction along a radial line of the image is

$$|H_{CBP}(f)|^2 = \frac{\pi}{\Theta}|f||F^T(f)|^2 \tag{3.8}$$

where Θ is the number of projections and $F^T(f)$ is the impulse response of the backprojector which takes into account the interpolations that may exit in a back-projection algorithm.

The above equation indicates that if $|G(f)|^2$ is less than unity, the component of the reconstructed image due to noise will be attenuated as compared to the original noise component in the projection space. Hence, the SNR in the image will be improved over that of the projection space SNR.

Given $|G(f)|^2$ is less than unity for all f, one can extract a better estimate of the signal by studying the reconstructed image. The extraction of the better estimate of the signal in the imag. can be done by projecting the reconstructed image. The projections of the reconstructed image will be referred to as reprojections. The exact same analysis of the noise transformation from the original measured projection to the reprojection can be made by substituting the reconstruction-reprojection operator for $\mathbf{G}$. For the case of the convolution backprojection, the reconstruction is denoted by $\mathbf{F^T R}$ and the (re)projection by $\mathbf{F}$. Thus, substituting $\mathbf{FF^T R}$ for the $\mathbf{G}$ in equation 3.4, the covariance in the reprojection, $\underline{z}$, is

$$\mathbf{\Sigma_z = (FF^T R)\Sigma_n(FF^T R)^T} \tag{3.9}$$

which reduces to

$$\mathbf{\Sigma_z = \sigma^2 FF^T RR^T FF^T} \tag{3.10}$$

for the IID noise case. Again, if the largest singular value of $\mathbf{FF^T RR^T FF^T}$ is less than unity, the noise in the reprojection is reduced compared to the original measured projections.

Similar substitution for the continuous-space version can be made where $G(f)$ is substituted by $G'(f)$ which is the impulse response function of the reconstruction-reprojection operator. For a reprojection operator which is a true Radon transform, the reprojections represents the information in the reconstructed image. Thus, given that $|G'(f)|^2$ is less than unity, we have a tool to reduce the noise and to improve the SNR and a better estimate of the signal is possible by analyzing the reprojections. As an example, a uniform circular disk phantom will be used to illustrate the SNR improvement between the original noisy projections and it's reprojection.

A narrow-band (mid frequencies) noise was added to a set of ideal projections of a UCD phantom. A comparison between the norm square of the Fourier transform of the ideal projections, narrow-band noise added projections and the reprojections are shown in the graph pictured in figure 3.2. Comparing the graph of the reprojection and the original projection in the frequency band where noise was added the power of reprojection projection is attenuated by 60% compared to the original projection's power.

Similar experiment is carried out with Poisson data. Simulated projections for the UCD with Poisson statistics and its reprojections are pictured in figure 3.3. Again, the power in the reprojection is attenuated compared to the original projection.

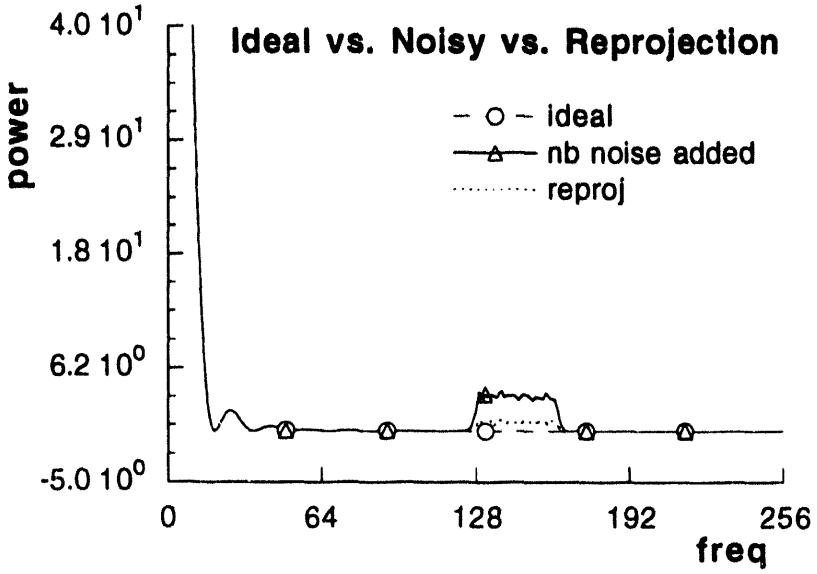

Figure 3.2: Comparison of the power between the ideal projections, narrow-band noise added projections, and the reprojections for a UCD phantom.

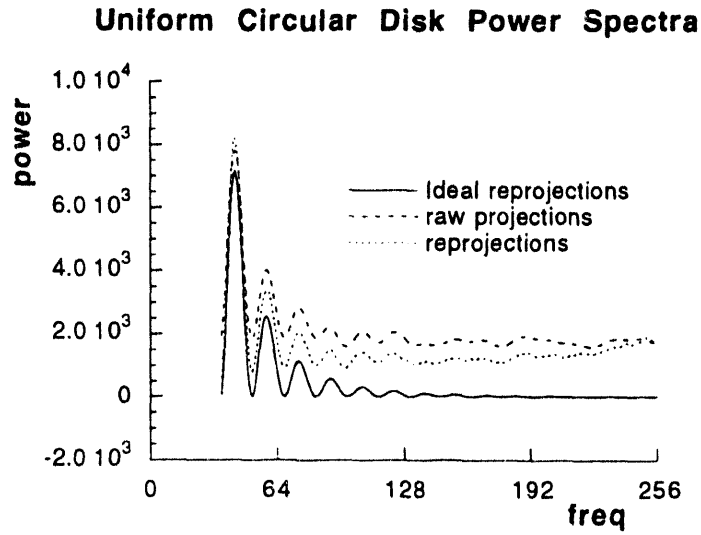

Figure 3.3: Comparison of the power between the ideal projection, simulated noisy projection (Poisson statistics), and its reprojection for a UCD phantom.

3.1.3 Using MTF priors to estimate PSD's

By looking at a block diagram representation of the data acquisition scheme which incorporates the non-ideal characteristics of the tomograph, shown below in figure 3.4, a very important information can be used to estimate the noise PSD. The modulation transfer function of the tomograph (MTF) is the impulse-response or point-spread function of the instrument. Though strictly speaking, the tomograph

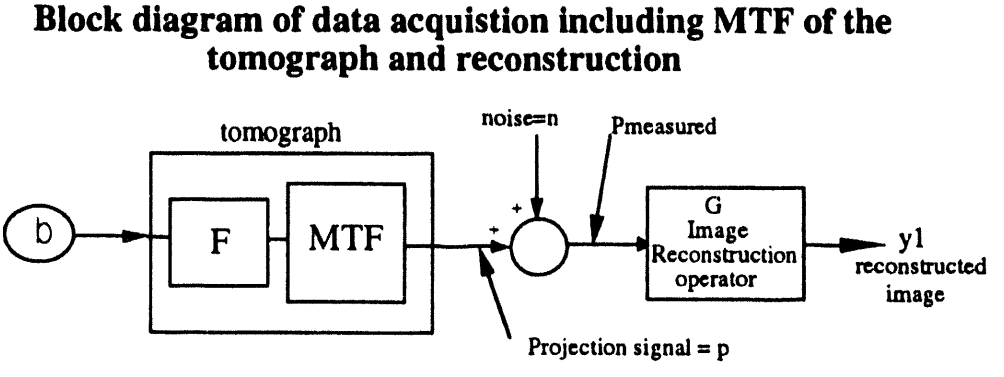

Figure 3.4: Block diagram of the data acquisition including the MTF of the tomograph.

is not shift invariant. The tomograph response is isotropic (rotationally invariant) [40] but radially varying. Furthermore, the response function for a detector pair is not shift invariant. The response of a detector pair to a positron-emitting source placed mid-way between the detectors is a Kronecker delta function whose height is a function of the point source location as indicated below [41] in figure 3.5. The response of the tomograph is governed by the physical limitation of the scintillator crystal (typically bismuth germanate [BGO]) [11] [51] [52]; both the physical dimension and the crystal's ability to scintillate before the high energy photon can either penetrate or scatter through to another crystal dictate the tomograph response characteristics.

However, useful analysis can be done making an engineering approximation of

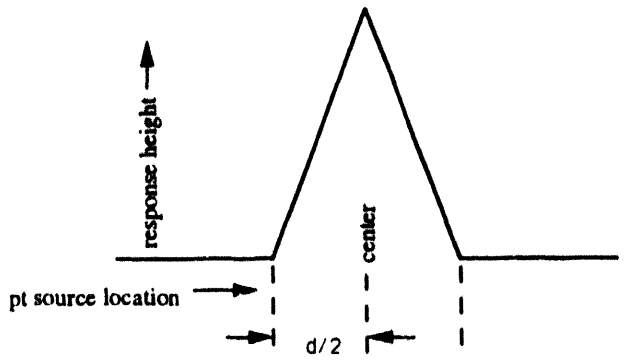

Figure 3.5: The height of the Kronecker delta response function of a detector pair in a tomograph as a function of point source location. where d is the width of a detector crystal (3mm for the Donner 600-crystal tomograph).

shift invariance and hence the response of the tomograph will be referred to as its MTF. When the MTF is measured by imaging a very small positron-emitting source the resulting reconstruction can be modeled as a narrow or "peaky" 2-D Gaussian. Taking the Fourier transform of the point spread function allows one to see the band width of the instrument. Figure 3.6 is the frequency domain representation (1-D) of the MTF.

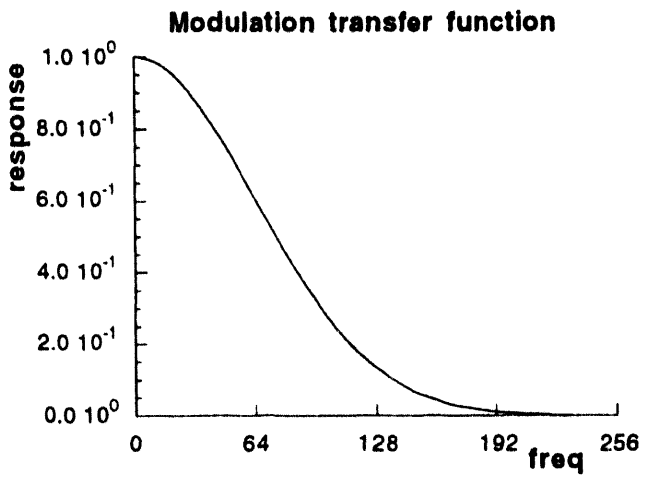

Figure 3.6: MTF of the Donner 600-crystal tomograph - the frequency axis is measured in frequency indices where index of 256 corresponds to the Nyquist limit equal to 6.67 cycles/cm.

As can be seen, the frequencies near the Nyquist rate the get attenuated by 60dB or more and thus the measured power in those high frequencies can be attributed to

noise alone. This suggests that one can estimate the average noise power in the high frequencies by merely looking at the total power in those frequencies.

Using the method of reprojecting the reconstructed image (without NR filtering), we can now proceed to implement the Wiener filter in conjunction with the CBP reconstruction. The reprojection vector, $\tilde{\underline{z}}$, is:

$$\tilde{\underline{z}} = \mathbf{F}\mathbf{F}^{\mathbf{T}}\mathbf{R}(\underline{p} + \underline{n}) \tag{3.11}$$

Now, let $\hat{\underline{p}}$ represent the estimate of $\underline{p}$ and $\hat{\underline{n}}$ denote the estimate of $\underline{n}$. Now, the estimate of the autocorrelation matrices, $\mathbf{R}_{pp}$ and $\mathbf{R}_{nn}$, will be

$$\hat{\mathbf{R}}_{pp} = \mathbf{K}E\underline{p}\underline{p}^{T}\mathbf{K}^{\mathbf{T}} \tag{3.12}$$

and

$$\hat{\mathbf{R}}_{nn} = \mathbf{K}E\underline{n}\underline{n}^{T}\mathbf{K}^{\mathbf{T}} \tag{3.13}$$

where

$$\mathbf{K} = \mathbf{F}\mathbf{F}^{\mathbf{T}}\mathbf{R}. \tag{3.14}$$

It follows that the Wiener filter using these estimates is

$$\hat{\mathbf{H}} = \mathbf{K}\mathbf{R}_{pp}\mathbf{K}^{\mathbf{T}}\mathbf{K}^{\mathbf{T}+}(\mathbf{R}_{pp} + \mathbf{R}_{nn})\mathbf{K}^{\mathbf{T}}. \tag{3.15}$$

The averaging effect of the reconstruction improves the SNR and hence the variance in the estimate of the autocorrelation matrices. The price to be paid is that the resultant estimates become biased. However, the finer the sampling done by $\mathbf{F}$ the better $\mathbf{F}^{\mathbf{T}}\mathbf{R}$ approximates it's true inverse and smaller the resultant bias introduced by $\mathbf{K} = \mathbf{F}\mathbf{F}^{\mathbf{T}}\mathbf{R}$. As will be demonstrated, for the Donner 600-crystal tomograph the bias introduced is minimal and very good estimates of the Wiener filter can be implemented.

To take advantage of the speed of the CBP reconstruction algorithm, we need to implement the Wiener filter in the frequency domain. Furthermore, we want to use the prior knowledge of the MTF of the tomograph to estimate the PSD of the noise. As before, using the WSS model of the signals the Wiener filter becomes a function of the PSD's. The PSD estimates are now done using the PSD of the reprojections.

The impulse response of $\mathbf{K} = \mathbf{F}\mathbf{F}^{\mathbf{T}}\mathbf{R}$, the reconstruction-reprojection operation one can be generated by Monte Carlo simulations; starting with white noise projections of known PSD reconstruct without a NR filter followed by projecting the reconstructed image. Repeating this operation five-hundred times and averaging over the five-hundred experiments, $|K(f)|^2$, the square of the impulse response can be found by the relationship

$$\Phi_{output}(f) = |K_{LSI}(f)|^2 \Phi_{input}(f). \tag{3.16}$$

The colorization of the noise term, $N(\mu = 0, \sigma = \sqrt{Ep})$, due to $|K_{LSI}(f)|^2$ is shown below on figure 3.7. The shape of the colorization curve reflects the impulse response of the projection and reconstruction algorithm; interpolations in the pixelization causes the curve to deviate from the ideal linear curve (as when $|F^T(f)|^2$ is unity in equation 3.8). It should be noted that this Monte Carlo simulation need only be done once. Once the colorization curve is determined for a particular set of reconstruction parameters (such as PWIDTH, number of angles, number of projection bins, reconstruction size, projector/backprojector operator), it can be stored as a look-up table and used for all reconstructions with the same parameters.

As stated earlier, the highest frequency components can be attributed to noise alone. Thus, the estimates of the noise PSD (corresponding to the $\mathbf{K}\underline{n}$ term) can be made by scaling the colorization curve shown on figure 3.7 such that a least-squares fit is achieved between the PSD of the reprojections and the scaled colorization curve. The graph on figure 3.8 depicts how the noise PSD term is estimated by normalizing the noise PSD curve to the PSD of the reprojection (signal + noise) over the upper frequency indices denoted by the hash marks. Once the noise power is determined, the signal power can be determined by subtracting the noise power from the PSD of the reprojection. Hence, the Wiener filter can be implemented by using these PSD estimates.

Determining how many of the highest frequency indices used for normalization depends on where the noise power begins to dominate over the signal power. The following two section discusses the choice the noise-power dominance parameter, the number of frequency indices used to perform the normalization.

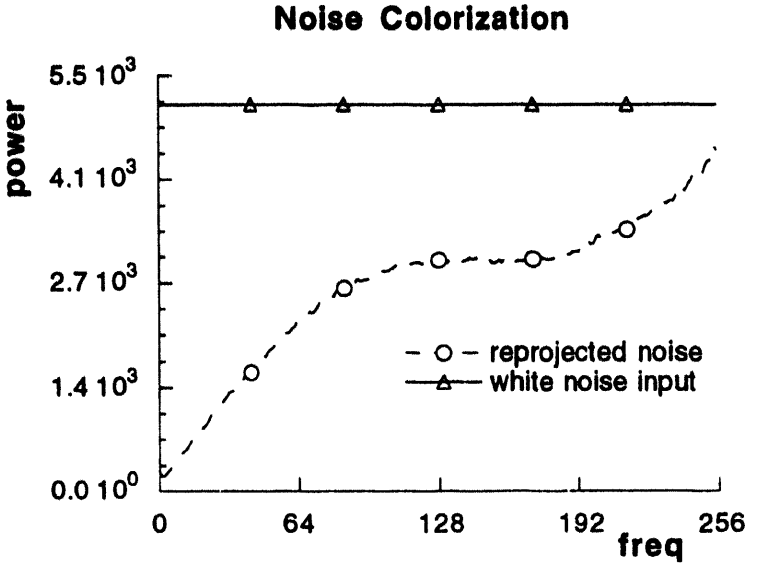

Figure 3.7: Transfer function between a white input noise source in the projection versus the colorized output of the reprojection. Frequency index of 256 is the Nyquist limit equal to 6.67 cycles/cm.

3.2 Outline of the Wiener filter implementation

A step by step outline of the Wiener filter is presented below: First, a colorization curve needs to be generated and kept as a look-up table for the Wiener filter routine. As indicated in the previous section, a Monte Carlo simulation (500 experiments were carried out as an example) of the reconstruction-reprojection operation is used to characterize how a white noise process is going to be transformed and thus correlated.

For a given tomograph data set and reconstruction routine an identically structured white noise projections need to be generated. For the example presented, the projections from the Donner 600-crystal tomograph has 300 angles with 201 projection bins per (angle for the clam-shut mode). The data is zero-padded to 512 to reduce aliasing when filtering and thus the white noise projections used to generate

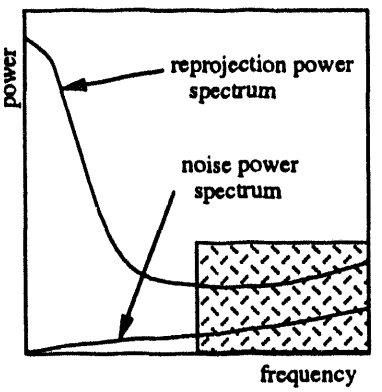

Figure 3.8: Illustration of how the noise PSD is estimated from reprojections and the noise colorization curve. After normalization, the noise power spectrum agree over the last m frequency indices.

the colorization curve for each Monte Carlo experiment has 300 vectors each with 512 white-noise elements. Picking the projector-backprojector pair used for the reconstructions (i.e. pll-bll, pin-bin, pll-bin, etc...), reconstruct the white-noise projections using a ramp filter and reproject the resultant white-noise induced image. The reprojections must be done at the same angles and the same number of projection bins. Determine the PSD in the reconstruction by calculating the mod-square of the Fourier transform of the reconstructions. Store the PSD of the reprojections. Repeat the experiment (500 times) and average the PSD over all experiments (500 experiments with 300 reprojections per experiment). The resultant average is the characteristic colorization curve which needs to be stored as a look-up table.

The implementation of the Wiener filter as a part of the CBP reconstruction is as follows. Start with the raw measured projections and reconstruct using only the ramp filter. Reproject the resultant image and determine the total PSD in the reprojections (mod-square of the Fourier transform of the reprojections). For each reprojection angle, determine the single normalization scale factor which when multiplied to the noise colorization curve results in the least-square error between the highest m frequency components of the reprojection and the noise power curve. The normalized noise power curve represents the estimate of the noise in each reprojection, and the difference between the total PSD of the reprojection and the noise power is the estimate of the signal power. The least-squares normalization calculation is car-

ried out as follows: let $\underline{P}_{repr}$ be the reprojection and $\underline{\hat{N}}$ be the characteristic colorized noise power. The error vector for the last m frequency indices (the noise-power dominance parameter) is simply $\underline{\epsilon_m} = \underline{P}_{repr-m} - \alpha\underline{\hat{N}}$. Solve for α which minimizes the norm of the error as follows:

$$||\underline{\epsilon_m}||_2^2 = \underline{\epsilon_m}^T\underline{\epsilon_m} \tag{3.17}$$

$$||\underline{\epsilon_m}||_2^2 = (\underline{P}_{repr-m} - \alpha\underline{\hat{N}}_m)^T(\underline{P}_{repr-m} - \alpha\underline{\hat{N}}_m)$$

$$\frac{d||\underline{\epsilon_m}||_2^2}{d\alpha} = -(\underline{\hat{N}}_m^T\underline{P}_{repr-m} + \underline{P}_{repr-m}^T\underline{\hat{N}}_m) + 2\alpha\underline{\hat{N}}_m^T\underline{\hat{N}}_m = 0 \tag{3.18}$$

$$\alpha = \frac{\underline{\hat{N}}_m^T\underline{P}_{repr-m}}{\underline{\hat{N}}_m^T\underline{\hat{N}}_m}. \tag{3.19}$$

$$\alpha = \frac{\sum_{i=M-m+1}^{M}\hat{N}(i)P_{repr}(i)}{\sum_{i=M-m+1}^{M}\hat{N}^2(i)} \tag{3.20}$$

where $i = M$ corresponds to the Nyquist frequency index. Thus, the estimate of the noise PSD becomes

$$\underline{N} = \alpha\underline{\hat{N}} \tag{3.21}$$

and the estimate of signal PSD becomes

$$\underline{S} = \underline{P}_{repr} - \alpha\underline{\hat{N}}. \tag{3.22}$$

Substituting the above for the Wiener filter,

$$H_W(f) = \frac{S(f)}{S(f) + N(f)} \tag{3.23}$$

where f is the frequency index.

Example: Ideal vs. Predicted

Using the Wiener filter generation outlined above, a Wiener filter was generated for a uniform circular disk with radius 16 pixels and a contrast ratio of 1:0 (background emits no counts). The graph depicted in the figure 3.9 compares the ideal Wiener filter generated from the known phantom geometry and the filter generated using the algorithm outline above.

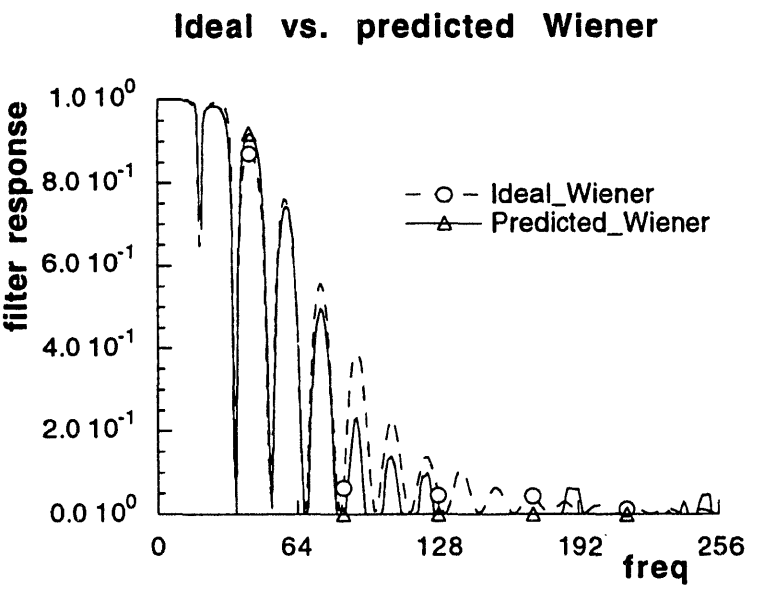

Figure 3.9: Comparison of an ideal Wiener filter and the Wiener filter generated by the outlined method. The filter is for an uniform circular disk phantom with a radius of 16 pixels.

3.3 Robustness of PSD Estimation Technique

In the previous section outlining the Wiener filter implementation the last m points of the reprojection PSD was used to calculate the normalization scale factor. As indicated in the graph of the tomograph MTF in figure 3.6, the tomograph attenuates the signal significantly at 50% of the Nyquist rate. In this section, a study of how the choice of m, the noise-power dominance parameter, effects the Wiener filter performance is done. For this purpose, simulation studies using a complex brain phantom generated by Llacer [20] which mimic the data set collected by the UCLA PET machine is used.

The description of the data set is as follows: each complete data set consists of 160 projection angles with 128 projection bins and the reconstructed image size is 128×128. Reconstructing the raw data results in a very small brain image and therefore a small PWIDTH value of 0.588 is chosen for the final reconstruction, consistent with the choice used by Llacer. There are 24 independent sets of projection data (24 X 160 projection angles with 128 bins) so that results of 24 independent experiments (reconstructions) could be averaged to produce better estimates. The image of the phantom is shown in the figures below.

The effect of the choice of m will be measured by 2 metrics: 1) a subjective measure of visual fidelity and 2) a quantitative measure of error determined by the standard deviation in a ROI in the reconstructed image. The values of m chosen for this study are 4, 8, 16, and 32. The 32nd highest frequency index corresponds to $f = 0.75 f_0$, or 75% of the Nyquist rate. The 4 images pictured below are typical reconstructions (1 of 24 data sets) with the varying value of m. The Wiener filter averaged over 160 angles for m = 4,8,16, and 32 is pictured in figure 3.14. ROI studies in two regions are done for this brain phantom — one in the high intensity region and another in a low intensity region. The quantitative results for the ROI studies are summarized in table 3.3.

As the table indicates, the quantitative error varies little with the choice of m. However, the image quality does show that there is more attenuation in the high

frequencies (marked by finer noise textures) with the higher m values, as predicted by the Wiener filter graphs.

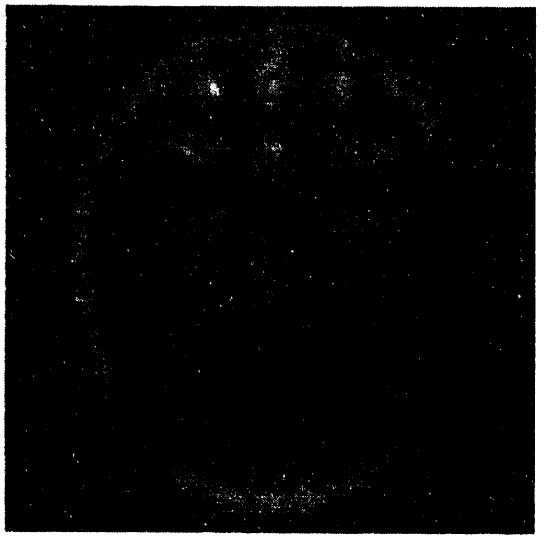

Figure 3.10: Wiener filter with the noise-power dominance parameter, m, equal to 4 to do the least squares fit.

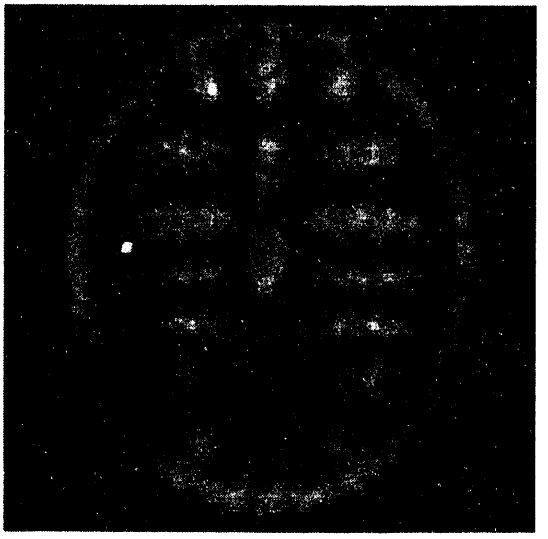

Figure 3.11: Wiener filter with the noise-power dominance parameter, m, equal to 8 to do the least squares fit.

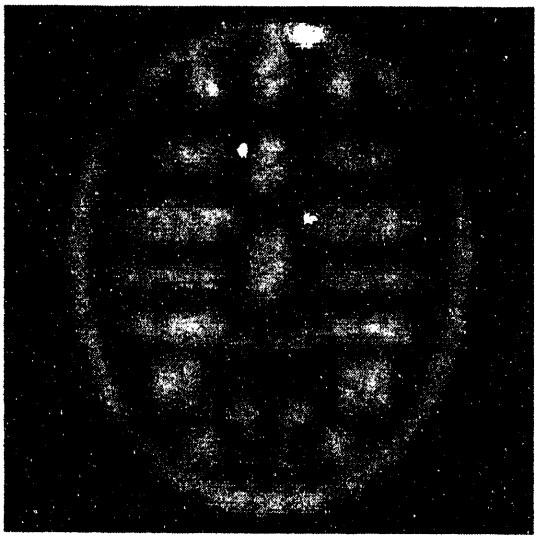

Figure 3.12: Wiener filter with the noise-power dominance parameter, m, equal to 16 to do the least squares fit.

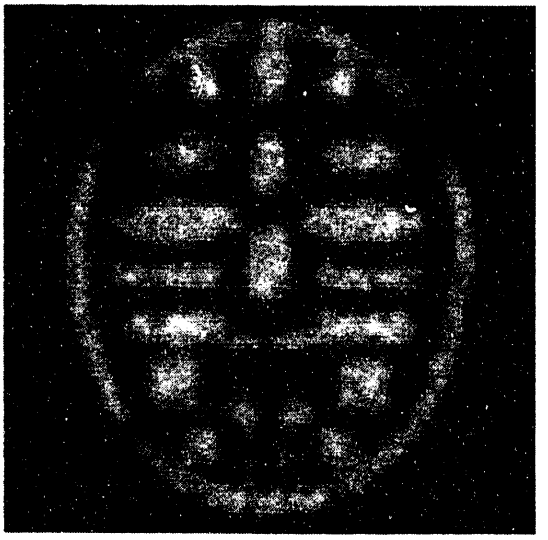

Figure 3.13: Wiener filter with the noise-power dominance parameter, m, equal to 32 to do the least squares fit.

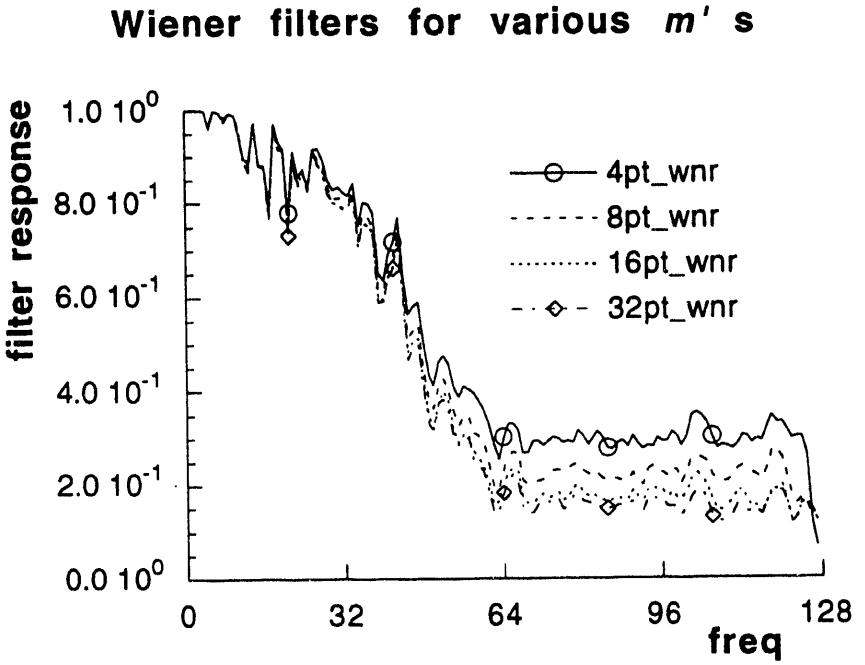

Figure 3.14: Comparison of the Wiener filter for 4 different noise-power dominance parameters: m = 4, 8, 16, and 32. The frequency index of 256 corresponds to the Nyquist rate equal to 6.67 cycles/cm.

Llacer brain phantom ROI studies					
reconstruction method	filter	Wiener m	ROI 1 σ (% of μ)	ROI 2 σ (% of μ)	μ_1/μ_2 ideal=4
CBP	Wiener	4	1.8%	7.4%	4.1
CBP	Wiener	8	1.8%	7.1%	4.2
CBP	Wiener	16	1.9%	7.4%	4.1
CBP	Wiener	32	1.9%	7.5%	4.1

Table 3.1: Summary of ROI statistics of the Llacer brain phantom. Wiener m corresponds to the highest m frequency indices used to perform the least squares fit to the noise curve. ROI 1 corresponds to the high intensity region and ROI 2 corresponds to the low intensity region.

Chapter 4

Results

In this chapter, results from simulations as well as experimental data will be presented. The first section describes results from simple geometric phantoms (uniform circular disk, uniform rectangle, and a ring surrounding a pair uniform rectangles of differing intensities) that are generated by software. The second section investigates the visual quality of the image as a function of the statistical error in the reconstruction. The third section studies a more complex brain phantom. Statistical error in reconstruction is presented and compared to reconstructions using the maximum likelihood estimate (MLE) and also CBP method with a Butterworth NR filter. Applying the same technique to experimental data taken from the Donner 600-crystal tomograph of a Hoffman brain phantom, the reconstruction results are presented in the fourth section.

4.1 Simulation Studies of Simple Phantoms

Using the algorithm outlined in the previous chapter for spectral estimation to be used in the Wiener filter, simulations will be studied to evaluate the performance of the Wiener NR filter. Phantom studies are carried out to simulate the Donner

600-crystal tomograph's data set. For each study, the projection data set consists of 300 projection angles with 201 projection bins (which simulates the clam shut mode) and the data possess Poisson statistics. The reconstructions are done using the RECLBL library and results in a 256×256 image. The PWIDTH parameter, the ratio between the pixel width and the projection bin width, is 1.0; the projector and backprojector are "pll" and it's adjoint "bll", respectively. The error will be quantitatively measured by determining the standard deviations in the regions of constant activity in each phantom. As before, 24 independent projection sets were generated for each phantom study so the quantitative results presented are averaged over 24 independent experiments.

Uniform circular disk (UCD) phantom, uniform rectangle phantom (URP), and a ring surrounding a pair of rectangle (RSR) phantoms of different intensities will be used as examples to compare the results of the Wiener filter with that of no NR (just ramp) filter and the Butterworth (BW) filter which were picked after manually iterating over the cut-off frequency and filter order to produce the "best" looking images. The BW filter in the RECLBL library is not restricted to having an integer filter order. The BW filter in the frequency domain is defined below

$$H_{BW}(f) = \frac{1}{\sqrt{1 + [\frac{f}{f_c}]^{2N}}} \tag{4.1}$$

where f is the frequency index, f_c is the cut-off frequency, and N is the filter order- not necessarily an integer. Aside from the flexibility of having adjustable parameters to shape the BW filter, another advantage of the BW filter is that it is zero phase. As stated in chapter 1 images are sensitive to phase information, thus, image restoration filters are generally zero phase filters. The general "rule of thumb" for picking the BW parameters go as follows: smaller the number of detected events the smaller the the cut-off frequency but higher the filter order. This makes intuitive sense as smaller the number of events the noisier the data set will be and the higher frequencies should be attenuated more and the attenuation should begin at a lower frequency. It should be noted that there is good correlation between the visually pleasing images and the quantitative measure of the standard deviation in the regions of interest (ROI's). It should also be noted that other NR filters are available in the RECLBL library (such

as the Hanning, Hamming, and Parzen filter) but the flexibility of the Butterworth filter by adjusting its two parameters allows it to resemble most other NR filters in shape and performance. Thus, the BW filter has been the NR filter of choice amongst the clinicians. Both quantitative results presented as the standard deviation in ROI's and the reconstructed images will be presented. For each phantom, three simulations will be presented — one with low statistics (250,000 detected events), one with medium statistics (500,000 events) and one with high statistics (2,000,000 events). The medium statistics cases simulate realistic counts for the Donner 600-crystal tomograph. For each phantom, the simulations are carried out for varying counts (number of detected events) to study the effects of differing effective intensities. For example, the uniform circular disk has a contrast ratio of 4:1 (foreground to background) and for the 250,000 (250k) event case the effective intensity in the UCD is about 10 events per pixel (before being scaled between 0 and 255, the 8-bit image display scale); for the 500,000 (500k) event case the effective intensity is about 20; and for the 2,000,000 (2M) event case it is about 80.

To simulate the data obtained from the Donner 600-crystal tomograph, 300 projection angles with 201 projection bins per angle are necessary. Simulated noisy projections for the uniform circular disk (UCD) were generated as follows. First, ideal projections were calculated analytically using the line-length algorithm [10]. The analytically determined projections are then passed bin by bin to a random number generator which outputs a realization of a Poisson process whose mean is the ideal projection.

4.1.1 Uniform circular disk example

The first simulation study is with the UCD whose contrast between the disk and the background is 4:1. The 250,000, 500,000, and 2,000,000 event simulations are given below. The UCD is centered in a 256×256 image with a radius of 64 pixels.

The resultant intensity (before being normalized to the 0 - 255 image display scale) in the UCD is about 10, 20 and 80 for the 250k, 500k, and the 2M event case, respectively. The ideal projections are identical for every angle since the UCD is isotropic (rotationally symmetric). The ideal projection is an elongated half circle shown below in figure 4.4 with simulated projection for a 500k event study overlaying the ideal projection. (The amount of elongation is linearly proportional to the intensity or height of the UCD.)

Figure 4.1 shows the original phantom. In figure 4.2 reconstruction results of the UCD in the absence of noise, or the best possible image given the reconstruction algorithm (which in this case is the CBP method with no NR filter). For the simulation done with 250,000 events, the reconstruction using the BW filter is shown in figure 4.5 and the Wiener filtered reconstruction is shown in figure 4.6. For this simulation, the Butterworth filter cut-off frequency is chosen to be 40% of the Nyquist rate, and the filter order was chosen to be 3.250. The comparison of the Butterworth filter and the Wiener filter (averaged over all 300 angles) is shown in figure 4.7.

The two ROI's are depicted in figure 4.14. Since the phantom is uniform, the two ROI's should have the same mean value and the standard deviation or be comparable. Results of the ROI studies are given in table 4.1.

The visual quality of the two (BW and Wiener-filtered) reconstructions are poor for this simulation. The foreground (the UCD phantom itself) is barely distinguishable from the background. Since the resultant intensity level is low and the contrast level is low the poor image quality is expected. However, the two images have distinct visual qualities; the BW-filtered version has large noise grains whereas the Wiener filtered version have very fine grains. This can be explained from the contrasting the two filters. The BW filter passes a lot more mid-frequencies and less of the highest frequencies as compared to the Wiener filter which has a relatively constant attenuation factor from frequency index of 40. The larger noise grains of the BW-filtered image occupy the mid-frequency spectrum and the fine grains of the Wiener-filtered image appear "white". The quantitative results for the two reconstruction show that the BW version performed slightly better than the Wiener reconstruction. The standard deviation in the ROI for the BW was roughly 135% of the mean while the Wiener

version had a standard deviation of about 158%. They both had relatively stable mean (or DC) values in the two ROI's.

The simulation studies for the UCD phantom with 500,000 detected events are presented below. The BW filtered reconstruction is shown in figure 4.8 and the Wiener filtered reconstruction is shown in figure 4.9. The Butterworth filter parameters for the 500,000 case was the following: cut-off frequency = 45% of the Nyquist rate and the filter order was 3.00. The comparison of the two filters is shown in figure 4.10. The quantitative results for the ROI studies are summarized in table 4.1.

The visual quality for the 500,000 event simulation was better due to the 3dB improvement in signal strength. However, the two reconstructed images still retain very distinct visual qualities much like that of the previous low statistic case. Since the overall filter shapes did not change too much from the previous case the images basically retained those same similar characteristics. However, the quantitative results show that the Wiener filter performs better as compared to the 250,000 event case. With the improved signal strength, the Wiener filter behavior becomes much more clearly dominated by the first-order Bessel function spectrum of the UCD projections. The humps in the low frequencies is analogous to the humps displayed in an earlier example figure 3.9 where the UCD had a much smaller diameter (and hence a much wider humps in the spatial frequency domain). The standard deviation for the BW version is about 106% whereas the Wiener version produces a standard deviation of about 111%. Again, the mean value in the ROI's were stable for both reconstructions.

The simulation studies for the UCD phantom with 2,000,000 detected events is presented below. The BW filtered reconstruction is shown in figure 4.11 and the Wiener filtered reconstruction is shown in figure 4.12. The Butterworth filter parameters for the 2,000,000 event case was the following: cut-off frequency = 55% of the Nyquist rate and the filter order was 3.00. Comparison of the two filters are given in figure 4.13. As stated earlier, with larger number of detected events, the SNR is improved and more spectral content can be passed through the low-pass NR filter and hence the cut-off frequency is made higher and the filter order made lower. The statistics from the ROI studies are summarized in table 4.1.

Again, the two reconstructed images display visual qualities similar to the lower statistics cases. That is, the noise in the Wiener reconstruction appear more white and thus more uniform whereas the BW reconstruction have much larger grains. With large number of events, the SNR is much improved and the the existence of humps in the lower frequencies is much more evident. Due to the improved SNR, the BW filter passes a lot more information as expected. The quantitative results show that the Wiener filter performs as well as the BW counter part for this high count simulation. The standard deviation in the ROI's for the Wiener is down to 52.5% of the mean and the BW version has standard deviation of about 55% of the mean. Again, the mean values are stable for both reconstructions.

It should be noted that the noise in the Butterworth reconstruction can vary significantly depending on the filter parameters. When the filter order is chosen too large, the resultant image contain miniature donut-shaped noise artifacts. If the cut-off frequency is chosen too high, the standard deviation in the ROI's become severely degraded. There are trade-offs in choosing the BW filter parameters. One of the short comings is that the BW filter roll-off rate is governed only by the filter order and is uniform when measured on a log-log scale (as it is an all-pole filter). Thus, the amount of attenuation increases with frequency and cannot be made to reach a constant level. With only the two degrees of freedom (filter order and cut-off frequency) the shape of the BW filter cannot be made to match the shape attained by the Wiener filter. This first set of simulations using the UCD favors the BW filtering approach since the ideal projections are identical from angle to angle. Thus, the same filter should be adequate to filter all projections. The next two simulations using nonisotropic phantoms show that the Wiener filter can outperform the BW filter.

The quantitative studies of the ROI's show that the error, measured in standard deviations as a percent of the ROI average, is reduced in the Wiener reconstructions. Furthermore, the lower the number of events, the better the BW filter performs. For the case with 250,000 events, the standard deviation in the ROI is about 160% of the mean for the Wiener and 130% for the Butterworth. For the case with 500,000 events, the standard deviation for the Wiener drops to about 110% and for the Butterworth, it drops to about 105%. For the case with high statistics of 2,000,000 events, the

standard deviation in the ROI's for the Wiener drops to 52% of the mean and for the Butterworth it drops to 55% of the mean. SNR improves with larger statistics and hence a better estimate of the signal is possible. With better estimates of the signal and noise PSD's, better estimates of the Wiener filter result which lead to better reconstructions.

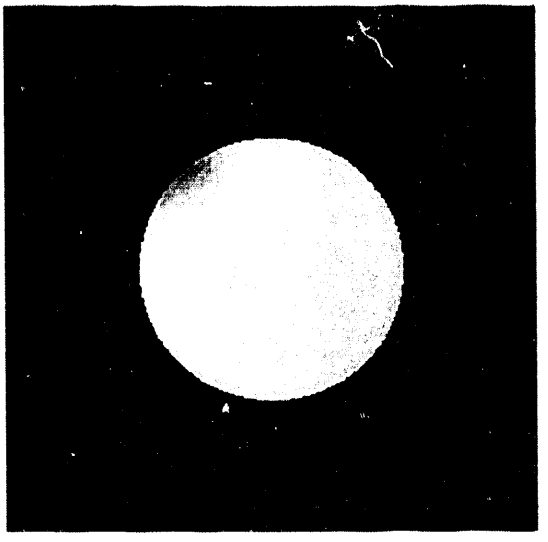

Figure 4.1: The UCD phantom centered on a 256×256 array with radius = 64 pixels.

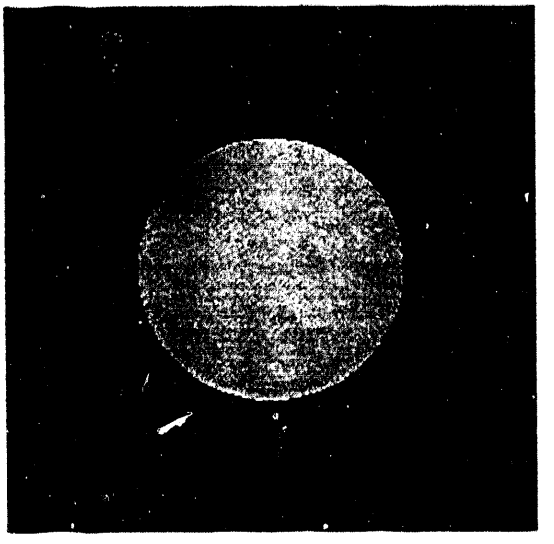

Figure 4.2: The best possible reconstruction, i.e. no noise case, for the CBP algorithm.

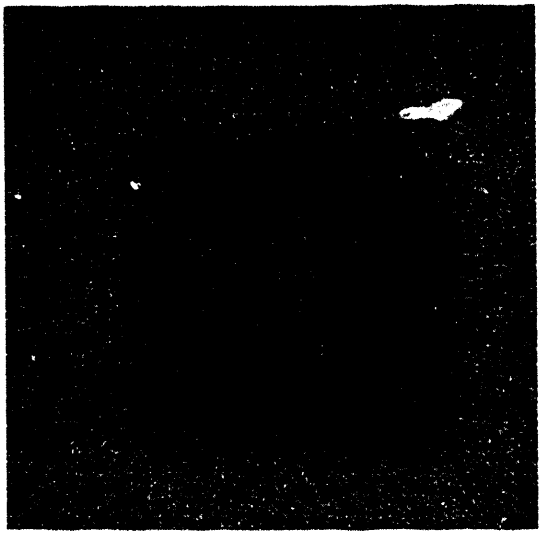

Figure 4.3: Reconstruction for a 500,000 event simulation without using any NR filters.

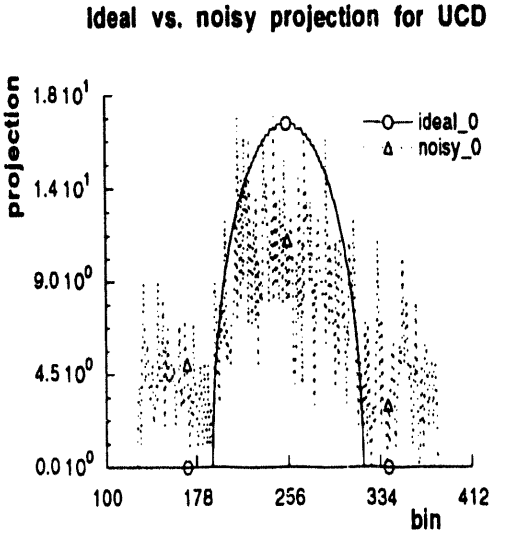

Figure 4.4: Ideal and simulated (500k events) projection for a UCD phantom.

Figure 4.5: BW ($f_c = 0.40 f_0$,N=3.25) filtered reconstruction of a 250k event UCD.

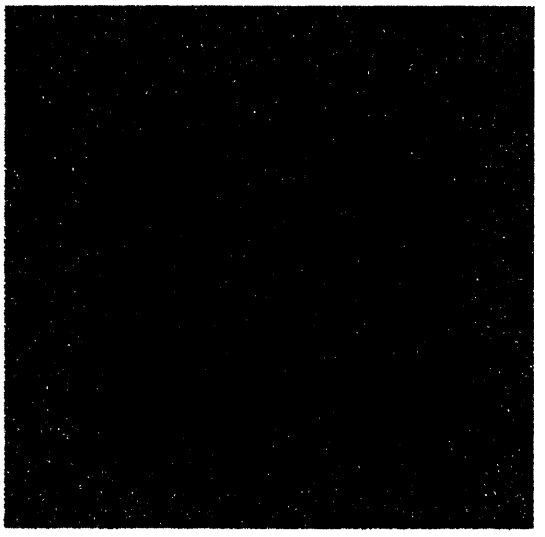

Figure 4.6: Wiener filtered reconstruction of the 250,000 event UCD phantom.

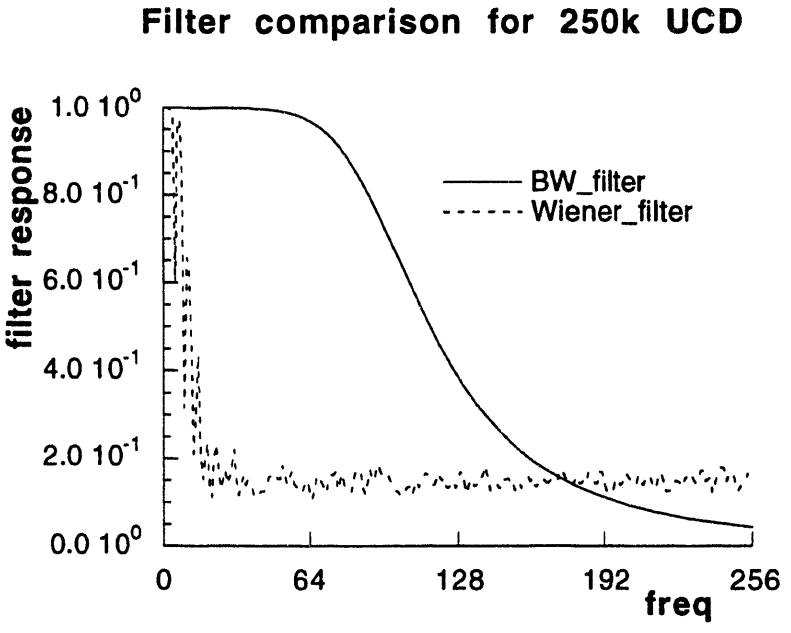

Figure 4.7: Comparison of the BW filter and the Wiener filter (averaged over all projection angles) used for the 250k event UCD reconstructions.

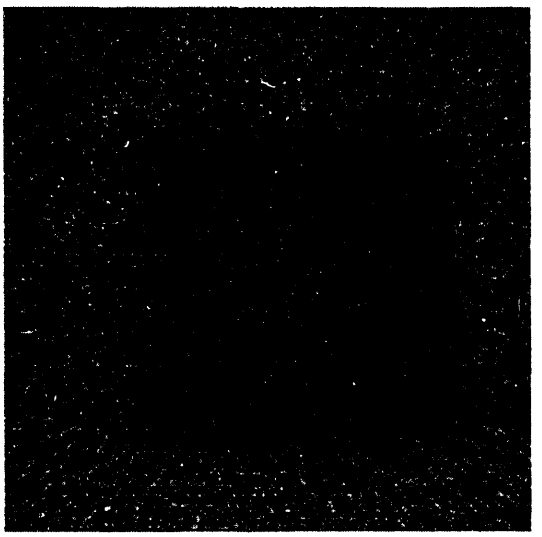

Figure 4.8: BW ($f_c = 0.45 f_0$,N=3.0) filtered reconstruction of a 500k event UCD

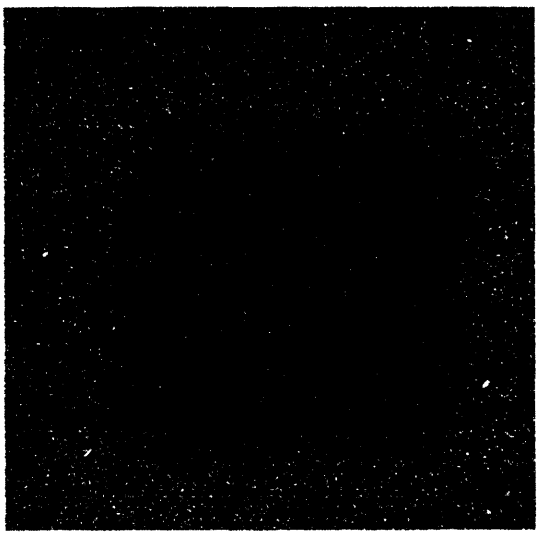

Figure 4.9: Wiener filtered reconstruction of the 500,000 event UCD phantom

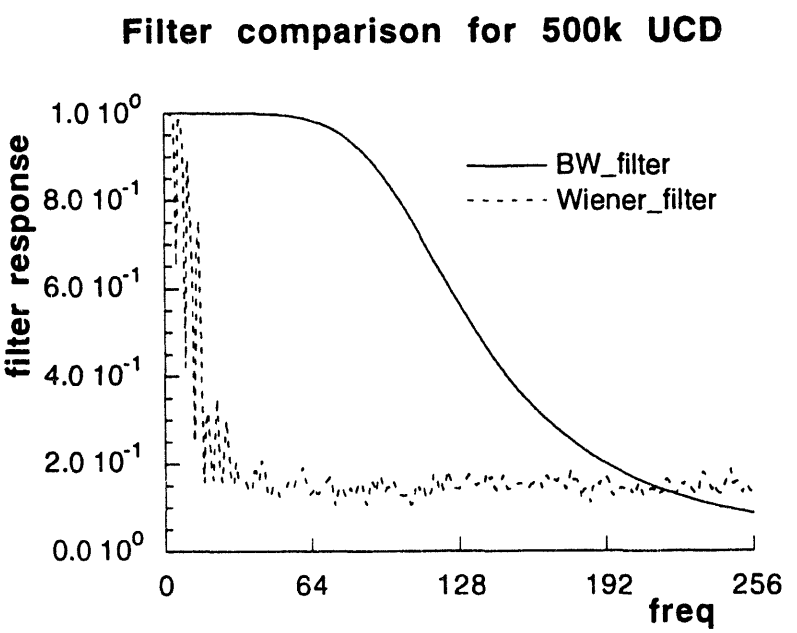

Figure 4.10: Comparison of the BW filter and the Wiener filter (averaged over all projection angles) used for the 500k event UCD reconstructions.

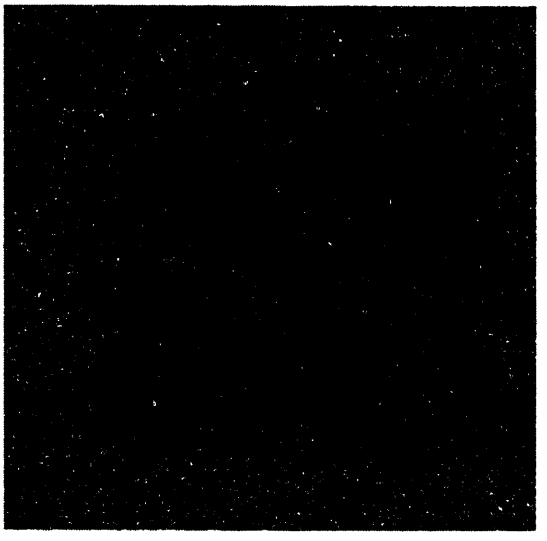

Figure 4.11: BW ($f_c = 0.55 f_0$,N=3.0) filtered result of a 2M event UCD

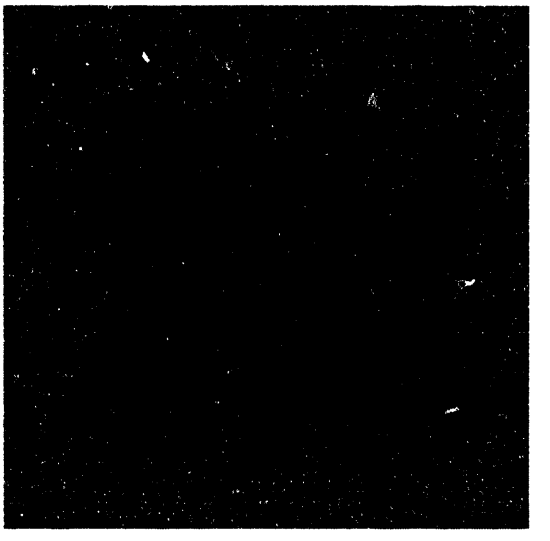

Figure 4.12: Wiener filtered reconstruction of a 2M event UCD phantom

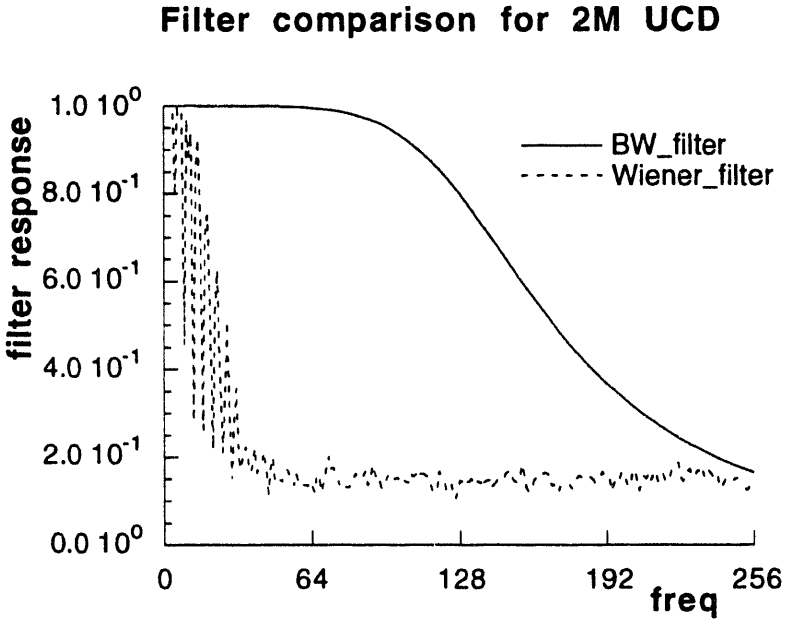

Figure 4.13: Comparison of the BW filter and the Wiener filter (averaged over all projection angles) used for the 2M event UCD reconstructions.

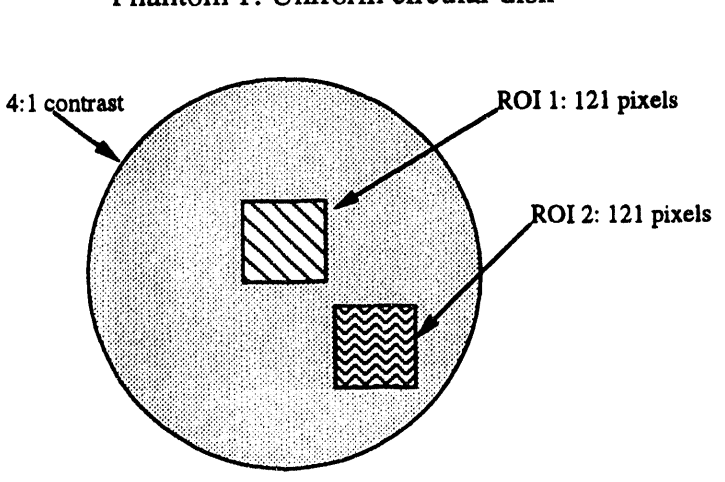

Figure 4.14: The UCD phantom is centered (128.5,128.5) on a 256×256 gridded array with a radius of 64 pixels. ROI 1 has its lower left corner at (128,123) and its upper right corner is at (138,133). ROI 2 has its lower left corner at (128,115) and its upper right corner is at (138,125).

Uniform circular disk phantom ROI studies						
number of events	filter type	BW param's		ROI 1	ROI 2	μ_1/μ_2
		f_c (% of f_o)	order	σ (% of μ)	σ (% of μ)	(ideal = 1)
250k	ramp			310%	320%	1.10
250k	BW	50%	3.25	130%	139%	1.05
250k	Wiener			160%	156%	0.99
500k	ramp			260%	268%	1.02
500k	BW	55%	3.05	105%	106%	1.00
500k	Wiener			112%	111%	1.01
2M	ramp			122%	125%	1.04
2M	BW	60%	3.00	54%	56%	1.02
2M	Wiener			52%	53%	1.02

Table 4.1: Summary of ROI statistics UCD phantom study. f_c and f_o are the cut-off frequency and the Nyquist rate, respectively. σ and μ are the standard deviation and mean of the ROI, respectively.

4.1.2 Uniform rectangle example

The Uniform rectangular phantom (URP) simulations is useful in demonstrating the adaptive nature of the Wiener filter. Since the rectangle is not isotropic (rotationally symmetric), the filter shape should change more dramatically than for the isotropic UCD. Figures 4.18 and 4.19 show the difference in the projections when the projections are measured at 0° and 90°, where the 0° is the projection measured north-to-south in the image and the angles are measured clock-wise. The rectangle is centered on a 256 X 256 image having a height of 86 pixels and width of 13 pixels. The contrast for this phantom is 6:1 as compared to 4:1 used in the UCD. The contrast ratio and the size of the phantom is such that the effective intensity (before normalization to the 0-255 image display scale) in the URP is about 20, 40, and 160 for the 250k, 500k, and 2M event cases respectively. The image of the original phantom is displayed on figure 4.15; the best possible reconstruction (no noise case) is on figure 4.16; an example of a reconstruction without using a NR filter (500k event simulation) is on figure 4.1.2; the ideal and simulated projections at 0° is on figure 4.18 and the 90° projections are on figure 4.19. The reconstructions and quantitative results are presented below.

For the 250k event simulation, the image quality is slightly better compared to that of the 250k UCD for both the Butterworth and the Wiener due to the 3dB improvement in the signal strength. The two reconstructions are placed side-by-side for comparison in figures 4.20 and 4.21. The noise in the reconstructed images has characteristics very similar to those of the 250k UCD simulations; the noise in the Butterworth filtered images is characterized by large grain sizes as compared to the Wiener. The Butterworth filter parameters for this case are: cut-off frequency = 55% of the Nyquist rate and the filter order is 3.50. The cut-off frequency is higher as compared to the UCD example for the same number of detected events due to the fact that the sinc function spectrum of the projections measured vertically has zero crossings that are wider than the of zero crossings of the Bessel function spectrum

of the UCD projections. The Wiener filter is displayed for two different projection angles: one at 0° and another at 90°. As can be seen, the filter shape is governed by spectrum of each projection angle. Since the 90° projection is a wide square pulse compared to the 0° projection, the sinc function spectrum of the 90° projection has zero crossings that occur more rapidly than the 0° projection. This can be seen in the close-up of the low-frequency portion of the Wiener filter shown on figure 4.29.

For the 500k event simulation, the Butterworth filter parameters are the following: cut-off frequency = 60% of the Nyquist and filter order is 3.1. Again, the BW filtered images had noise grains which were much larger causing larger false hot spots to appear. Figure 4.23 and 4.24 are the reconstructed images and figure 4.25 show the Wiener filter at two different angles.

For the 2M event simulation, the Butterworth filter parameters are the following: cut-off frequency = 64% of the Nyquist and filter order is 3.00. With the expected value of the intensity (before scaling to 0 - 255) being around 160 the SNR approximately being $\sqrt{160}$ = 22dB the two reconstructed images look much less noisy and the image quality is good for both reconstructions.

As with the simulations using UCD phantom, the BW filter parameters varied according to the number of detected events. With improving SNR, the cut-off frequency is made higher and filter order made smaller. As explained in the UCD section, the shape of the BW cannot be made to look similar to outline of the Wiener filter. If the parameters are chosen the mimic the outline of the Wiener in the low frequencies, the BW filter would end up over attenuating the mid to high frequencies causing the result image to have blurred edges as well as having an a image quality similar to that of looking at an image through ground or etched glass.

The two ROI's for the URP simulation is illustrated in figure 4.30 and the summary of the ROI statistics is presented in the table 4.2. Quantitatively, the Wiener filter performed better for this non-isotropic phantom as compared to the isotropic UCD. The BW filtered images and the Wiener filtered images resulted in having nearly identical standard deviations in the ROI for the all three cases despite the remarkably different image appearances. For the low statistics case: $\sigma \approx 70\%$. For the medium statistics case: $\sigma \approx 50\%$. For the high statistics case: $\sigma \approx 25\%$.

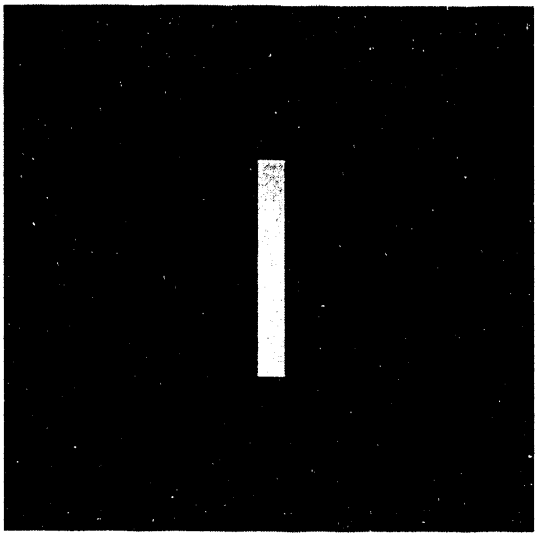

Figure 4.15: The URP has height=86 pixels and width=13 pixels.

Figure 4.16: The best possible reconstruction, i.e. no noise case, for the CBP algorithm.

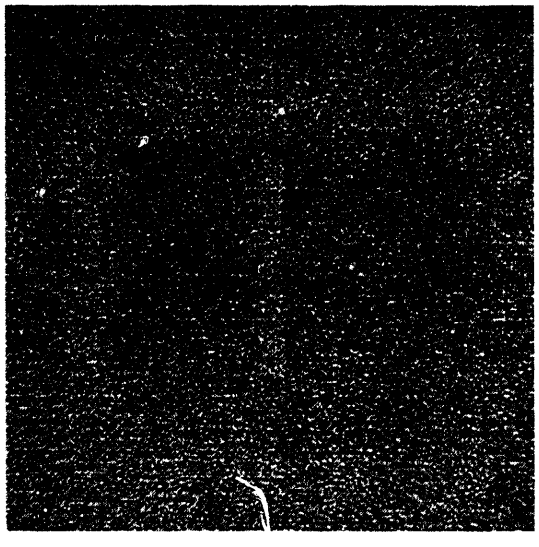

Figure 4.17: Reconstruction for a 500,000 event simulation without using a NR filter.

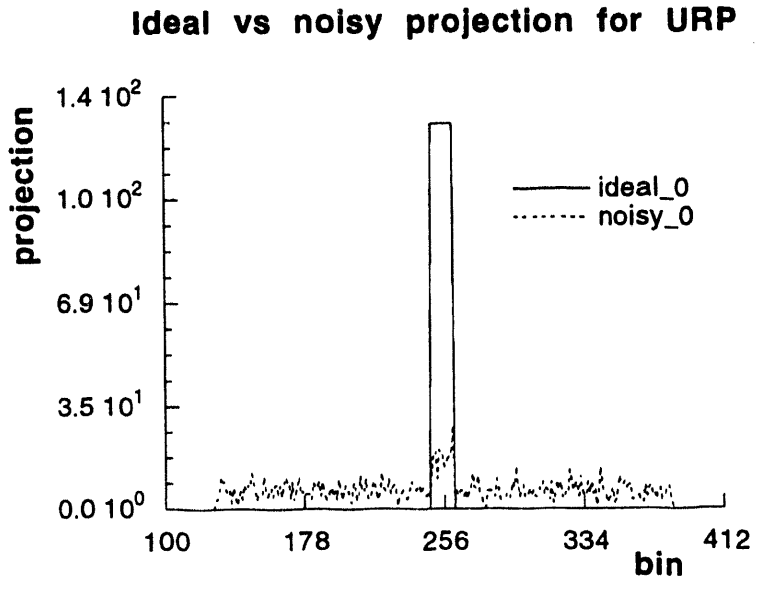

Figure 4.18: Ideal and simulated (500k events) projection for a URP at $0°$.

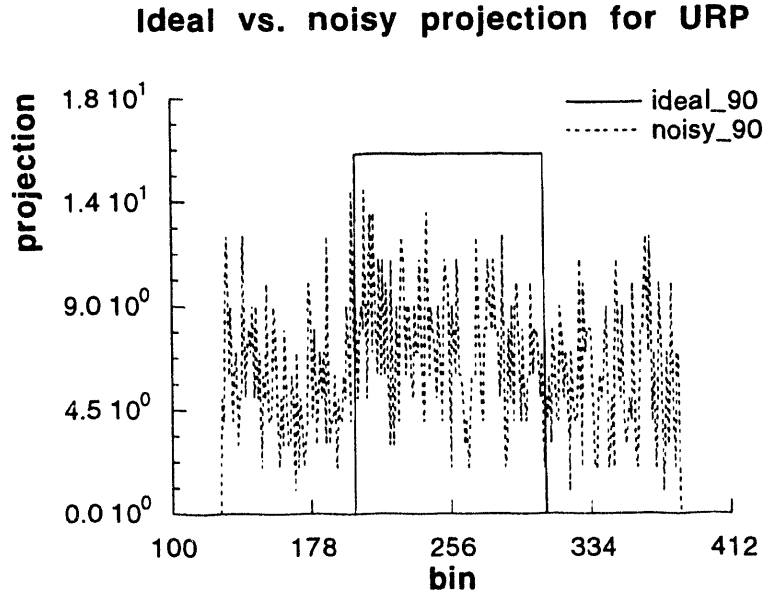

Figure 4.19: Ideal and simulated (500k events) projection for a URP at $90°$.

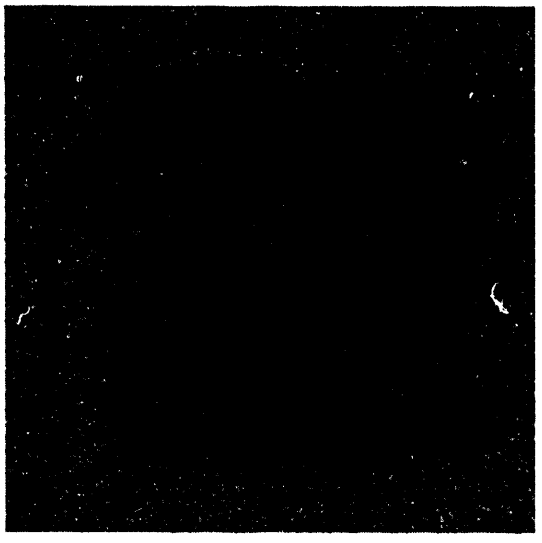

Figure 4.20: BW ($f_c = 0.55f_0$,N=3.5) filtered reconstruction of a 250k event URP

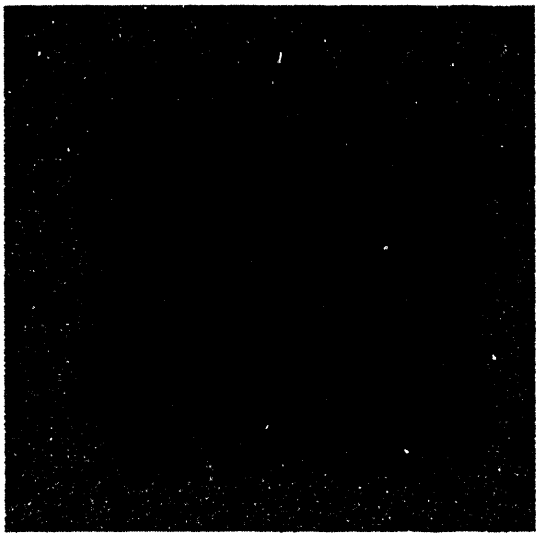

Figure 4.21: Wiener-filtered reconstruction of the 250k event URP

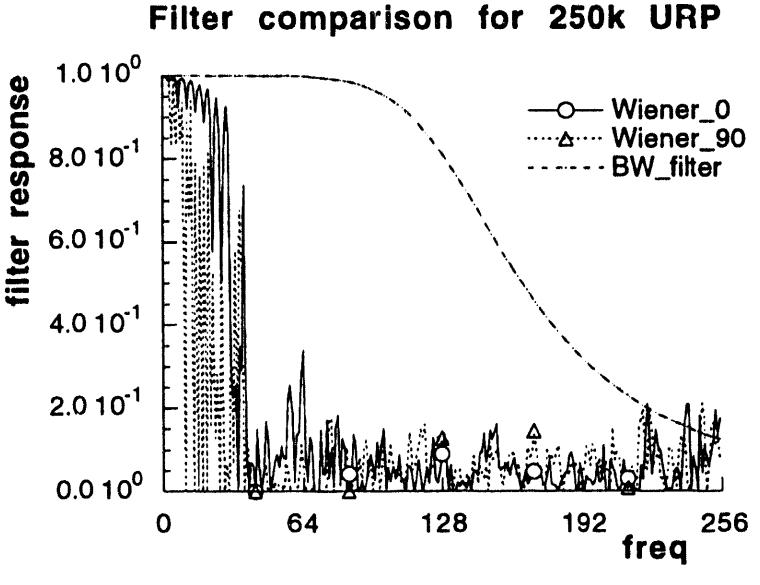

Figure 4.22: Comparison of the BW filter and the Wiener filter (at 0° and 90°) used for the 250k event URP reconstructions.

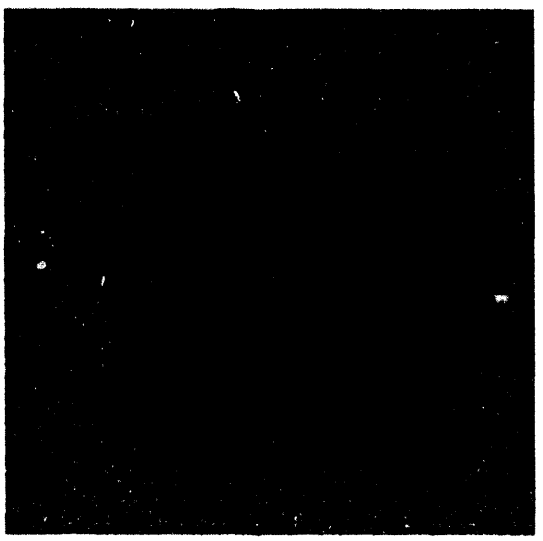

Figure 4.23: BW ($f_c = 0.60 f_0$,N=3.1) filtered reconstruction of a 500k event URP

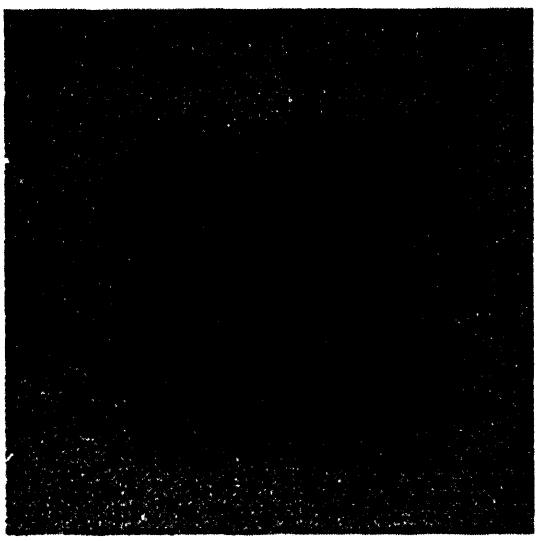

Figure 4.24: Wiener filtered reconstruction of the 500k event URP

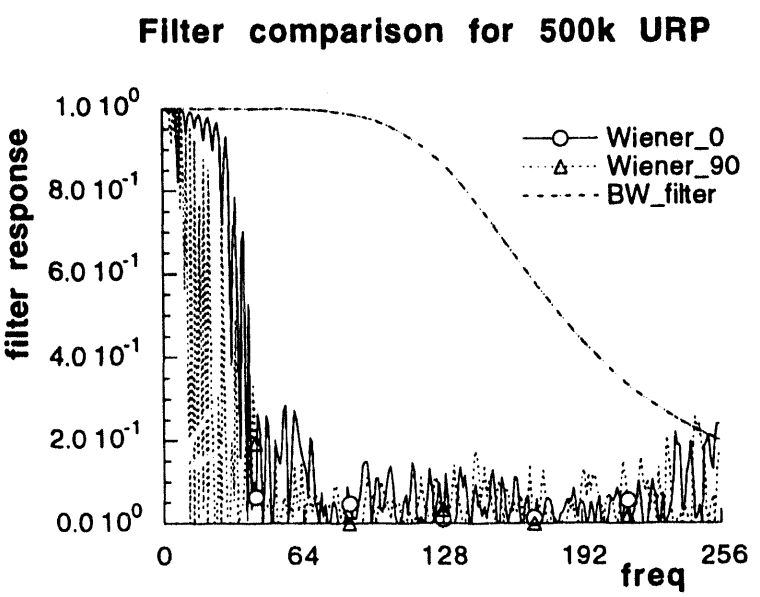

Figure 4.25: Comparison of the BW filter and the Wiener filter (at 0^o and 90^o) for the 500k event URP reconstructions.

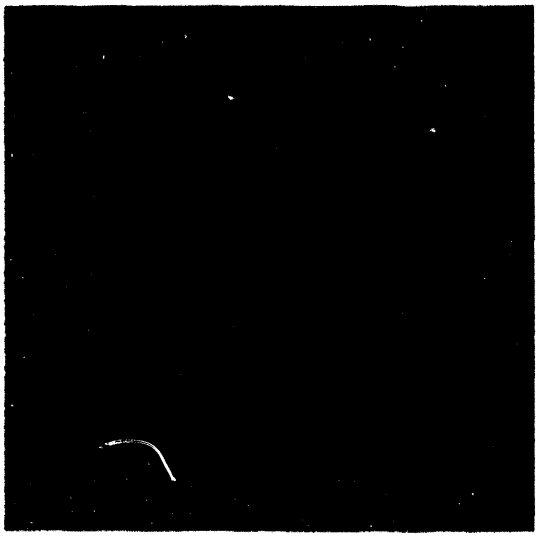

Figure 4.26: BW ($f_c = 0.64 f_0$,N=3.0) filtered reconstruction of a 2M event URP

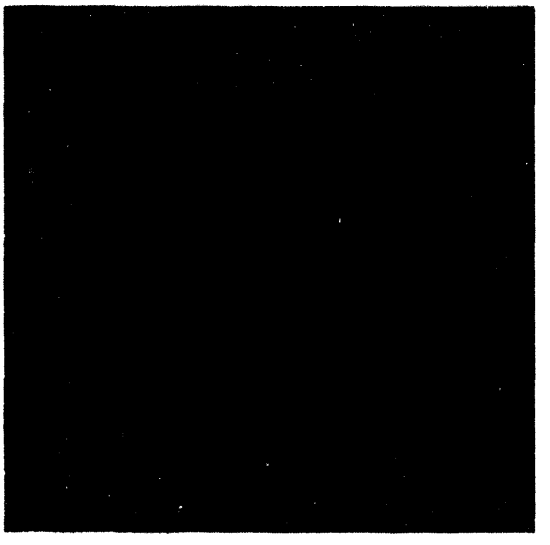

Figure 4.27: Wiener filtered reconstruction of the 2M event URP

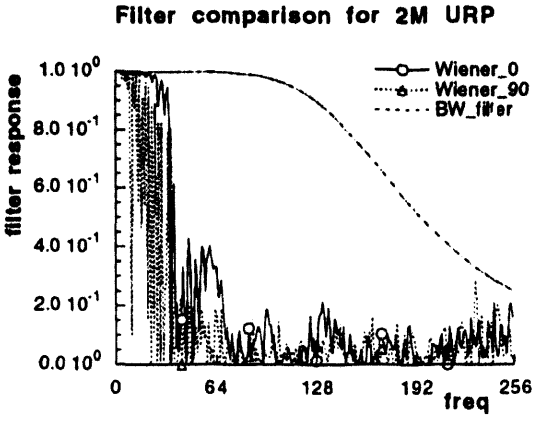

Figure 4.28: Comparison of the BW filter and the Wiener filter (at 0^o and 90^o) for the 2M event URP.

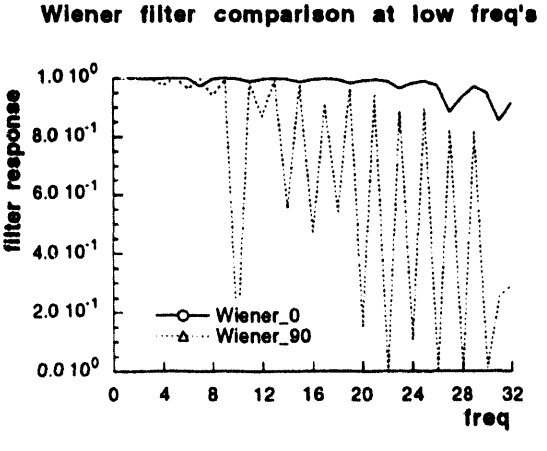

Figure 4.29: Blow up of the low frequencies to illustrate the adaptive nature of the Wiener filter.

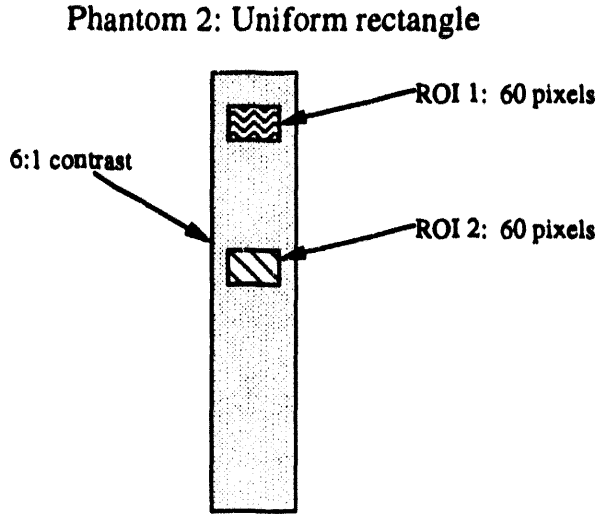

Figure 4.30: The URP is centered on a 256×256 array with a height of 86 pixels and width of 13 pixels. ROI 1 has its lower left corner at (123,165) and its upper right corner is at (132,170). ROI 2 has its lower left corner at (123,125) and its upper right corner is at (132,130).

Uniform rectangular phantom ROI studies						
number of events	filter type	BW param's		ROI 1	ROI 2	μ_1/μ_2
		f_c (% of f_o)	order	σ (% of μ)	σ (% of μ)	(ideal = 1)
250k	ramp			158%	168%	1.10
250k	BW	55%	3.50	64%	67%	0.98
250k	Wiener			70%	68%	1.02
500k	ramp			113%	122%	0.98
500k	BW	60%	3.10	52%	55%	1.00
500k	Wiener			49%	47%	1.01
2M	ramp			53%	62%	0.99
2M	BW	64%	3.00	27%	31%	1.01
2M	Wiener			26%	29%	1.01

Table 4.2: Summary of ROI statistics for the uniform rectangular phantom study. f_c and f_o are the cut-off frequency and the Nyquist rate, respectively. σ and μ are the standard deviation and mean of the ROI.

4.1.3 Phantom of ring surrounding a pair of rectangles

Simulations studies carried out on the ring surrounding a pair of uniform rectangles phantom shown on figure 4.31 is presented below. As shown on the image, the ring and the upper rectangle have equal but lower intensity levels than the lower rectangle. The contrast levels are 4:1 and 8:1, respectively. The ring is centered in the image and has an outer diameter equal to 128 pixels and an inner diameter of 120 pixels. The two rectangles have height equal to 11 pixels and length equal to 65 pixels. The two rectangles are separated by 11 pixels. Using the lower left corner of the image array as the origin (row=0,column=0), the lower left corner of the bottom rectangle is located at (row=96, column=111). The intensities in the 4:1 contrast regions are approximately 12.5, 25, and 100 for the 250k, 500k, and the 2M event simulations respectively. (The intensities in the 8:1 region is double the above.) As in the URP studies, results of the Wiener filter will be presented for the 0° and the 90° cases. The best possible reconstruction is displayed on figure 4.32; an example of a reconstruction without the use of a NR filter is shown on figure 4.1.3 (500k events); the ideal and simulated projections are on figures 4.34 and 4.35. As before, simulations are done with 250k, 500k and 2,000,000 events.

For the 250k simulation, the reconstructed images are shown on figures 4.36 and 4.37. The ring is barely visible in both reconstructions though the rectangles, due to a larger width is much more visible. The lower rectangle, with a 3dB improve SNR, is even more visible than the lower rectangle as expected. Again, the image quality and the visual quality of the noise is similar with the previous phantom studies. The BW filter parameters chosen for this reconstruction are: $f_c = 0.46\ f_0$ and N=3.40. The comparison of the BW filter and the Wiener filter (at 0° and 90°) are presented in figure 4.38.

For the 500k simulation, the Butterworth filter parameters are the following: cut-off frequency = 64% of the Nyquist and filter order is 3.1. Again, the BW filtered images had noise grains which were much larger causing non-uniform textures to appear in regions which are supposed to be uniform.

For the 2M event simulation, the Butterworth filter parameters are the following: cut-off frequency = 66% of the Nyquist and filter order is 3.00. With the expected value of the intensity (before scaling to 0 - 255) being around 100 (and 200 for the high intensity region) the SNR approximately being $\sqrt{100}$ = 20dB (and 23dB) the images look much less noisy and the image quality is similar.

The two ROI's for this phantom is shown in figure 4.46. ROI 1 is in a region where the contrast ratio is 4:1 and ROI 2 is in a region where the contrast is 8:1. The results are presented in the table 4.3. For the 250k event case, the BW filtered reconstructions have standard deviations that are slightly smaller than the Wiener filtered reconstructions. The BW σ for the 4:1 contrast region is 78% of the mean compared to the Wiener σ of 89%. In the 8:1 contrast region, the BW σ is 40% compared to the Wiener σ of 58%. For the 500k event case, the ROI studies resulted in comparable results: ROI 1 has σ's around 65% and ROI 2 has σ's around 35%. For the high statistics case, again, the results were comparable: ROI 1 has σ's around 38% ROI 2 has σ's around 20%.

As with the previous two phantom simulations, the BW filter parameters varied according to the number of detected events. With improving SNR, the cut-off frequency is made higher and filter order made smaller. As explained in the previous two sections, the shape of the BW cannot be made to look similar to outline of the Wiener filter. If the parameters are chosen the mimic the outline of the Wiener in the low frequencies, the BW filter would end up over attenuating the mid to high frequencies causing the result image to have blurred edges as well as having an a image quality similar to that of looking at an image through ground or etched glass.

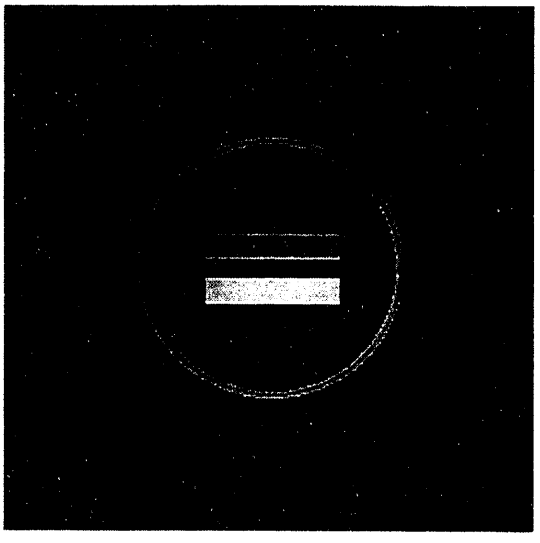

Figure 4.31: The RSR phantom: contrast level of the lower rectangle is 2X of the upper rectangle.

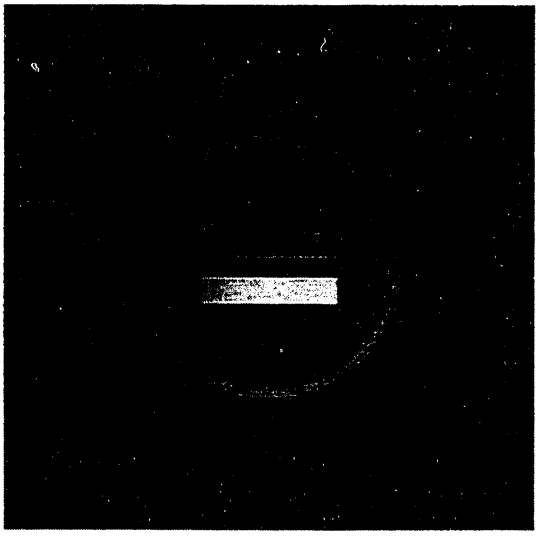

Figure 4.32: The best possible reconstruction for the CBP reconstruction algorithm (i.e.. no noise case).

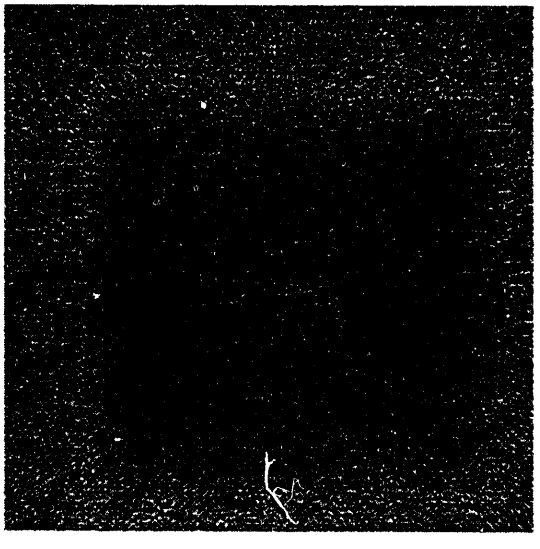

Figure 4.33: Reconstruction for a 500,000 event simulation without using a NR filter.

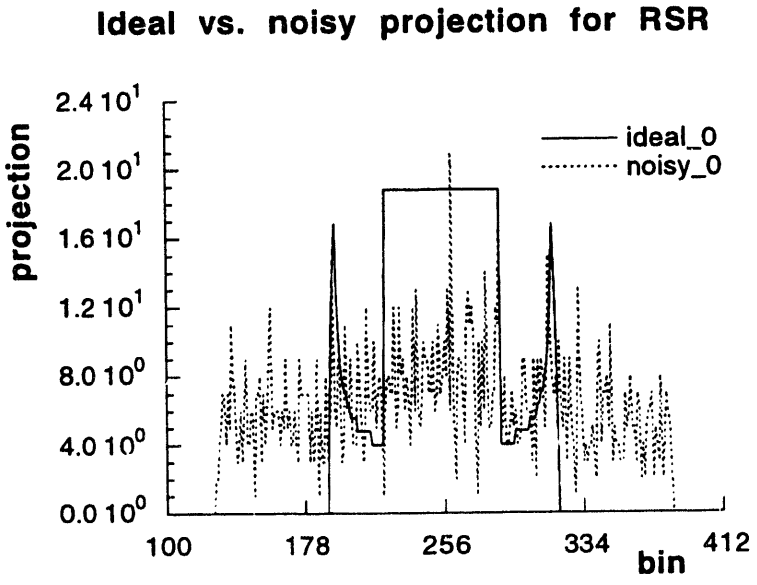

Figure 4.34: Ideal and simulated (500k events) projection for a URP at $0°$.

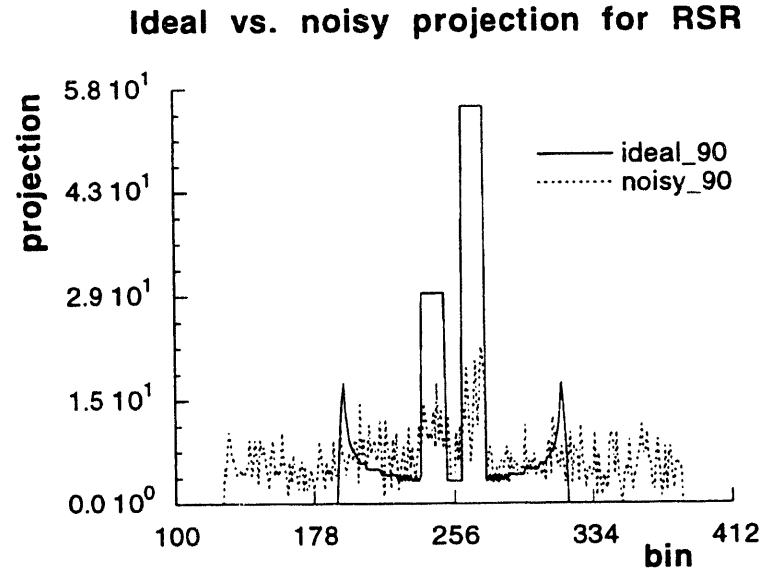

Figure 4.35: Ideal and simulated (500k events) projection for a URP at $90°$.

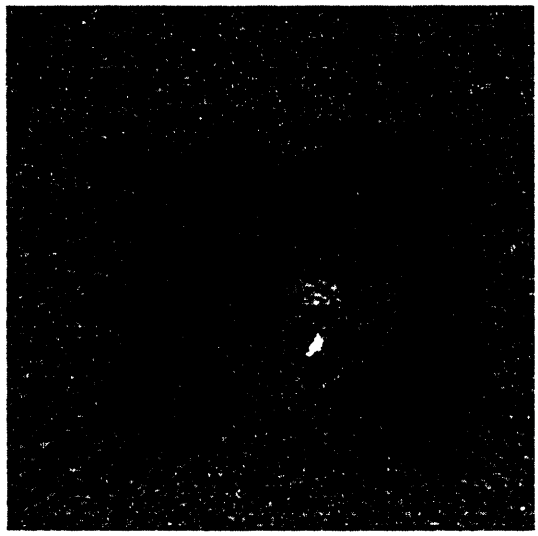

Figure 4.36: BW ($f_c = 0.55 f_0$,N=3.5) filtered reconstruction of a 250k event URP

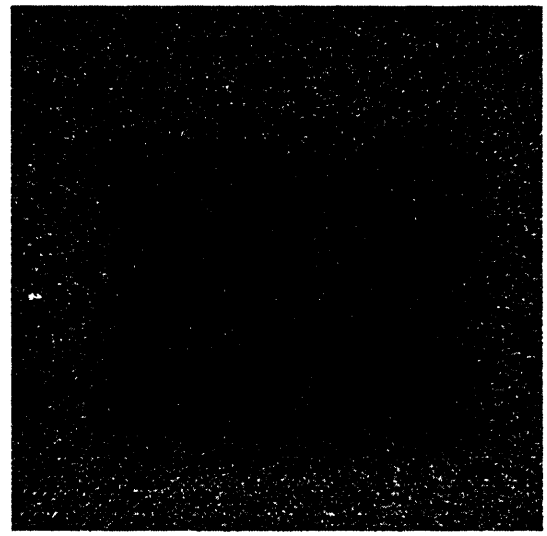

Figure 4.37: Wiener filtered reconstruction of the 250k event URP.

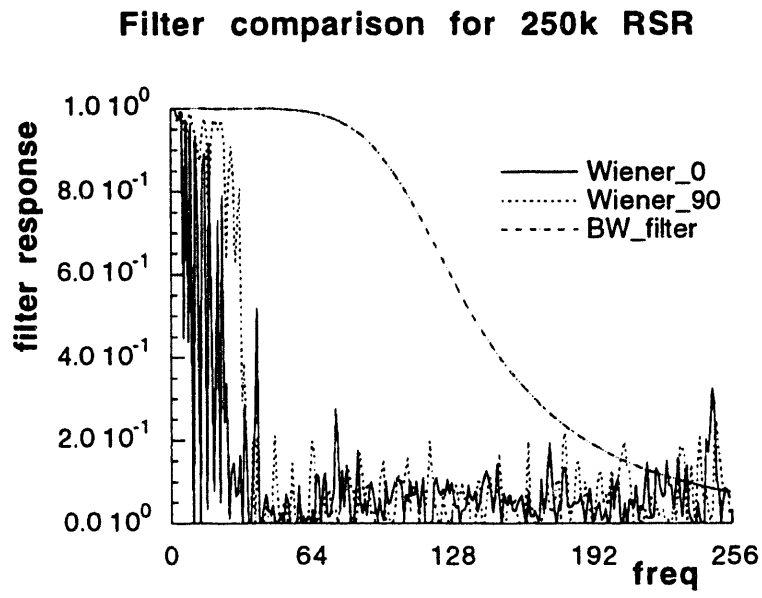

Figure 4.38: Comparison of the BW filter and the Wiener filter (at 0° and 90°) used for the 250k event RSR reconstructions.

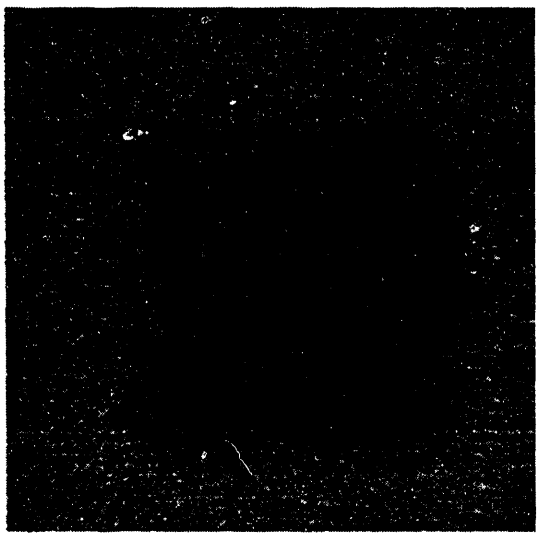

Figure 4.39: BW ($f_c = 0.60 f_0$,N=3.1) filtered reconstruction of a 500k event RSR

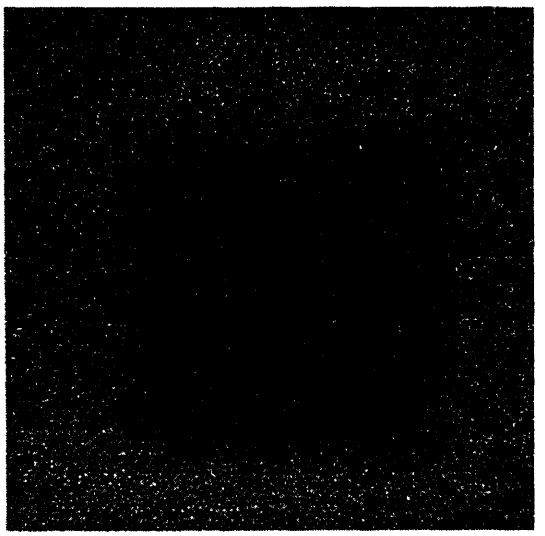

Figure 4.40: Wiener filtered reconstruction of the 500k event RSR

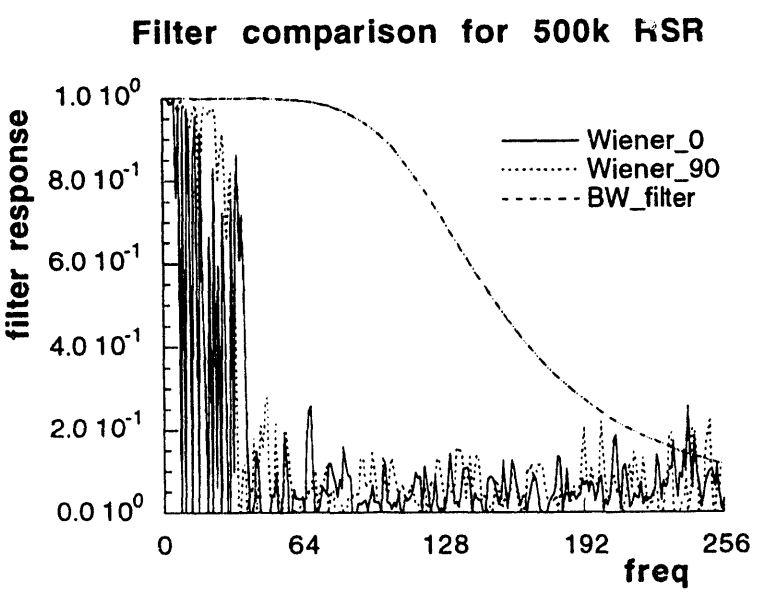

Figure 4.41: Comparison of the BW filter and the Wiener filter (at 0° and 90°) for the 500k event RSR reconstructions.

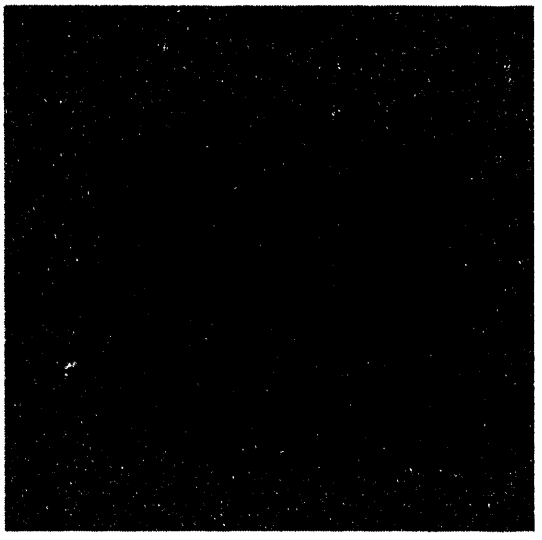

Figure 4.42: BW ($f_c = 0.64 f_0$,N=3.0) filtered reconstruction of a 2M event RSR

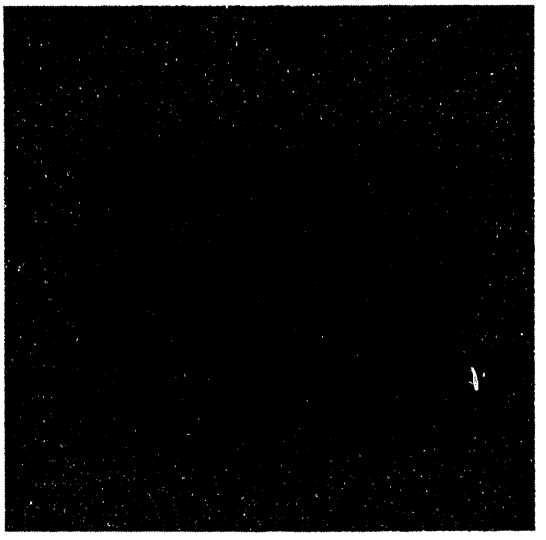

Figure 4.43: Wiener filtered reconstruction of the 2M event RSR

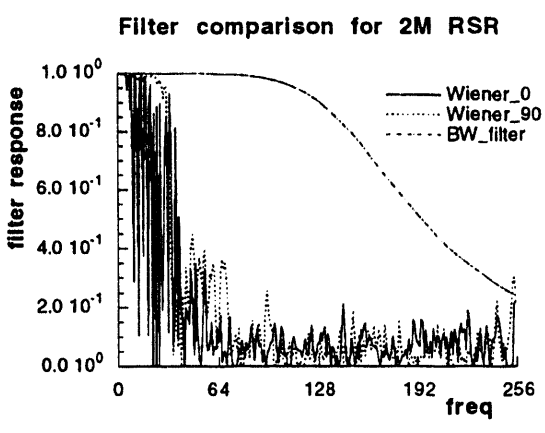

Figure 4.44: Comparison of the BW filter and the Wiener filter (at 0° and 90°) for the 2M event URP.

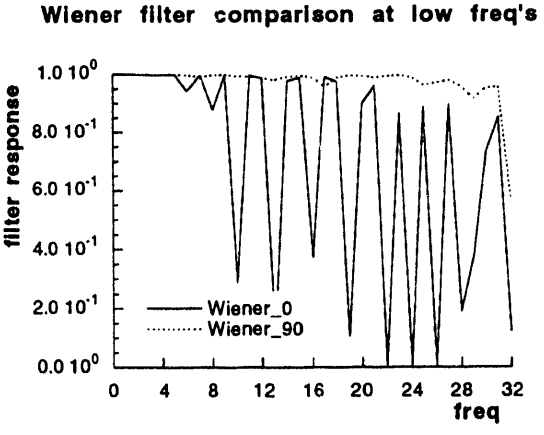

Figure 4.45: Blow up of the low frequencies to illustrate the adaptive nature of the Wiener filter.

Phantom 3: Ring surrounding 2 rectangles

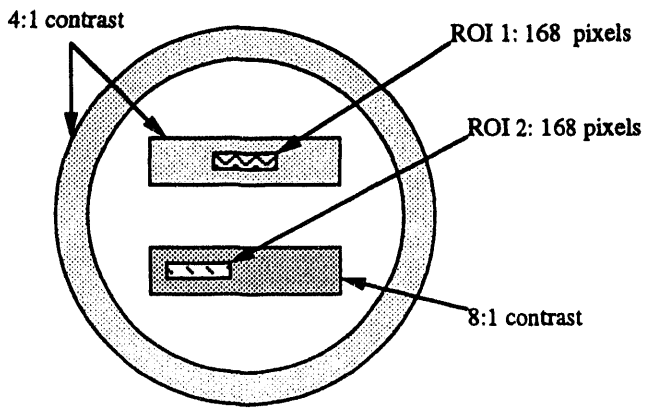

Figure 4.46: The RSR is centered on a 256X256 array with a the outer diameter of the ring of 128 pixels and inner diameter of 120 pixels. The upper rectangle has its lower-left corner at (96,133) and upper-right corner at (160, 145). The lower rectangle has its lower-left corner at (96,111) and upper-right corner at (160,123). ROI 1 is located in the upper rectangle and has its lower left corner at (115,135) and its upper right corner is at (135,142). ROI 2 s located in the lower rectangle and has its lower left corner at (100,113) and its upper right corner is at (120,120).

Ring surrounding rectangles - ROI studies						
number of events	filter type	BW param's		ROI 1	ROI 2	μ_1/μ_2
		f_c (% of f_o)	order	σ (% of μ)	σ (% of μ)	(ideal = 2)
250k	ramp			250%	137%	2.02
250k	BW	46%	3.30	76%	40%	1.99
250k	Wiener			95%	55%	1.99
500k	ramp			180%	94%	2.01
500k	BW	50%	3.10	61%	33%	1.99
500k	Wiener			72%	37%	1.01
2M	ramp			92%	48%	1.99
2M	BW	64%	3.10	42%	21%	1.98
2M	Wiener			39%	20%	1.99

Table 4.3: Summary of ROI statistics for the RSR phantom study. f_c and f_o are the cut-off frequency and the Nyquist rate, respectively. σ and μ are the standard deviation and mean of the ROI.

4.2 Visual quality

This section investigates a new metric for measuring the image quality. The standard deviation of a selected region of uniform intensity is not the optimal measure the image quality of a reconstructed image. Using the URP with 500,000 detected events as an example, this section presents how the visual quality is effected by the fluctuations of the statistical error within a region of known uniform activity.

The profiles of the reconstructed images using the BW filter and the Wiener filter are shown in 4.47 through 4.50. Comparing the profiles through the center of the image, both horizontally and vertically, shows that the deviations from the mean is larger for the BW filtered image as predicted by the statistical summary in table 4.2. How the larger deviations translates to the visual quality is displayed in figures 4.52 and 4.53. In these images, a 8×8 region of uniform activity is magnified and segmented such that the dark pixels represent pixels whose value is within $\pm$ 50% of the local mean and the light pixels are those that exceed the $\pm$ 50% bounds. In this example, the BW-filtered image contain 35 pixels (out of 64) that exceed the threshold whereas the Wiener-filtered image only contain 11 pixels. The clustering of the light-colored pixels in figure 4.53 can lead to a false-positive reading in a BW-filtered image.

Finer quantization of the pixel values in the same ROI's is depicted in figures 4.54 and 4.55. The pixel values are segmented into the following bins: $\pm$12.5% of the ROI mean, between $\pm$12.5% and $\pm$25%, between $\pm$25% and $\pm$50%, between $\pm$50% and $\pm$75% of the mean, and beyond $\pm$75% of the local mean. These finer quantizations further demonstrate that the dispersion of pixel values in an uniform ROI is much larger in the BW-filtered reconstructions than in Wiener-filtered reconstructions. Due to the fact that the BW-filters used in the reconstructions pass more mid-band frequencies, the fluctuations from the mean in the BW-filtered images tend to vary slower as compared to the Wiener-filtered results. This causes the pixels that have larger deviations from the mean to cluster together for the BW-filtered reconstruc-

tions as displayed in figures 4.53 and 4.55. These large clusters of pixels with larger deviations from the mean explain the coarse 2-D texture of the noise present in the BW-reconstructed image.

Although the standard deviations of the Wiener-filtered and the BW-filtered reconstructions are comparable (49% for the Wiener and 52% for the BW), due to the relatively small sample size (64 pixels) the distribution of the noise in the image is not measured well by the standard deviation. The histogram of the pixel values in a 8×8 uniform region measured by sampling 24 independent reconstructions is shown in figure 4.56 and 4.57. These histograms as well as the spatial distribution of the fluctuations (figures 4.54 and 4.55) clearly indicate that the Wiener-filtered reconstructions preserve uniformity better in regions of constant activity. There is, however, a relationship between this new image quality metric and the standard deviation. The smaller the standard deviation, the more likely that the concentration of pixels with small deviation is higher.

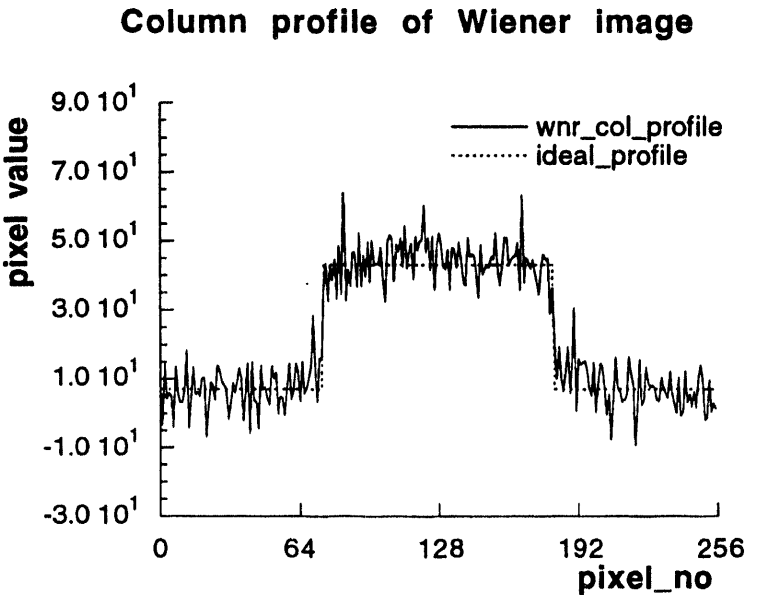

Figure 4.47: Profile of the Wiener-filtered reconstruction of the 500,000 detected event URP — the profile is through the middle of the image (column=128).

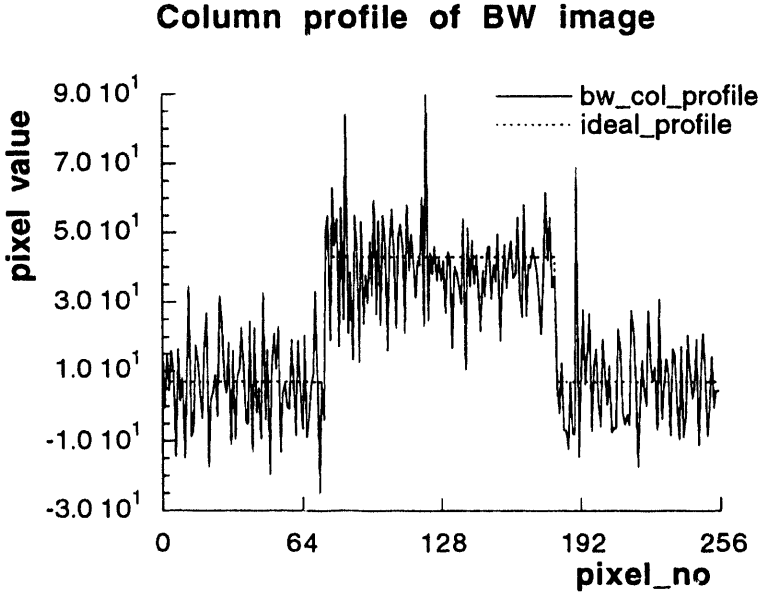

Figure 4.48: Profile of the BW-filtered reconstruction of the 500,000 detected event URP — the profile is through the middle of the image (column=128).

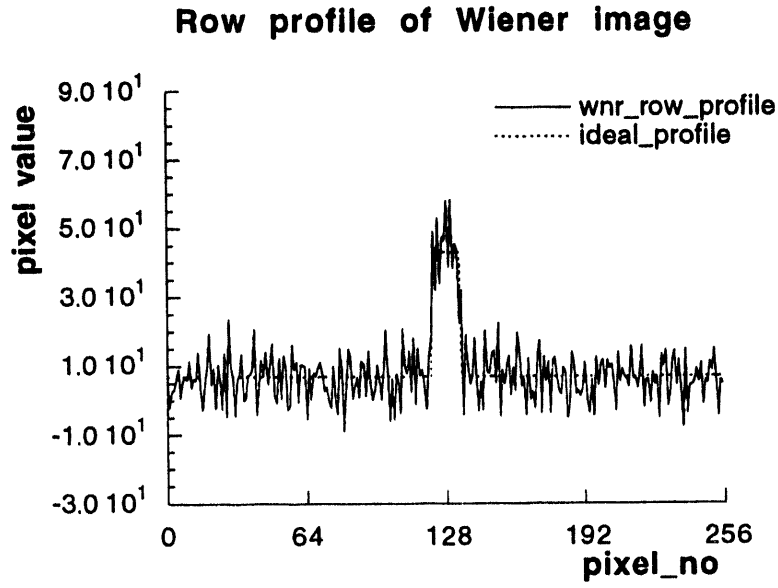

Figure 4.49: Profile of the Wiener-filtered reconstruction of the 500,000 detected event URP — the profile is through the middle of the image (row=128).

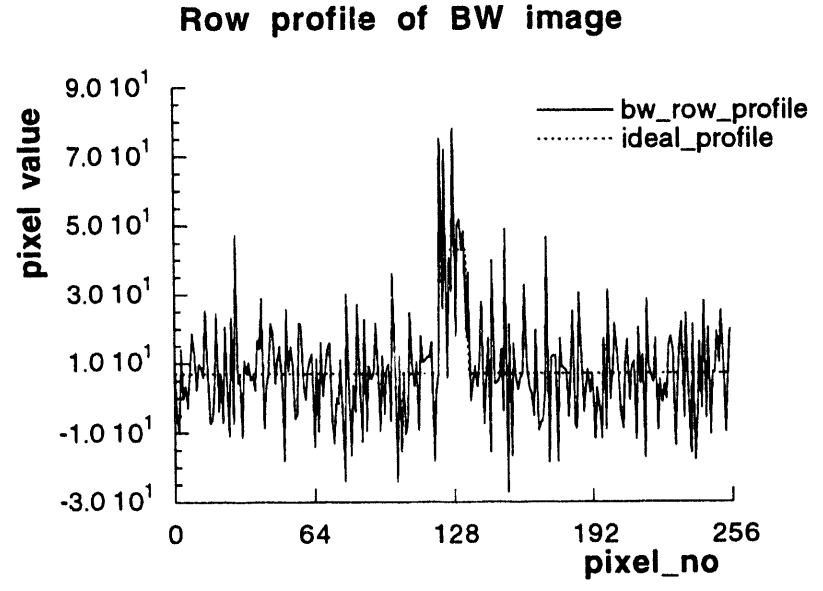

Figure 4.50: Profile of the BW-filtered reconstruction of the 500,000 detected event URP — the profile is through the middle of the image (column=128).

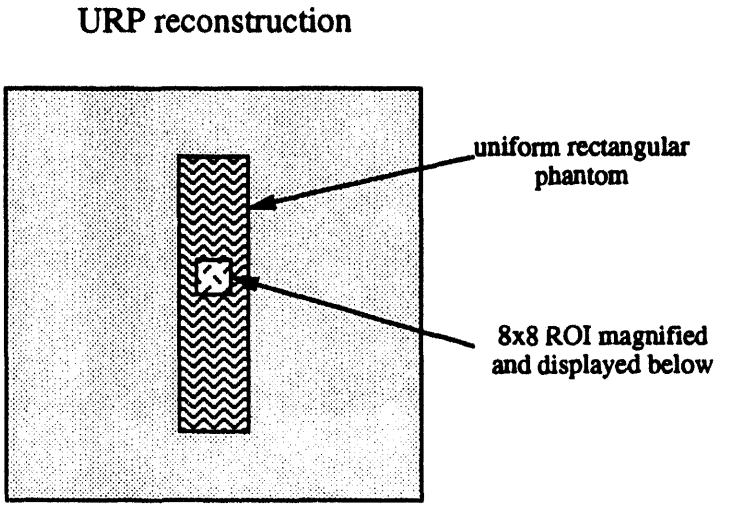

Figure 4.51: Illustration of the ROI in the 500,000 detected event URP reconstruction (for both the Wiener and BW-filtered results)

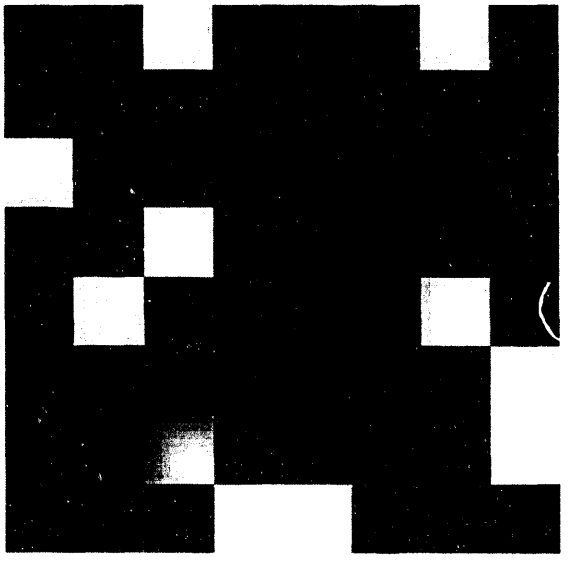

Figure 4.52: An example of a magnified 8x8 ROI shown above for the Wiener-filtered reconstruction. Threshold was set such that the dark pixels are within $\pm 50\%$ of the mean of the ROI while the light-colored pixels fall outside the threshold window.

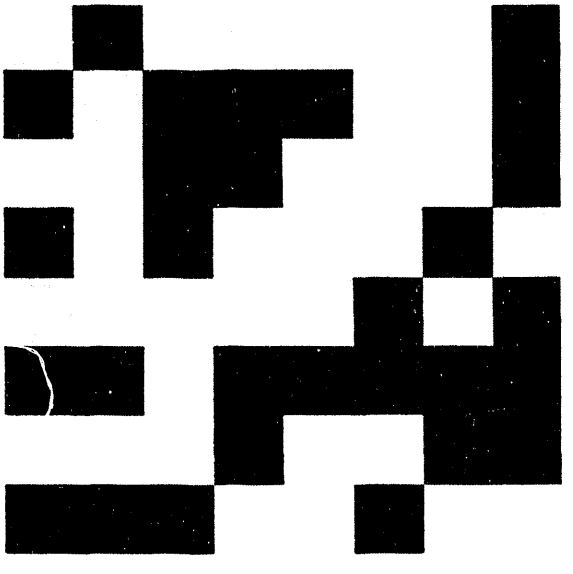

Figure 4.53: An example of a magnified 8x8 ROI shown above for the BW-filtered reconstruction. Threshold was set such that the dark pixels are within $\pm 50\%$ of the mean of the ROI while the light-colored pixels fall outside the threshold window.

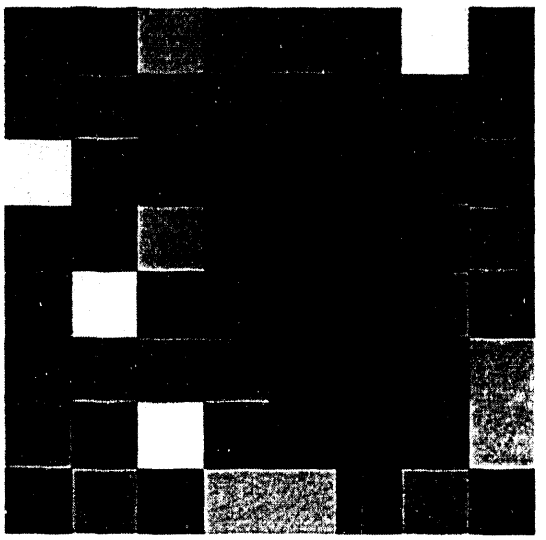

Figure 4.54: 8x8 pixels from the Wiener-filtered reconstruction (same as figure 4.52) quantized 5 levels of gray scale. The darkest pixels are within $\pm 12.5\%$, the next darkest shade is between $\pm 25\%$ and $\pm 12.5\%$, t :5%, the second lightest shade is for pixels that h he mean, and the lightest shade is for pixels beyor

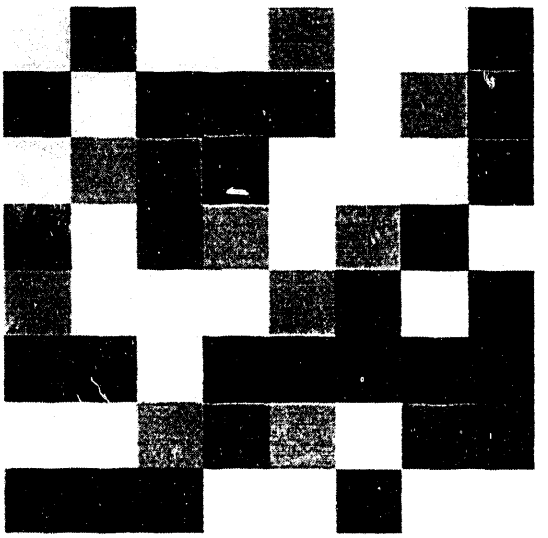

Figure 4.55: 8x8 pixels from the BW-filtered reconstruction (same as figure 4.53) quantized to 5 levels of gray scale. The darkest pixels are within $\pm 12.5\%$, the next darkest shade is between $\pm 25\%$ and $\pm 12.5\%$, the next darkest shade is between $\pm 50\%$ and $\pm 25\%$, the second lightest shade is for pixels that have values that lie between $\pm 50\%$ and $\pm 75\%$ of the mean, and the lightest shade is for pixels beyond $\pm 75\%$ of the local mean.

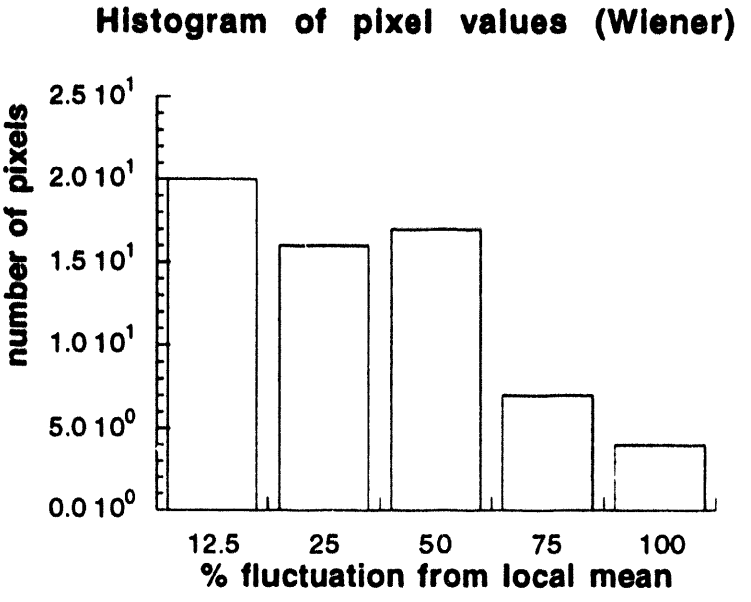

Figure 4.56: Histogram of the pixel values in a 8×8 region of uniform activity measured by sampling 24 independent Wiener-filtered reconstructions of the 500,000 detected events URP.

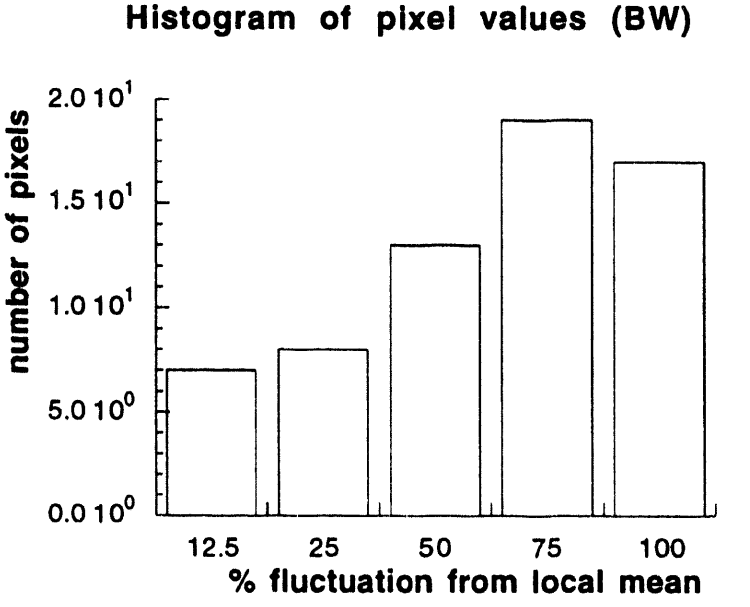

Figure 4.57: Histogram of the pixel values in a 8×8 region of uniform activity measured by sampling 24 independent [illegible]-filtered reconstructions of the 500,000 detected events URP.

4.3 Simulation studies of a brain phantom

Using the Llacer brain phantom (with 1.5M detected events) pictured below in figures 4.58 and 4.59, simulations comparing the results of the CBP reconstruction with the Butterworth NR filter, and the CBP reconstruction with the Wiener NR filter, and a reconstruction using the maximum likelihood estimation (MLE) method will be presented. The MLE reconstruction was carried out using the MLE-CV reconstruction software package described in [20]. Statistical error are measured and compared for the 3 reconstruction techniques in two ROI's — one in a high intensity region and another in a low intensity region. Results are summarized in table 4.4. The same data set used in section 3.3 (study of m vs. Wiener performance) is used for this study.

As the summarized results in table 4.4 indicate the Wiener filter performs favorably compared to both the BW-filtered result and the MLE reconstruction.

Llacer brain phantom ROI studies				
reconstruction method	filter	ROI 1 σ (% of μ)	ROI 2 σ (% of μ)	μ_1/μ_2 ideal=4
CBP	Wiener	1.9%	7.5%	4.1
CBP	BW	2.4%	11.3%	3.9
MLE		2.8%	8.2%	4.2

Table 4.4: Summary of ROI statistics of the Llacer brain phantom. ROI 1 corresponds to the high intensity region and ROI 2 corresponds to the low intensity region. The Wiener filter was generated using 32 highest frequency indices to perform the power normalization. The BW parameters are $f_c = 0.5 f_o$ and N=3.50.

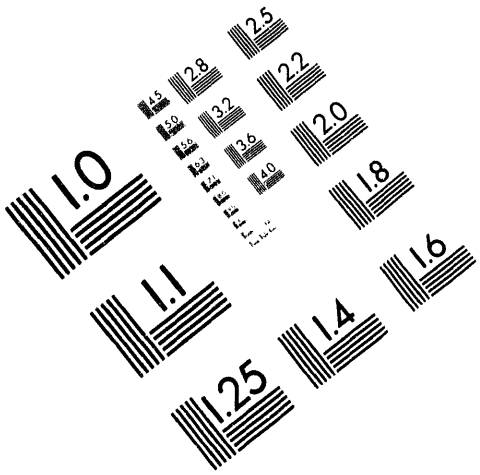

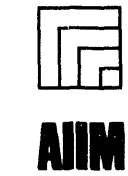

Association for Information and Image Management

1100 Wayne Avenue, Suite 1100
Silver Spring, Maryland 20910

301/587-8202

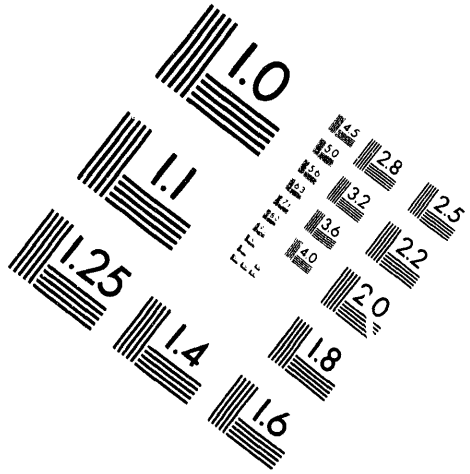

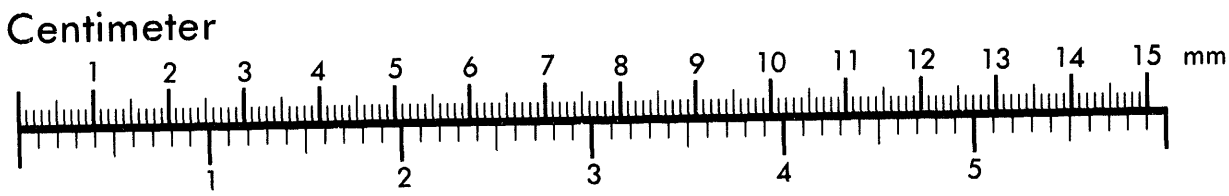

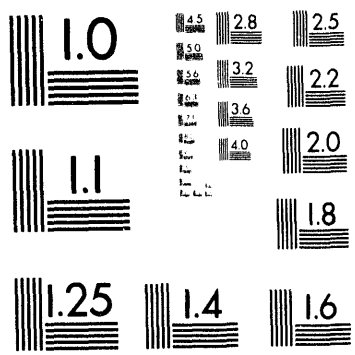

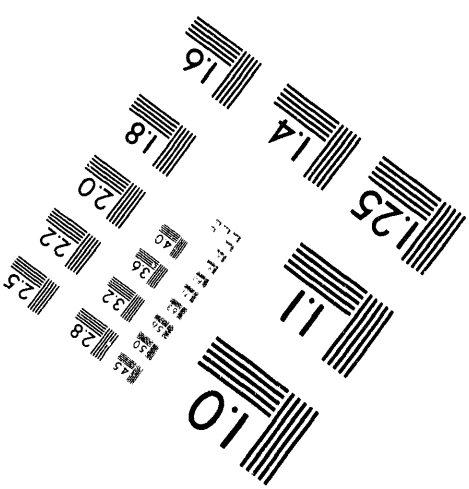

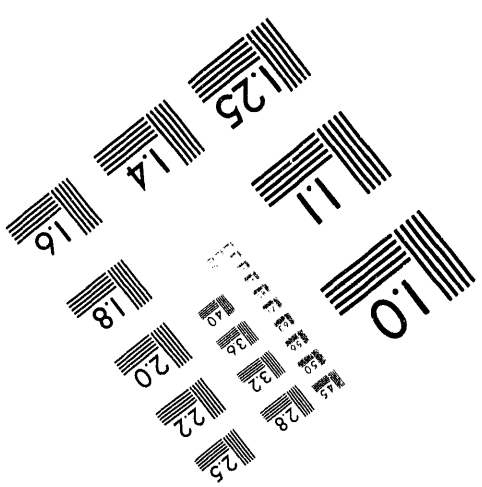

2 of 2

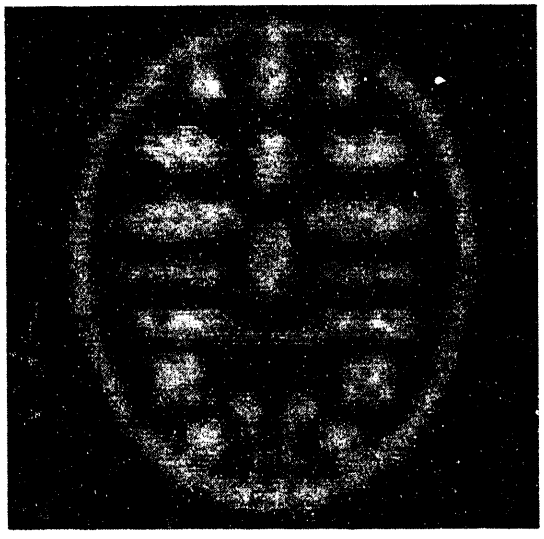

Figure 4.58: Wiener-filtered reconstruction of the Llacer brain phantom

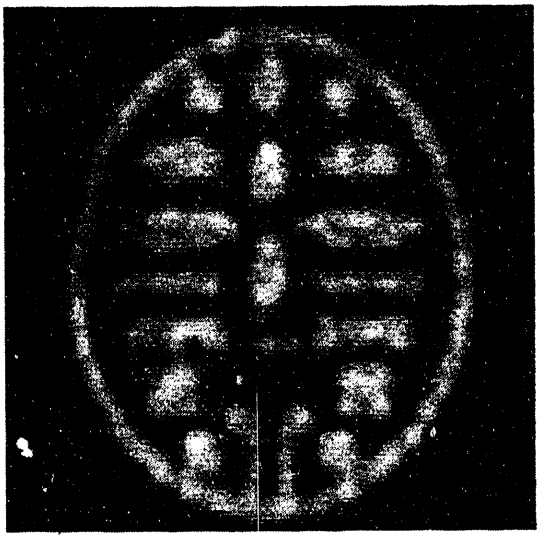

Figure 4.59: BW-filtered reconstruction of the Llacer brain phantom ($f_c = .5f_o$, N=3.5)

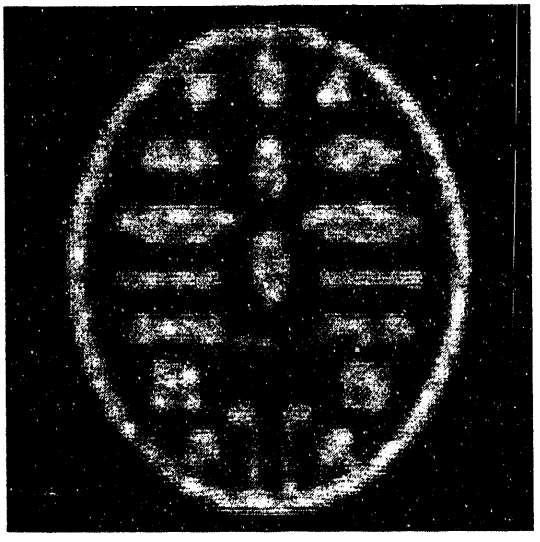

Figure 4.60: MLE reconstruction of the Llacer brain phantom

4.4 Experimental results of the Hoffman brain phantom

The Hoffman phantom is a plexiglass which has been milled to resemble the cross section of a human brain. Sealing the plexiglass after filling it with a positron-emitting tracer and placing it in the tomograph, projection data is measured. Unlike human subjects, the dosage can be made large to increase the SNR so that very good reconstructions are possible as will be shown. Two reconstructions are presented: one with 500,000 detected events and one with 34,000,000 events. Comparisons are made in the resulting Wiener filters and the reconstructed images with the Butterworth filtered images below.

As in the simulations, the comparison between the Wiener filters and the Butterworth filters show that the Butterworth filters pass more mid-frequency information and attenuate the high frequencies more than the Wiener filters. Similarly, the comparison of the reconstructed images shows similar image quality with those of the simulated data. That is, the Wiener-filtered images contain noise which appears more white with fine texture while the BW-filtered images have a much coarser texture. In the 500k case, the noise in the BW filtered reconstructions have mottled noise artifacts. For the 34M event case, the two reconstructions both have good visual appearance but the BW filtered image still contain more mottled noise texture.

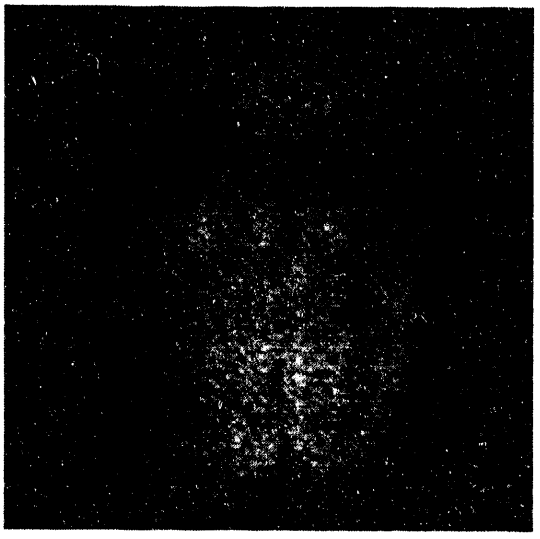

Figure 4.61: Reconstruction of the Hoffman brain phantom with 500,000 counts using the Wiener filter.

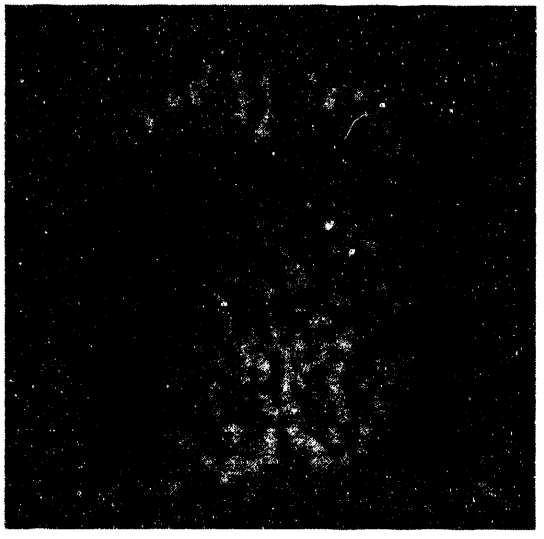

Figure 4.62: Reconstruction of the Hoffman brain phantom with 500,000 counts using the BW filter.

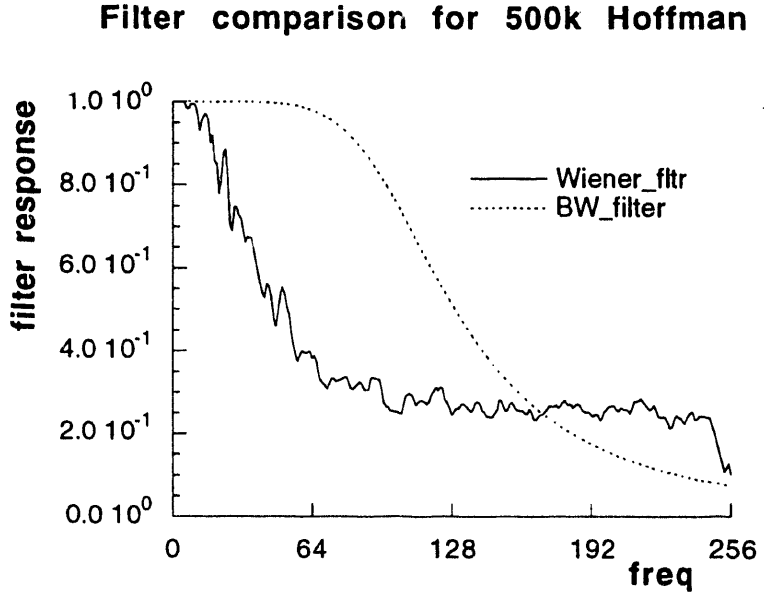

Figure 4.63: Comparison of the BW filter and the Wiener filter (averaged over all 300 angles) for the 500,000 event Hoffman phantom. The BW parameters are: $f_c = 0.42$ and N=3.0. The frequency index of 256 corresponds to the Nyquist limit equal to 6.67 cycles/cm.

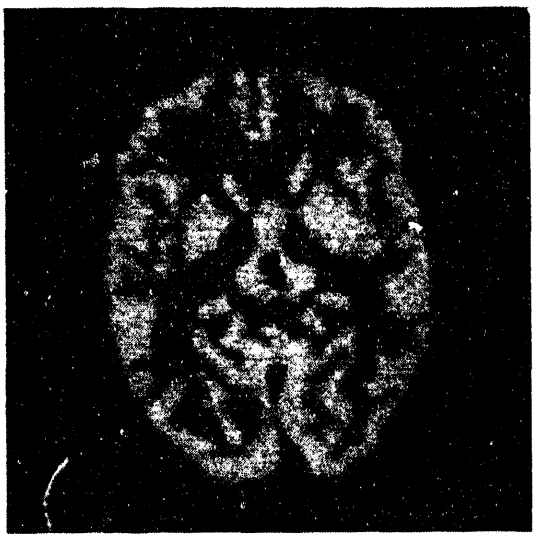

Figure 4.64: Reconstruction of the Hoffman brain phantom with 34,000,000 counts using the Wiener filter.

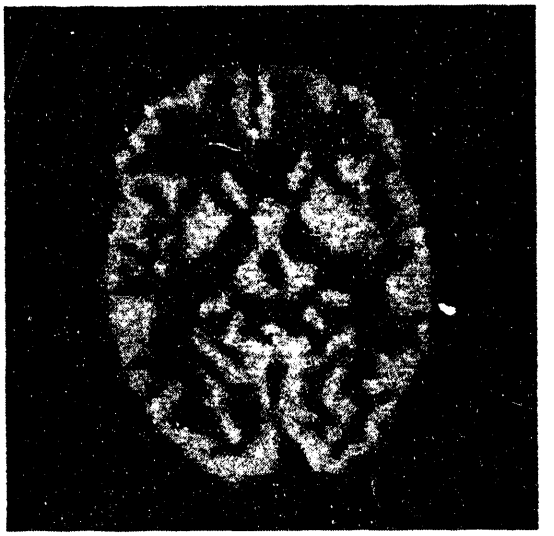

Figure 4.65: Reconstruction of the Hoffman brain phantom with 34,000,000 counts using the BW filter.

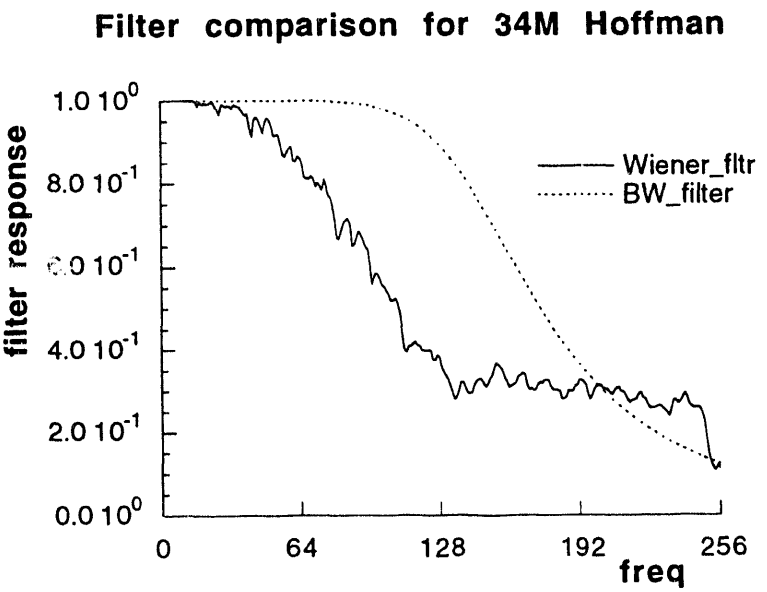

Figure 4.66: Comparison of the BW filter and the Wiener filter (averaged over all 300 angles) for the 34,000,000 event Hoffman phantom. The BW parameters are: $f_c = 0.59 f_0$ and N=4.0. The frequency index of 256 corresponds to the Nyquist limit equal to 6.67 cycles/cm

Chapter 5

Conclusion

5.1 Summary

The goal of this thesis is to derive a computationally efficient algorithm for an optimal linear noise-reduction filter for linear tomographic image reconstruction. Implementing such a filter was done using a frequency-space adaptive-Wiener filter for the convolution backprojection reconstruction method. Theoretical results of the Wiener filter performance was verified through experimental results. Both simulated and experimental data was used to compare the Wiener-filtered reconstructions with the BW-filtered results. Simulation results showed that the adaptive Wiener filter outperformed both the conventional Butterworth NR-filter and the reconstruction using the MLE method in terms of the statistical error measured in standard deviations. However, the standard deviation does not measure image quality and a new image quality metric was developed. By measuring the number of pixels in a region of uniform activity that fall within a chosen threshold, a quantitative measure of the image quality can be described. Using the uniform rectangular phantom with 500,000 detected events as an example, it was shown that the Wiener-filtered reconstructions contained more than twice as many pixels within the $\pm 50\%$ threshold as compared to the BW-filtered result. This new metric is related the standard deviation as the the number of pixels that fall within a percentage of the local mean is inversely related

to the local standard deviation.

The visual quality of the Wiener-filtered reconstructions were shown to be characterized by fine 2-D noise textures with a uniform gray scale whereas the BW-filtered reconstructions were shown to have a coarse texture with oscillating gray-scale values. The coarse texture caused by clustering of pixels with large deviations from the local mean degraded the image quality of BW-filtered reconstructions.

Integral to the adaptive Wiener filtering technique is estimating the signal and noise statistics. Estimation of signal PSD is made difficult in PET data due to the poor SNR of the measured data. This thesis demonstrated a novel technique of estimating the signal and noise PSD's by using the concept of reprojections. By measuring the projections of a reconstructed image, a better estimate of the signal is possible because the SNR is improved in the reprojections. Furthermore, the characteristic noise power can be removed from the reprojections as the noise behavior in the reprojections was calculated using Monte Carlo simulations. Hence, better estimates of the signal and noise PSD was derived and implemented for the adaptive Wiener filter.

5.2 Future work

One direction for further research on the adaptive-Wiener filter for the CBP is to reduce the systematic bias introduced into the filter. The algorithm of the Wiener filter implementation presented in chapter 3 prevents negative filter values to appear by forcing $H_W(f) = 0$ when the noise power estimate exceeds the total power. The algorithm assumes that all of high frequencies are noise which should result in the average value of the filter at those frequencies to be zero. However, as a result of forcing the filter value to go to zero when the calculated value is negative, the average filter value at those highest frequencies become greater than zero. Heuristic schemes to force the average filter values to zero have been suggested such as if neighboring

frequency indices have filter value of zero, then the filter value for that frequency should also be forced to zero. However, such schemes have not been implemented.

Future research in developing an adaptive-Wiener filter for linear reconstruction methods based on the SVD of the projection formation matrix is outlined below. Incorporating priors such as the MTF of the tomograph and the impulse response of the reconstruction algorithm can improve the estimates of the second order statistics required to implement the Wiener filters for the SVD-based reconstructions. The autocorrelation matrix for the noise and signal represented in the basis set of the left and right singular vectors (functions) of $\mathbf{F}$ needs to be estimated. For both the M-P inverse and the Baker reconstruction method a diagonal matrix, $\mathbf{D}$, acts as a filter by properly weighing each component of the basis set. The diagonal elements of $\mathbf{D}$ was shown to be

$$d_k = \frac{\lambda_k^2 E\beta_k^2}{\lambda_k^2 E\beta_k^2 + E\eta_k^2}$$

where β_k's are the elements of $\underline{\beta} = \{\underline{\beta} : b = \mathbf{V}\underline{\beta}\}$ and similarly, η_k's are the elements of $\underline{\eta} = \{\underline{\eta} : \underline{n} = \mathbf{U}\underline{\eta}\}$. The $\mathbf{U}$ and $\mathbf{V}$ are the unitary matrices (operators) which consists of the left and right singular vectors (or functions) of the projection formation matrix, $\mathbf{F}$.

As with the frequency-space adaptive-Wiener filter, an estimate of the second order statistic of the noise can be derived by using Monte Carlos simulations. Utilizing the same normalization scheme of least-squares fitting the characteristic noise power to a specific data set, the characteristic $E\eta_k^2$ shape can be normalized to a specific data set in the highest m indices of k. The scaled signal parameter, $\lambda_k^2 E\beta_k^2$ can then be estimated by subtracting the normalized $E\eta_k^2$ curve from $Ep_k'^2$, the second order statistic of the measured noisy projection. Thus, an adaptive-Wiener filter can be implemented for the two reconstruction methods based on the SVD of $\mathbf{F}$.

Bibliography

[1] J. R. Baker. *Spatially Variant Tomographic Imaging: Estimation, Identification, and Optimization.* PhD thesis, University of California, Berkeley, Nov. 1991.

[2] G. M. Ramachandran and A. V. Lakshiminarayanan. "Three-dimensional reconstruction from radiographs and electron micrographs: Application of convolutions instead of Fourier transforms". *Proceedings of the National Academy of Sciences*, 68(9):2236–2240, 1971.

[3] R. B. Marr. On the reconstruction of a function on a circular domain from a sampling of its line integrals. *Jour. Math Anal Appl*, 45:357–374, 1974.

[4] M. H. Buonocore, W. R. Brody, and A. Macovski. A natural pixel decomposition for two-dimensional image reconstruction. *IEEE Trans. Biomedical Engineering*, BME-29.69–78, 1981.

[5] J. Radon. Über die bestimmung von funktionen durch ihre integralwerte längs gewisser mannigfaltigkeiter. *Berichte Sächsische Akademie der Wissenschaften*, 69:262–267, 1917.

[6] T. F. Budinger, G. T. Gullberg, and R. H. Huesman. *Topics in Applied Physics, chapter 5 - Emission Computed Tomography.* Springer-Verlag, 1979.

[7] Anil K. Jain. *Fundamentals of Digital Image Processing.* Prentice-Hall, Inc., 1989.

[8] L. Chang. A method for attenuation correction in radionuclide computed tomography. *IEEE Transactions on Nuclear Science*, NS-25:638–643, 1978.

[9] L. A. Shepp and B. F. Logan. The Fourier reconstruction of the head. *IEEE Transactions on Nuclear Science*, NS-21(3), 1974.

[10] R. H. Huesman, G. T. Gullberg, and T. F. Budinger. *User's Manual: Donner Algorithms for Reconstruction Tomography.* Technical Report PUB-214 LBL, 1977.

[11] S. E. Derenzo, R. H. Huesman, J. L. Cahoon, A. Geyer, D. C. Uber, T. Vuletich, and T. F. Budinger. Initial results from the Donner 600-crystal tomograph. *IEEE Transactions on Nuclear Science*, NS-34:321–325, 1987.

[12] C. E. Metz and R. N. Beck. Quanititative effects of stationary linear image processing on noise and resolution of structure in radionuclide images. *Jour. of Nuclear Medicine*, 15:164–170, 1974.

[13] E. T. Tsui. *Estimation and Filtering Theory Applied to Computer Tomography in Low Dose Environments.* PhD thesis, University of California, Berkeley, Nov. 1978.

[14] Y. S. Shim and Z. H. Cho. SVD pseudoinversion image reconstruction. *IEEE Transactions on Acoustics, Speech, and Signal Processing*, ASSP-29(4):904–909, August 1981.

[15] K. M. Hanson. *Image Recovery: Theory and Application.* Academic Press, Inc., 1987.

[16] E. Levitan and G. T. Gullberg. A maximum *a posteriori* probability expectation algorithm for image reconstruction in emission tomography. *IEEE Transactions on Medical Imaging*, MI-6:185–192, 1987.

[17] L. A. Shepp and Y. Vardi. Maximum likelihood reconstruction for emission tomography. *IEEE Transactions on Medical Imaging*, MI-1(2), 1982.

[18] Y. Vardi, L. A. Shepp, and L. Kaufman. Statistical model for positron emission tomography. *Jour. American Statistical Assoc.*, pages 8–20, March 1985.

[19] Jorge Llacer and Eugene Veklerov. Statistically based image reconstruction for emission tomography. *Jour. of Imaging Systems and Technology*, 1:132–148, 1989.

[20] Jorge Llacer, Eugene Veklerov, and Kevin Coakley. Statistically analysis of maximum likelihood estimator images of human brain fdg pet studies. *Accepted for publication in IEEE Transactions on Medical Imaging*, 1993.

[21] A. P. Dempster, N. M. Laird, and D. B. Rubin. Maximum likelihood from incomplete data via the em algorithm. *Jour. Royal Statistical Society*, 39:1–38, 1977.

[22] Eugene Veklerov and Jorge Llacer. Stopping rule for the MLE algorithm based on statistical hypothesis testing. *IEEE Transactions on Medical Imaging*, MI-6(4):313–318, 1987.

[23] Jorge Llacer and Eugene Veklerov. Feasible images and practical stopping rules for iterative algorithms in emission tomography. *IEEE Transactions on Medical Imaging*, 8(2):186–193, 1989.

[24] R. Rangayyan, A. P. Dhawan, and R. Gordon. Algorithms for limited-view computed tomography: An annotated bibliliography and a challenge. *Applied Optics*, 24:4000–4012, 1985.

[25] R. H. Huesman. The effects of a finite number of projection angles and finite lateral sampling of projections on the propagation of statistical errors in transverse section reconstruction. *Physics in Medicine and Biology*, 22(3):511–521, 1991.

[26] K. Lange and R. E. Carson. EM reconstruction algorithms for emission and transmission tomography. *Journal of Computer Aided Tomography*, 8:302–316, 1984.

[27] Y. Censor. Finite series expansion reconstruction methods. *Proc. IEEE*, 71(3):409–419, 1983.

[28] S. L. Wood. *A Sytem Theoretic Approach to Image Reconstruction.* PhD thesis, Stanford University, May 1978.

[29] A. P. Sage and J. L. Melsa. *Estimation Theory with Applications to Communication and Control.* McGraw-Hill Book Company, Inc., 1971.

[30] Athanasios Papoulis. *Probability, Random Variables, and Stochastic Processes.* McGraw-Hill, third edition, 1991.

[31] M. Ein-Gal, D. Rosenfeld, and A. Macovski. The consistency of the shadow: An approach to preprocessing in computerized tomography. In R. Gordon, editor, *Image Processing for 2-D and 3-D Reconstruction from Projections: Theory and Practice in Medicine and the Physical Sciences*, pages WB5.1–WB5.4. Optical Society of America, 1975.

[32] E. H. Moore. On the reciprocal of the general algebraic matrix. *Bulletin of the American Mathematical Society*, 26:389 and 394–395, 1920.

[33] R. Penrose. A generalized inverse for matrices. *Proc. Cambridge Philos. Soc.*, 51:406–413, 1955.

[34] Gilbert Strang. *Linear Algebra and Its Applications.* Harcourt Brace Jovanovich, 1988.

[35] Gene H. Golub and Charles F. Van Loan. *Matrix Computations.* Johns Hopkins Unversity Press, second edition, 1989.

[36] A.J. Thomasian. *The Structure of Probability Theory with Applications.* McGraw-Hill Book Company, Inc., 1969.

[37] David G. Luenberger. *Optimization by Vector Space Methods.* John Wiley & Sons, 1969.

[38] Francis B. Hildebrand. *Methods of Applied Mathematics.* Dover Publications, Inc., 1965.

[39] P. Hughett. An optimal constrained linear inverse method for magnetic imaging. in preparation, 1993.

[40] R. H. Huesman, E. M. Salmeron, and J. R. Baker. Compensation for crystal penetration in high resolution positrom tomography. *IEEE Transactions on Nuclear Science*, NS-36:1100–1107, 1989.

[41] S. F. Haber and S. E. Derenzo. Application of mathematical removal of positron range blurring in positron emission tomography. *IEEE Transactions on Nuclear Science*, NS-37:1301–1307, 1991.

[42] Dan E. Dudgeon and Russel M. Mersereau. *Multidimensional Digital Signal Processing.* Prentice-Hall, Inc., 1984.

[43] Jae S. Lim. *Two-Dimensional Signal and Image Processing.* Prentice-Hall, Inc., 1990.

[44] Alan V. Oppenheim, Willsky. Alan S., and Ian T. Young. *Signals and Systems.* Prentice-Hall, Inc., 1983.

[45] William K. Pratt. *Digital Image Processing.* John Wiley & Sons, 1978.

[46] Norbert Wiener. *Extrapolation, Interpolation, and Smoothing of Stationary Time Series, with Engineering Applications.* MIT Press, 1949.

[47] Peter J. Bickel and Kjell A. Doksum. *Mathematical Statistics: Basic Ideas and Selected Topics.* Holden-Day, Inc., 1977.

[48] David R. Brillinger. *Time Series: Data Analysis and Theory.* McGraw-Hill Book Company, Inc., expanded edition, 1981.

[49] Bill Penney, Stephen Glick, and Michael King. Relative importance of error sources in wiener restoration of scintigrams. *IEEE Transactions on Medical Imaging*, MI-9(1):60–70, 1990.

[50] K. M. Hanson. Detectibility in computed tomographic images. *Medical Physics*, 6(5):441–450, 1979.

[51] J. L. Cahoon, R. H. Huesman, S. E. Derenzo, A. Geyer, D. C. Uber, B. T. Turko, and T. F. Budinger. The electronics for the donner 600-crystal positron tomograph. *IEEE Transactions on Nuclear Science*, NS-33, January 1986.

[52] B. T. Turko, G. Zizka, C. C. Lo, B. Leskovar, J. L. Cahoon, R. H. Huesman, S. E. Derenzo, A. Geyer, and T. F. Budinger. Scintillation photon detection and event selection in high resolution positron emission tomography. *IEEE Transactions on Nuclear Science*, NS-34, January 1987.

DATE FILMED

7/18/94

END